Multi-Device Study of Characteristics of Disruptive Magnetohydrodynamic Modes in Tokamaks

Veronika Klevarová

Supervisors: Prof. Dr. Geert Verdoolaege
Prof. Dr. Hartmut Zohm

Advisors: Dr. Gabriella Pautasso
Dr. Peter de Vries
Dr. Joseph Snipes
Dr. Michael Lehnen

Autumn 2020

This research was performed at:

Max Planck Institute for Plasma Physics
Boltzmannstraße 2
D-85748 Garching, Germany

ITER organization
Route de Vinon-sur-Verdon, CS 90 046
13067 St. Paul-lez-Durance, France

In collaboration with:

Ghent University
Faculty of Engineering and Architecture
Department of Applied Physics
Sint-Pietersnieuwstraat 41
9000 Ghent, Belgium

Ludwig-Maximilians-Universität München
Faculty of Physics
Geschwister-Scholl-Platz 1
80539 München, Germany

FUSION-DC - International Doctoral
College in Fusion Science and Engineering
Erasmus Mundus Programme
Coordinated by Ghent University

To my parents.

Abstract

Fusion plasmas confined in tokamaks by magnetic fields often experience disruptions, i.e. sudden losses of the plasma confinement, consisting of a fast thermal quench followed by a plasma current quench, accompanied by the destabilization of the vertical position of the plasma column. Disruptions are a serious threat to the device components in terms of large heat and particle loads on the plasma-facing components and the forces applied on the various components of the device. Disruption avoidance, prediction and, in case of an unavoidable disruption, mitigation, is a prerequisite for safe, efficient operation of large tokamaks (e.g. ITER, currently under construction). Disruption onset is known to be linked with the development of magnetohydrodynamic (MHD) modes. In particular, the crossing of a critical value of the mode amplitude has been identified as a main disruption trigger in the past (de Vries, 2011). This thesis addresses multiple aspects of MHD mode development prior to a disruption. The main diagnostic instruments serving for the mode amplitude monitoring were magnetic sensors, particularly saddle and Mirnov coils. The main tool in the work is an extensive (> 1100 entries) database of discharges terminated by a disruption. The database consists of measurements from devices of various plasma size (COMPASS, ASDEX Upgrade, DIII-D, JET), but similar aspect ratios. Identical data selection criteria were applied across all devices for compiling the database. All database entries were manually classified according to the main cause leading to onset of the MHD mode. Earlier works reported that in large devices, most of the modes were static in the laboratory frame ('locked') (de Vries, 2016). However, in general modes are often observed to rotate prior to becoming locked, as also seen in the database compiled in this work. This thesis addresses important characteristics of both rotating and locked modes in the context of the disruption initiation. The mode amplitude development is followed throughout the mode braking, the stationary phase of the mode and the disruption onset. The observations reported in this work may contribute to a set of design criteria for future disruption forecasting schemes. The work explores both existing physical models for describing mode dynamics, as well as a phenomenological description of mode behavior on the basis of the multi-machine database.

A first part of the work aims to validate a model for mode locking on the basis of a reduced database of ASDEX Upgrade discharges. Not discriminating between plasma configurations, the model allows to estimate the duration of the deceleration phase, as well as the critical mode width for locking. Both quantities are important for the design of algorithms that aim to avoid disruptions by means of external actuators. The reduced ASDEX Upgrade database consists of discharges covering a broad range of plasma parameters and discharge scenarios. It was found that the model successfully describes locking of large modes in those cases where the mode deceleration started in a quasi-stationary phase of the discharge (i.e. with low variability of the global plasma angular momentum prior to mode seeding) and where deceleration took place over temporal intervals that are long in comparison with the momentum confinement time. Theoretical braking curves and locking durations predicted with the model were in good quantitative agreement with the experimental data. On the other hand, the model failed to

reproduce the braking curves of modes appearing towards the end of a transient phase, e.g. during an impurity influx or when approaching the disruptive density limit. A modified mode equation of motion is proposed, which accounts for transient variation of the plasma density, e.g. during the development of a MARFE and its poloidal destabilization from its stable location at the plasma X-point. The experimental and theoretical mode braking curves were in closer accordance when the modified model was applied.

The second part of the work focuses on the analysis of the duration of (quasi-) stationary modes, as well as the pre-disruptive growth of the measured mode amplitude. In addition, regression analysis is conducted of the locked phase duration and a previously derived scaling for the disruptive mode amplitude is validated (de Vries, 2016). The study was performed using the full database of disruptive discharges covering a broad range of plasma parameters, including a considerable range of plasma dimensions. The measured mode durations span several orders of magnitude in all devices, but nevertheless the median duration is seen to increase with plasma size. Several factors are discussed that could influence the locked mode duration, such as the plasma control system response to exceptional situations (e.g. switching on or off external heating modules, initiation of a fast plasma current ramp-down, plasma shape modification etc.), the specific location of the discharge within the typical device parametric space (often reflected in the disruption root cause) and the occurrence of minor disruptive events (accompanied by a partial loss of the plasma confinement). The scaling formula for the disruptive mode amplitude is reported to systematically overestimate the experimental amplitudes in case of modes detected with magnetic sensors located at the torus high-field-side. A proposal for modifying the scaling, adjusting for this case, is presented. The modified scaling equation allowed more accurate predictions of the critical mode amplitude threshold. Linear extrapolation with plasma size of both experimental and predicted times-to-disruptions and the associated fraction of disruptions suggests that, in devices with large plasma minor radius, the locked modes will grow on time scales that are long enough to allow for disruption mitigation by means of fast massive gas injection or pellet injection. A regression analysis aimed at establishing a scaling relation for the locked mode phase duration with plasma parameters. A physically plausible scaling relation could be established, which however explains only part of the variability of the data. Possible origins of the remaining scatter are discussed, such as the onset of minor disruptions in the presence of the mode, mode re-rotation under a constant external torque input etc. Application of the scaling to the ITER Baseline scenario suggests that the locked phase duration will be of the order of hundreds of milliseconds or seconds in ITER, depending on the particular disruption root cause. Such time scales are in favour of a timely disruption mitigation in ITER.

Parts of Sec. 2.5.2, Sec. 2.5.3 and Chap. 5 were adapted from V. Klevarová, H. Zohm, G. Pautasso, G. Tardini, R. McDermott, G. Verdoolaege, J.A. Snipes, P.C. de Vries, M. Lehnen, the EUROfusion MST1 team and the ASDEX Upgrade team, Validation of a Tearing Mode Locking Model Using a Database of Disruptive Plasmas at ASDEX Upgrade, 2019, Plasma Physics and Controlled Fusion, ***62****(2), 025024.*

Parts of Chap. 4 and Chap. 6 were adapted from V. Klevarová, G. Pautasso, P.C. de Vries, R. Sweeney, T. Markovič, H. Zohm, G. Verdoolaege, M. Komm, J. Havlicek,

J.A. Snipes, M. Lehnen, JET contributors, the EUROfusion MST1 team, the ASDEX Upgrade team and the DIII-D team, Multi-device study of temporal characteristics of magnetohydrodynamic modes initiating disruption, 2020, Fusion Engineering and Design, ***160C****, 111945.*

Samenvatting

Fusieplasma's opgesloten door magnetische velden in tokamaks ervaren vaak disrupties, plotse verliezen van de plasmaopsluiting, bestaande uit een snelle thermische onderdrukking gevolgd door het uitdoven van de plasmastroom, gepaard met een destabilisering van de verticale positie van de plasmakolom. Disrupties vormen een ernstige bedreiging voor de componenten van de machine ten gevolge van de grote warmte- en deeltjesbelasting van wandcomponenten nabij het plasma en de krachten uitgeoefend op de verschillende componenten van de machine. Het vermijden, voorspellen en beperken ervan is een voorwaarde voor een veilige en efficiënte werking van grote tokamaks (bv. ITER, momenteel onder constructie). Het is bekend dat de initiatie van een disruptie gelinkt is aan de ontwikkeling van magnetohydrodynamische (MHD) instabiliteiten. Meer bepaald werd het overschrijden van een drempelwaarde van de mode-amplitude eerder al geïdentificeerd als een belangrijke aanleiding voor disrupties (de Vries, 2011). Dit proefschrift gaat in op meerdere aspecten van de ontwikkeling van MHD-modes voorafgaand aan een disruptie. De belangrijkste diagnostische technieken die gebruikt werden voor het monitoren van de amplitude van de modes waren magnetische sensoren, in het bijzonder zadelspoelen en Mirnovspoelen. Als belangrijkste instrument werd in ons werk een grote databank gebruikt van meer dan 1100 ontladingen die eindigden in een disruptie. De databank bevat metingen van machines van verschillende plasmagrootte (COMPASS, ASDEX Upgrade, DIII-D, JET), maar gelijkaardige aspectverhouding. Identieke selectiecriteria werden toegepast voor elke machine om de databank samen te stellen. Alle metingen in de databank werden handmatig geclassificeerd op basis van de hoofdoorzaak die leidt tot de aanvang van de MHD-mode. Uit eerder werk blijkt dat in grote machines de meeste modes statisch zijn in het laboratoriumsysteem ('vergrendeld') (de Vries, 2016). In het algemeen wordt echter vaak gezien dat de modes roteren alvorens te vergrendelen, zoals ook in de databank samengesteld in dit werk. Deze thesis behandelt belangrijke kenmerken van zowel de roterende als de vergrendelde modes in de context van de aanvang van disrupties. De ontwikkeling van de amplitude van de mode wordt gevolgd tijdens het afremmen, de stationaire fase van de mode en de aanvang van de disruptie. De observaties die in dit werk gemaakt worden, kunnen mogelijk bijdragen tot een set designcriteria voor toekomstige strategieën voor disruptiepredictie. Ons werk maakt zowel gebruik van bestaande analytische modellen om de dynamica van de modes te beschrijven, als van een fenomenologische beschrijving van het gedrag van de modes op basis van de multi-machine-databank.

Een eerste deel van het proefschrift heeft als doel een model te valideren voor de vergrendeling van modes op basis van een gereduceerde databank van ontladingen van ASDEX Upgrade. Zonder onderscheid te maken tussen plasmaconfiguraties, laat het model toe de duur van de fase van afremming te schatten, evenals de kritische breedte van de mode voor het vergrendelen. Beide grootheden zijn belangrijk voor het ontwerp van algoritmes die gericht zijn op het vermijden van de disruptie door middel van externe actuatoren. De gereduceerde databank van ASDEX Upgrade bestaat uit ontladingen die een groot bereik van plasmaparameters

en operationele scenarios bestrijken. Het model blijkt met succes het vergrendelen van grote modes te beschrijven in die gevallen waarin het afremmen van de mode begon in een quasi-stationaire fase van de ontlading (d.w.z. met een lage variabiliteit van het globale impulsmoment van het plasma vóór het ontstaan van de mode) en waarin de vertraging plaatsvond over een lange periode, in vergelijking met de tijdschaal van impulsopsluiting. Theoretische remcurves en duur van vergrendeling, voorspeld aan de hand van het model, waren in goede kwantitatieve overeenstemming met de experimentele data. Anderzijds slaagde het model er niet in om de remcurves van modes te reproduceren die ontstaan naar het einde van een transiënte fase toe, bijvoorbeeld tijdens een influx van onzuiverheden of bij het naderen van de disruptieve dichtheidslimiet. Een gewijzigde bewegingsvergelijking voor de modes werd voorgesteld, die rekening houdt met tijdelijke variaties van de plasmadichtheid, bijvoorbeeld tijdens de ontwikkeling van een MARFE en de poloïdale destabilisering ervan ten opzichte van de stabiele positie ter hoogte van het X-punt van het plasma. De experimentele en theoretische remcurves waren in betere overeenstemming gebruik makend van het gewijzigde model.

Het tweede deel van de thesis focust op de analyse van de duur van (quasi) stationaire modes, alsook de toename van de gemeten amplitude van modes voorafgaand aan een disruptie. Daarnaast wordt regressieanalyse uitgevoerd van de duur van vergrendeling en wordt een eerder afgeleide schaling van de amplitude van de disruptieve mode gevalideerd (de Vries, 2016). Dit onderzoek werd uitgevoerd met behulp van de volledige databank van disruptieve ontladingen, met een grote variatie in de plasmaparameters, waaronder een aanzienlijk bereik in plasmadimensies. De gemeten duur van de modes varieert over meerdere grootteordes, maar de mediaan ervan neemt niettemin toe met de grootte van het plasma. Verschillende factoren worden besproken die de duur van vergrendeling van de modes kunnen beïnvloeden, zoals de reactie van het plasmacontrolesysteem op uitzonderlijke situaties (bv. aan- en afschakelen van externe verhittingsmodules, start van een snelle stroomafschakeling, wijziging van de vorm van het plasma, enz.), de specifieke locatie van de ontlading binnen de typische parametrische ruimte van de machine (vaak weerspiegeld in de hoofdoorzaak van de disruptie) en het voorkomen van kleine disruptieve gebeurtenissen (die gepaard gaan met een gedeeltelijk verlies van de plasmaopsluiting). De schalingswet voor de amplitude van de disruptieve mode overschat systematisch de experimentele amplitudes in het geval van modes die worden gedetecteerd met magnetische sensoren die zich aan de hoge-veld-kant van de torus bevinden. Er wordt daarom een voorstel gedaan om de schalingswet aan te passen voor dit geval. De gewijzigde relatie liet een meer nauwkeurige voorspelling toe van de drempelwaarde voor de kritische modeamplitude. Lineaire extrapolatie met de plasmagrootte van zowel de experimentele als de voorspelde tijd-tot-disruptie en de bijbehorende fractie van disrupties, suggereert dat, in machines met een grote plasmastraal, de vergrendelde modes zullen groeien op een tijdschaal die gunstig is voor de beperking van disrupties door snelle massale gas- of pelletinjectie. Een regressieanalyse, gericht op het afleiden van een schalingswet voor de duur van de vergrendelde fase met de plasmaparameters, levert een schalingsformule op die echter significante onzekerheden op de voorspellingen geeft. Mogelijke redenen voor die spreiding worden besproken, zoals de start van kleine disrupties in het bijzijn van de mode, het opnieuw roteren van de mode bij constant toegevoegd extern impulsmoment, enz. Toepassing van de schalingswet op het ITER-basisscenario suggereert dat de duur

van de vergrendelde fase van de orde van honderden milliseconden of seconden zal zijn in ITER, afhankelijk van de hoofdoorzaak van de disruptie. Dergelijke tijdschalen zijn gunstig voor een tijdige beperking van disrupties in ITER.

Delen van Sec. 2.5.2, Sec. 2.5.3 en Hoofdstuk 5 werden opgenomen uit V. Klevarová, H. Zohm, G. Pautasso, G. Tardini, R. McDermott, G. Verdoolaege, J.A. Snipes, P.C. de Vries, M. Lehnen, het EUROfusion MST1 team en het ASDEX Upgrade team, Validation of a Tearing Mode Locking Model Using a Database of Disruptive Plasmas at ASDEX Upgrade, 2019, Plasma Physics and Controlled Fusion, ***62****(2), 025024.*

Delen van Hoofdstuk 4 en Hoofdstuk 6 werden opgenomen uit V. Klevarová, G. Pautasso, P.C. de Vries, R. Sweeney, T. Markovič, H. Zohm, G. Verdoolaege, M. Komm, J. Havlicek, J.A. Snipes, M. Lehnen, JET-medewerkers, het EUROfusion MST1-team, het ASDEX Upgrade-team en het DIII-D-team, Multi-device study of temporal characteristics of magnetohydrodynamic modes initiating disruption, 2020, Fusion Engineering and Design, ***160C****, 111945.*

Zusammenfassung

Fusionsplasmen, die magnetisch in Tokamaks eingeschlossen sind, erfahren häufig Störungen, d.h. plötzliche Verluste des Plasmaeinschlusses, bestehend aus einem schnellen thermischen Quench, gefolgt von einem Quench des Plasmastroms, begleitet von der Destabilisierung der vertikalen Position der Plasmasäule. Diese Disruptionen stellen eine ernsthafte Bedrohung für die Maschine in Bezug auf hohe Wärme- und Teilchenströme auf die dem Plasma zugewandten Komponenten und resultierende Kräfte auf alle Bauteile dar. Ihre Vermeidung, Vorhersage und Minderung ist eine Voraussetzung für einen sicheren, effizienten Betrieb großer Tokamaks (z.B. ITER, zur Zeit im Aufbau). Das Einsetzen von Disruptionen steht im Zusammenhang mit der Entwicklung magnetohydrodynamischer (MDH) Moden. Insbesondere das Überschreiten eines Schwellenwerts der Modenamplitude wurde in der Vergangenheit als der entscheidende Auslöser von Störungen identifiziert (de Vries, 2011). Diese Arbeit befasst sich mit mehreren Aspekten der Störungsvermeidung und -vorhersage auf der Grundlage der Überwachung der MHD-Moden-Amplitude. Die Diagnostiken zur Überwachung der Modenamplitude bestanden aus magnetischen Sensoren, speziell aus Sattel und Mirnov Spulen. Als Hauptarbeitsinstrument diente eine große ($>$ 1100 Einträge) Datenbank von Plasmaentladungen, die durch eine Disruption terminiert wurden. Die Datenbank besteht aus Einträgen von mehreren Maschinen, mit unterschiedlichen Plasma-Volumina, aber vergleichbarem Aspektverhältnis (COMPASS, ASDEX Upgrade, DIII-D, JET). Identische Kriterien zum Auswählen der Daten wurden für die Erstellung der Datenbank bei allen Maschinen angewendet. Alle Fälle wurden manuell nach der Hauptursache, die zum Einsetzen der MHD-Mode führte, klassifiziert. Frühere Arbeiten berichteten, dass bei großen Maschinen die meisten Moden im Laborrahmen statisch ("gesperrt") waren (de Vries, 2016). Häufig wird beobachtet, dass sich die Moden vor der Sperrung drehen, was ebenfalls in der kompilierten Datenbank beobachtet wurde. In dieser Arbeit werden wichtige Merkmale im Zusammenhang mit dem Beginn der Störung behandelt, sowohl für rotierende als auch für gesperrten Moden. Die Entwicklung der Modenamplitude wird während der Bremsung der Mode, der stationären Phase und dem Einsetzen der Disruption nachverfolgt. Beobachtungen in dieser Arbeit können zu Designkriterien für zukünftige Vorhersagemodelle von Disruptionen beitragen. Diese Dissertation erforscht sowohl existierende physikalische Modelle für die Beschreibung der Modendynamik als auch eine phänomenologische Beschreibung des Modenverhaltens basierend auf der Multi-Maschinen-Datenbank.

Der erste Ergebnisteil der Arbeit beschreibt eine explorative Studie, die darauf abzielt, ein Modell für die Sperrung der Mode zu validieren. Dieser Teil basiert auf einer auf ASDEX Upgrade beschränkten Datenbank. Das Modell unterscheidet nicht zwischen Plasmakonfigurationen und erlaubt, die Dauer der Abbremsphase sowie die kritische Modenbreite für die Blockierung abzuschätzen. Beide Größen sind wichtig für den Entwurf von Algorithmen, die darauf abzielen, die Disruption mittels eines Sets von externen Aktoren zu vermeiden. Die auf ASDEX Upgrade beschränkte Datenbank besteht aus Entladungen mit verschiedensten Plasmaparametern und Entladungsszenarien. Es stellte sich heraus, dass das Modell

erfolgreich die Blockierung großer Moden in den Fällen beschreibt, in denen die Abbremsung der Moden in einer quasi-stationären Phase der Entladung beginnt (d.h. mit geringer Variabilität des globalen Plasmadrehimpulses vor der Modeneinschränkung) und in denen die Abbremsung über zeitliche Intervalle erfolgt, die lang im Vergleich zu der Impulseinschlusss zeit sind. Die mit dem Modell vorhergesagten theoretischen Bremskurven und Blockierungsdauern waren in guter quantitativer Übereinstimmung mit dem Experiment. Andererseits konnte das Modell die Bremskurven von Moden nicht reproduzieren, wenn sie gegen Ende einer transienten Phase auftreten, wie z.B. während des Einstroms von Verunreinigungen oder bei Annäherung an die Dichteobergrenze. Daraus kann geschlossen werden, dass die Moden nicht die Hauptursache für die Verluste des Plasmaimpulses im Rahmen des Modells waren. Es wird eine modifizierte Bewegungsgleichung der Moden vorgeschlagen, die die transiente Variation der Plasmadichte, z.B. während der Entwicklung eines MARFE und seiner poloidalen Destabilisation von seiner stabilen Position am Plasma X-Punkt, berücksichtigt. Die experimentellen und theoretischen Bremskurven der Moden zeigen eine bessere Übereinstimmung bei Verwendung des angepassten Modells.

Der zweite Ergebnisabschnitt des Dokuments konzentriert sich auf die Analyse der Dauer der gesperrten Moden und des prädisruptiven Wachstums der gemessenen Amplitude der Mode. Es wird auch versucht, eine Regressionsanalyse der Dauer der Phase mit der verriegelten Mode durchzuführen und eine zuvor abgeleitete Skalierung für die Amplitude der disruptiven Mode anzuwenden (de Vries, 2016). Die Studie wurde unter Verwendung der vollständigen Datenbank der disruptierten Entladungen durchgeführt. Dabei wurde ein breites Spektrum von Plasmaparametern inklusive verschiedener Plasmadimensionen abgedeckt. Die gemessene Andauer der verriegelten Moden erstrecken sich bei allen Geraten über mehrere Größenordnungen, aber die Parametermediane steigen mit der Plasmagröße. Mehrere Faktoren, die die Dauer der gesperrten Mode beeinflussen konnten werden diskutiert, wie z.B. die Reaktion des Plasmasteuerungssystems auf Ausnahmesituationen (z.B. An- und Ausschalten externer Heizungsmodule, Einleitung eines schnellen Plasmastromabfalls, Modifizieren der Plasmaform), die spezifischen Eigenschaften des Plasmas innerhalb des typischen Parameterraums der Maschine (die sich oft in der Zugehörigkeit zu einer Störungsklasse widerspiegelt) und das Auftreten kleiner disruptiver Ereignisse (begleitet von einem teilweisen Verlust des Plasmaeinschlusses). Es wird berichtet, dass die Skalierungsformel für die Disruptionsmodenamplitude die experimentellen Amplituden systematisch überschätzt, falls die Mode mit magnetischen Sensoren auf der Hochfeldseite des Torus erfasst wird. Ein Vorschlag für eine auf diesen Fall angepasste Skalierungsformel wird vorgestellt. Die modifizierte Gleichung ermöglicht eine genauere Bestimmung der kritischen Modenamplitude. Eine lineare Extrapolation bezüglich der Plasmagröße, der experimentell erfassten und der vorhergesagten Zeit bis zur Disruption und dem damit verbundenen Bruchteil von tatsachlichen Disruptionen lasst vermuten, dass bei Geräten, in denen der kleine Plasmaradius groß ist, die gesperrten Moden auf Zeitskalen wachsen, die für die Störungsminderung durch schnelle massive Gas- oder Pelletinjektion vorteilhaft sind. Eine hohe Erfolgsrate der Mitigation von Disruptionen, wie sie für den Hochleistungsbetrieb von ITER gefordert wird, sollte jedoch durch ein mehrstufiges Störungsvorhersagegerät unterstützt werden. Eine Regressionsanalyse, die darauf abzielt, eine Skalierungsbeziehung von den Plasmaparametern für die Dauer

der Phase mit einer gesperrten Mode herzustellen, hat eine Skalierungsformel ergeben, deren Vorhersagekapazität von großen Unsicherheiten beeinträchtigt ist. Die Ursachen der Streuung, wie z.B. das Einsetzen kleiner Disruptionen im Beisein der Mode oder das erneute Rotieren der Mode unter konstantem externen Torque, werden diskutiert. Die Anwendung der hier abgeleiteten Skalierung auf das ITER-Basisszenario lässt vermuten, dass die Dauer der Phase mit einer gesperrten Mode bei ITER je nach Disruptionsursache in der Größenordnung von einigen Hundert Millisekunden bis einigen Sekunden liegen wird, was zu Gunsten einer rechtzeitigen Mitigation der Disruption in ITER spricht.

Teile des Abschnitts. 2.5.2, Abschnitt. 2.5.3 und Kap. 5 wurden von V. Klevarová, H. Zohm, G. Pautasso, G. Tardini, R. McDermott, G. Verdoolaege, J.A. Snipes, P.C. de Vries, M. Lehnen, das EUROfusion MST1 Team und das ASDEX Upgrade Team, Validation of a Tearing Mode Locking Model Using a Database of Disruptive Plasmas at ASDEX Upgrade, 2019, Plasmaphysik und kontrollierte Fusion, ***62****(2) 025024.*

Teile von Kap. 4 und Kap. 6 wurden von V. Klevarová, G. Pautasso, P.C. de Vries, R. Sweeney, T. Markoviĉ, H. Zohm, G. Verdoolaege, M. Komm, J. Havlicek, J.A. Snipes, M. Lehnen, JET-Mitarbeiter, das EUROfusion MST1-Team, das ASDEX Upgrade-Team und das DIII-D-Team, Multi-device study of temporal characteristics of magnetohydrodynamic modes initiating disruption, 2020, Fusion Engineering and Design, ***160C****, 111945.*

Contents

1. Introduction

1.1 Challenges of the energy sector

As of the year 2018, young environmental activists around the globe have caught the attention of the mass media and introduced the term 'climate crisis' in the public space. This term responds to the continuation of the global temperature increase and occurrence of extreme weather phenomena. Following the public pressure, the UN Climate Action summit 2019 addressed the challenges of the climate change, presumably linked to the emission of the greenhouse gases accompanying the industrial civilization era. The summit emphasized the need of faster transition to emission-free power sources, since the energy sector is the dominant source of the pollutant gases (Fig. 1.1a).

Hydro, solar, wind and nuclear fission power plants are considered emission-free during their operation, but represent only a minority of the current power sources (Fig. 1.1b). Hydro-based power plants are capable of a large scale, continuous energy delivery, but bring an irreversible change to the environment. Furthermore, a long term drought brings a risk to their operation. Wind and solar power plants operate non-continuously and the current power banks are unable to store large amounts of energy that can be produced in those plants under favourable weather conditions. The fission reactors are capable of a continuous, scalable electricity production. The public, however, often expresses concerns in terms of the safety measures and storage of the highly radioactive burned fuel.

The global demand for the electricity production is increasing. Combined with the accent on the emission-free power sources, the need for harnessing the energy released during the nuclear fusion increases.

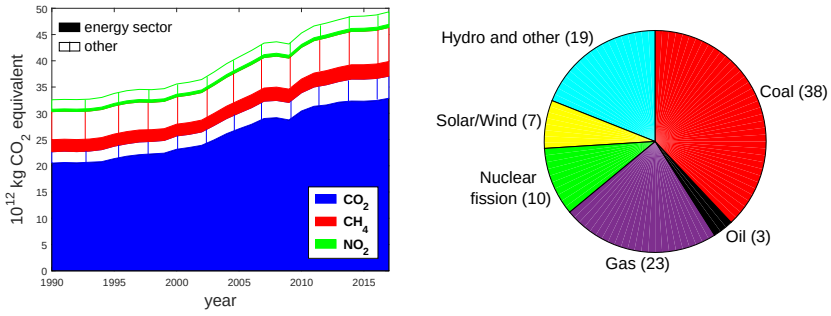

(a) (b)

Figure 1.1: *(a) Global evolution of the greenhouse gas emissions. (b) Mix of the electricity generation, year 2018 (percentages are given in parentheses). Figure data were adopted from [1, 2], respectively.*

1.2 Thermonuclear fusion and the tokamak concept

A clear public demonstration of the fusion reaction potential in terms of the energy release was the launch of the hydrogen Tsar bomb (in former Soviet Union, 1961) that caused so far the most powerful human-triggered explosion on the Earth. Peaceful applications of the fusion reactions have been globally, nevertheless, explored since 1940's.

Nuclei merge together during the fusion process. The nucleus mass is not a simple sum of proton and neutron masses forming it. The mass defect, Δm_{fusion}, the difference between the sum of the reactant masses m_1 and m_2 and the mass M of the final product can be calculated as

$$\Delta m_{\text{fusion}} = m_1 + m_2 - M. \tag{1.1}$$

With $m_1 + m_2 > M$, $\Delta m_{\text{fusion}} > 0$ and the Einstein's mass-energy equivalence yields the energy released during the fusion reaction, ΔE_{fusion},

$$\Delta E_{\text{fusion}} = \Delta m_{\text{fusion}} c^2. \tag{1.2}$$

The liquid drop model of nucleus allows calculating the nucleus binding energy B, i.e. the energy needed to separate the nucleus into nucleons [3]. Of particular interest is this quantity normalized to the mass number A, yielding the binding energy per nucleon B/A. Fig. 1.2a displays this quantity as a function of A, with the maximum located at $A = 62$. Exothermic reactions, of interest within the scope of the positive energy gain, are located at $A < 62$ and of interest are reactions with the highest energy gain, i.e. those with significant difference between $B/A_{\text{reactants}}$ and B/A_{products}. The following reaction between deuterium and tritium has the highest cross-section for a large range of deuterium energies [4]:

$$\text{D} + \text{T} \rightarrow {}^{5}\text{He}\,(17.6\,\text{MeV}) \rightarrow {}^{4}\text{He}\,(3.6\,\text{MeV}) + \text{n}\,(14.0\,\text{MeV}) \tag{1.3}$$

and it is thus considered as the main fusion reaction to be explored during high performance experimental campaigns in reactors specially designed for handling the reactants (one of which is radioactive, see below). Concerning the reactant sources, deuterium is a naturally abundant element, present in the seawater. Tritium sources are mainly human-produced, for example, the isotope is a secondary product in some of the fission power plants. Total estimated amount of tritium on Earth is only several tens of kilograms, its sources are thus rare. It can be, however, bred within the fusion reactor through the interaction of the produced neutron and lithium stored in the blanket surrounding the confining vessel. Lithium is another naturally abundant element. Natural sources for the fusion reaction (1.3) are thus virtually inexhaustible.

Tritium is a radioactive element with a half-time decay constant of ~ 12.3 years. The fusion power plant designs account for keeping the tritium within a closed loop, in amounts not exceeding few kilograms. Furthermore, ^{4}He, the product of the (1.3) reaction, is a stable isotope. Concerning the radioactive waste of the fusion reactors, the reactor first wall is of concern since its components will get activated during the reactor operation. Current material research for fusion applications focuses on development of low-level activated materials that should mitigate the negative impacts of radioactive components.

In summary, the advantages of the fusion power plants are the following:

- greenhouse gas emission-free concept,
- virtually inexhaustible fuel source,
- large energetic gain of fusion reactions,
- no risk of melt-down events (since no chain reaction takes place),
- short radioactive decay time of the activated waste.

It could thus represent a safe, environmentally friendly and sustainable power source.

Fusing nuclei have to overcome the mutually exerted repulsive Coulomb force. This can happen under favourable conditions in terms of their high energy (temperature) and collision conditions (density), forcing the reactants to be in a plasma state. The *ignition*, the independence of the fusion process on the external power input, can be achieved once the so called Lawson criterion, practically formulated in terms of a triple product of the plasma density n, temperature T and the energy confinement time τ_{E} (defined as a measure of the system energy loss to 1/e of its initial value) is fulfilled [5]:

$$nT\tau_E > 3 \cdot 10^{21}\,\mathrm{m}^{-3}\mathrm{keVs} \tag{1.4}$$

For a D-T reaction, the typical order of magnitudes are $n \sim 10^{20}$ m^{-3} and $T \sim 10$ keV[1] for the criterion fulfilment. No material can sustain a direct contact with a matter of such a high temperature. The charged particles can be, however, kept away from the confining vessel with the use of magnetic fields, defining thus the concept of the *magnetic confinement*.

The most advanced member of the magnetically confining fusion reactors group is a *tokamak* of a typical donut shape (Fig. 1.2b). The magnetic field configuration is a result of superposition of two components: coils surrounding the confining vessel produce a field in the toroidal direction, while the plasma current induced by the transformer (of which the plasma is the secondary winding) produces a field in the poloidal direction. The resulting field lines take form of a helix. From this simplified description it follows that the tokamak operation is not continuous since the capacity of the central solenoid is limited. Passage to a continuous operation requires a sophisticated engineering design and a special tailoring of the plasma parameters [6].

Since the plasma resistivity decreases with increasing temperature as $\propto T^{-3/2}$, the ohmic heating of the plasma due to the current flow becomes ineffective at high temperatures. Unless the alpha particles support the plasma heating at the ignition condition, auxiliary heating sources (of total input power P_{aux}) have to be used, such as a beam of neutral particles (NBI, neutral beam injection) or electromagnetic waves injected into the plasma at electron or ion cyclotron frequencies (ECRH and ICRH, electron and ion cyclotron resonance heating, respectively) [8]. Under favourable circumstances, typically at high plasma performance, the plasma can pass to a state characterized by increased energy confinement time and steep gradients of the density and temperature at the plasma edge, the so called H-mode (a high-confinement mode) [9]. In contrast, plasma without the increased confinement time and steep parameter gradients is denoted as an L-mode plasma (a low-confinement mode). Origin of the transition between high

[1] 1 eV $\approx$ 11600 K

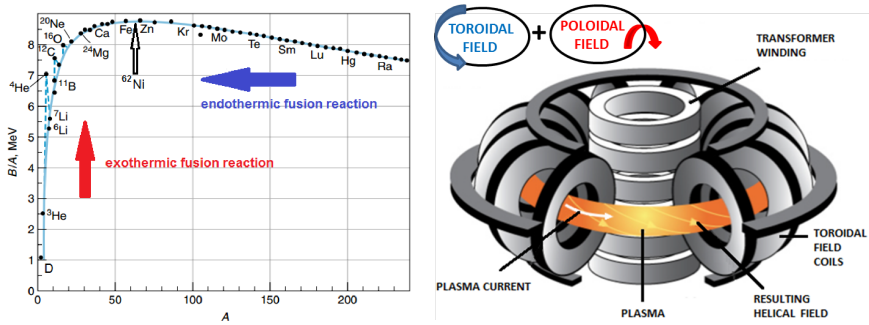

(a) (b)

Figure 1.2: *(a) The nucleus binding energy per nucleon. Areas of exo/endothermic fusion reactions are highlighted. The curve reaches maximum at $A = 62$. Figure taken from [3]. (b) Tokamak schematic drawing [7].*

and low-confinement modes is complex [10] and not fully understood. Among other phenomena, macroscopic instabilities developing in the plasma, introduced in Sec. 1.4 and theoretically treated in Chap. 2, are observed to initiate the transition.

Tokamak operation at high plasma performance is challenging both from the engineering and physics points of view. Some of the challenges will be addressed in this thesis.

1.3 The ITER project

The fusion power scales roughly with the third power of the major tokamak radius [11]. To demonstrate feasibility and economical viability of the fusion, an experimental tokamak of unprecedented dimensions, the tokamak ITER (Fig. 1.3), is currently under construction in France. Its main scientific mission will focus on producing more fusion power gain than will be the auxiliary power input, by a particular factor ≥ 10, during a temporal period of $\sim$ 300-500 s. Besides that, a continuous operation schemes at positive energy gain will be tested.

The first plasma operation is currently scheduled for December 2025. The first D-T campaign should take place in 2035. In summer 2020, about 70% of the total work scope related to the first plasma operation was completed. [12].

1.4 Threats of the sudden plasma confinement loss

Sudden losses of the plasma confinement, the so called disruptions, are ordinarily accompanying the tokamak operation. Those events are primarily caused either by a destabilization of the plasma column position or the development of macroscopic instabilities that reach a certain threshold amplitude [14]. Conveniently, the magnetohydrodynamic theory (MHD), that treats plasma as a single conducting fluid interacting with magnetic fields, is used to describe theoretically the

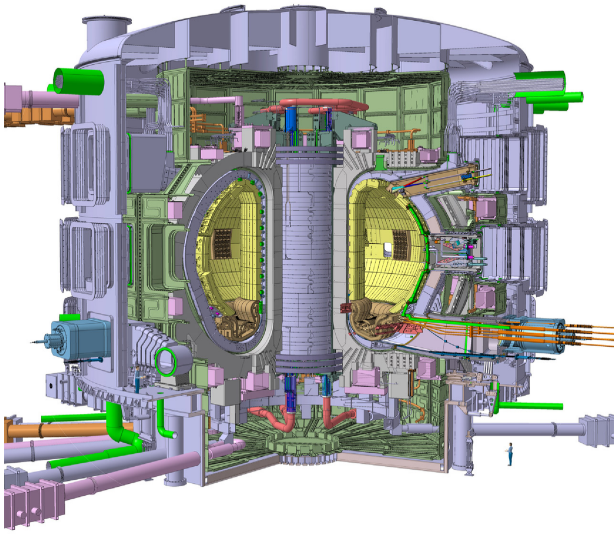

Figure 1.3: *3D drawing of the ITER tokamak [13]. Device engineering parameters are listed in Tab. 3.1.*

onset and development of the (disruptive) modes.

There are multiple threats related to the discharge termination by a disruption. Firstly, once the plasma gets destabilized in position, it can come in physical contact with the conducting vessel. A so called 'halo' current (shown to carry 10-40% of the plasma current in Ref. [15]) can flow in the poloidal direction (via a loop composed of the plasma and vessel), resulting in a substantial electromagnetic force applied on the device structural components. Ref. [16] reports that in high-performance large tokamaks the pressure on the vessel can be of the order of tens of tonnes per square meter. Secondly, the plasma facing components can be subjected to large heat loads during the disruption. Those can exceed significantly the normal operation levels, melt the plasma facing components [17] and eventually release dust within the vessel interior. Thirdly, a beam of so called 'runaway' electrons of relativistic energies can be generated during the disruption [18, 19] and their impact on the first wall can be damaging. The current carried by the runaway beam can reach a substantial fraction of the disrupting plasma current and the damaging potential of the runaway beam is thus increased for high performance plasma operation conditions.

In large devices, repair of the components damaged by disruptions can be costly, time-consuming and logistically demanding. It is thus of importance to detect the instabilities in real-time and *predict*, *avoid* and eventually *mitigate* the disruptions in large machines. The corresponding schemes must be implemented in the device plasma control system (PCS) [20]. Beside the eventual damage, the instabilities can reduce the plasma performance, wasting thus the device experimental potential. In future power plants, the fusion power output might be reduced due to this reason. Detection of the instabilities and their physical reduction can be complementary with the disruption avoidance schemes.

In the scope of disruption avoidance, the PCS aims to restore the plasma performance (by, for example, stabilization of a detected MHD mode) and keep it within pre-defined operational conditions unfavourable for the disruption onset. A set of plasma diagnostic instruments is used in real-time for this purpose, together with a number of actuators (such as external heating modules) executing the PCS actions. The disruption prediction task is to recognize an imminent disruptive event and initiate the mitigation action. This can consist for example of a fast current ramp-down initiation or a quick vacuum vessel filling by a radiating medium. Time sampling of the plasma control system and the radiative medium filling modules sum up in a reaction time necessary for the disruption mitigation.

Requirements on the predictor efficiency and reliability are, in case of large devices of high performance, rather severe. In the ITER case, an operation window in terms of the plasma current and energy has been defined for which the reliability of the disruption detection (within the minimum allowed reaction time) must be very high. In case of plasmas of the highest performance, the number of detected and mitigated disruptions must nearly approach 100%, since only limited number of events disrupting those plasmas are allowed in the view of the protection of device plasma facing and structural components [20]. On the other hand, premature, or even 'false' alarms (i.e. the disruption predictors raises an alarm, whereas no disruption would have developed) must be very low, because every mitigation action in the devices of the ITER size requires time consuming chamber pumping and vessel conditioning, resulting thus in the waste of the device operational potential. A balance between the amount of unmitigated and falsely detected disruptions must be found, in accordance with the engineering requirements in terms of the expected life time of device components and the costs of the machine shut-down periods.

Anomalous, potentially disruptive, plasma conditions were shown to be recognized with high prediction success rate and low number of false alarms by using advanced machine learning algorithms [21–24]. Number of diagnostic signals, indicating the upcoming disruption, are typically fed to those so-called *data-driven* schemes. The algorithms are tailored to be independent of a particular discharge operational scenario, which should allow their universal applicability within the machine operation space. This universal application, as well as the algorithm device-to-device portability (a desirable property in the view of its application in the future devices), is, however, rather limited. In addition, a large initial set of both disruptive and non-disruptive discharges is typically necessary for the algorithm initial training. For high-performance plasmas, collection of unmitigated disruptions might be troublesome due to unacceptable risk of the component damage.

Generalization of the data-driven predictors might be supported by the input from *physics-driven* schemes that carry information (provided by empirical scalings and models) about the physical mechanisms driving the disruption onset. Currently, amount of such information sources is limited. Derivation of new models describing the disruption development and validation of some of the existing scalings/models will represent the main goal of this thesis.

1.5 Outline of the Thesis

To achieve this goal, i.e. to provide additional input to the (existing) physics-driven models and scalings, applicable in the disruption forecasting, it was decided to assemble a large, multi-device database of disruptive discharges. The database will serve as a main working tool in the scope of this thesis. The database consists of entries pertaining to devices of various plasma size (COMPASS, ASDEX Upgrade, DIII-D, JET), but similar plasma minor to major radii ratio. The discharges originate from broad range of plasma and discharge scenarios, allowing thus to study the disruption development under various plasma conditions. All cases were manually classified according to the main cause leading to the onset of the MHD instability. Under multiple circumstances, the observations will be discussed in the context of the disruption root cause.

This thesis investigates several aspects of disruption forecasting based on monitoring of the MHD mode amplitude detected by magnetic sensors. Focus on this particular diagnostic signal is motivated by the fact that MHD modes are observed to be the principal disruption triggers and the magnetic measurements are relatively simple (installed in most of the existing devices), yet robust.

Ref. [14] showed that in large devices, the instabilities were usually static in the laboratory frame ('locked') at the disruption onset. Often, modes are, however, observed to rotate prior to locking. It was shown that the mode rotation can support its stabilization [25–27]. Studies focused on disruption forecasting and avoidance are thus often investigating the mode braking phenomenon. Here, important characteristics of both rotating and locked modes are investigated.

In particular, this thesis addresses in its two result chapters (Chap. 5 and Chap. 6) the following research topics:

- Chap. 5 focuses on validation of a previously derived [28,29] model for locking of an initially rotating instability. With the model, it is possible to calculate the instability braking duration and the critical amplitude at which the locking occurs. Both quantities are important in the context of the disruption avoidance, since the PCS might, provided that this information is supplied to it, tailor the action aiming at avoiding the instability locking. Like that, disruption can be prevented and an optimum plasma confinement can be restored. Since the tokamak plasma parameters are often set close to various disruptive operation borders, it is of interest to validate the model for a large set of discharges, thereby considering a broad variety of operational scenarios, plasma parameters, discharge phases, as well as root causes for instability seeding and details of the amplitude growth. The model predictions will be confronted with the experimental measurements (restricted to the ASDEX Upgrade part of the database) and if a discrepancy is encountered, its origins will be examined.
- As stated above, instabilities are often static prior to the disruption onset. Currently, no analytical model allowing a universal calculation of the locked mode duration (ideally in real-time during the discharge) exists. This parameter would yet represent another important information for the PCS action in the context of the disruption forecasting. Based on the estimate of this parameter (and combined with a real-time measurement of the mode amplitude), the PCS might decide whether to initiate the disruption mitigation action and/or aim at reducing the instability amplitude by means

of external actuators. In Chap. 6 the full database is used to analyse the experimental locked mode durations. The typical pre-disruptive growth of the mode measured amplitude is examined and the experimental characteristics are discussed in the context of a typical PCS reaction time. In the chapter, it is also attempted for regression analysis of the experimental locked mode duration. Predictions of this parameter in the ITER high performance scenario, based on a newly derived scaling, are presented. Finally, a previously derived empirical formula for the disruptive mode amplitude, presented in Ref. [14], is applied on the database and the observed discrepancies between predictions and measurements are examined. The adjusted scaling is then used to explore predictions of the time available for the PCS disruption mitigation action in the four devices.

The above points indicate that Chap. 5 will focus on a validation of a physical model that describes the mode locking, a phenomenon that frequently precedes the disruption onset. Only a reduced database of ASDEX Upgrade discharges will be used for this purpose, but given the fact that this reduced database will cover an extensive range of various plasma parameters (such as density), it might be assumed that the loss of generality of the here performed model validation will be minor. Chap. 6 then analyses the locked pre-disruptive mode duration (and growth) for the full set of discharges. Usage of the full database is motivated by the attempt for the phenomenon description under an extended range of certain parameters (such as the plasma size and current). Given the complexity of the underlying causes that determine the mode duration and growth (within the broad plasma parameter and discharge scenario range), an empirical approach is adopted in the chapter. Both Chap. 5 and Chap. 6 consist of a motivation, result and discussion sections.

Sec. 1.4 mentions that the main properties of the modes are described with the MHD theory. Key definitions and mode properties introduced by this theory (including the model for instability locking, Sec. 2.5.3) are contained in Chap. 2.

Chap. 3 presents basic information concerning the necessary experimental setup. In particular, it introduces terms related to the measurement of the mode amplitude, as well as measurements of important plasma parameters, such as temperature and density. It also provides the main characteristics of devices examined in this study.

The description of the database assembly, filtering, calculation of the key plasma parameters at important discharge time points and the analysis of the instability seeding cause (i.e. the details of the disruption classification) are contained in Chap. 4.

The result section, as mentioned above, consists of Chap. 5 and Chap. 6. The overall thesis summary is provided in Chap. 7.

2. Theoretical background

The magnetohydrodynamic theory (MHD) describes mutual interaction of magnetic fields and electrically conducting fluids. In the following, the plasma is treated as a conducting single fluid interacting with magnetic fields, i.e. a simple fluid dynamics is combined with the electrodynamic equations [30–32]. Basic MHD equations will be presented in Sec. 2.1.1, followed by conditions simplifying MHD to its ideal and resistive forms. Theory validity will be discussed in Sec. 2.1.2. In Sec. 2.2, ideal MHD approach will be adopted and the MHD equilibrium in toroidal configuration (typical of the tokamak) will be presented. Destabilization of ideal kinks and resistive tearing modes will be discussed in Sec. 2.3.1 and Sec. 2.3.2, respectively. Sec. 2.4 provides a phenomenological description of the disruption. Sec. 2.5 will focus on basic terms related to rotating (Sec. 2.5.1) and locked (Sec. 2.5.4) MHD modes. It will also present a model for mode braking (Sec. 2.5.3), built upon examination of properties of field characteristic of a mode rotating in a resistive wall vicinity (Sec. 2.5.2). Content of this chapter will be mainly based on a literature overview, with the exception of parts of Sec. 2.5.2 and Sec. 2.5.3.

2.1 Introduction of the MHD theory

2.1.1 Basic MHD equations

Assuming the plasma, an electrically conducting single (constituted both by electrons and ions) fluid, to be quasineutral ($n_e = n_i = n$) and in a local thermodynamic equilibrium, it can be at any point in space $\boldsymbol{r}$ and at any time t of its state specified by its mass density $\rho \simeq m_i n = mn$, temperature T ($T_e = T_i = T$) and velocity $\boldsymbol{v}$. Starting from the Ampère's law,

$$\nabla \times \boldsymbol{B} = \mu_0 \boldsymbol{j}, \tag{2.1}$$

(where, assuming a non-relativistic limit, the displacement current was neglected), Maxwell-Faraday's law,

$$\frac{\partial \boldsymbol{B}}{\partial t} = -\nabla \times \boldsymbol{E}, \tag{2.2}$$

resistive form of the Ohm's law (simplified as Hall term, electron inertia, gradients in electron pressure etc. are omitted),

$$\boldsymbol{j} = \sigma(\boldsymbol{E} + \boldsymbol{v} \times \boldsymbol{B}), \tag{2.3}$$

and given the non-existence of magnetic monopoles, expressed by the Gauss's law for magnetism,

$$\nabla \cdot \boldsymbol{B} = 0, \tag{2.4}$$

the induction equation for the case of an electrically resistive fluid can be retrieved by eliminating the electric field $\boldsymbol{E}$ and electric current density $\boldsymbol{j}$,

$$\frac{\partial \boldsymbol{B}}{\partial t} = \nabla \times (\boldsymbol{v} \times \boldsymbol{B}) + \eta \nabla^2 \boldsymbol{B}, \tag{2.5}$$

where $\eta = 1/\mu_0\sigma$ stands for the magnetic diffusivity (temperature dependence of conductivity, σ, is omitted). This formula describes the evolution of magnetic field $\boldsymbol{B}$ for a given velocity field of the fluid. Newton's second law for a fluid element,

$$\rho\frac{d\boldsymbol{v}}{dt} = \boldsymbol{F},$$

expresses the equation of motion of a fluid subjected to forces, represented by the right side of the formula. The left side contains the fluid mass multiplied by the acceleration seen by the moving fluid element, given by the convective derivative

$$\frac{d\boldsymbol{v}}{dt} = \frac{\partial\boldsymbol{v}}{\partial t} + \boldsymbol{v}\cdot\nabla\boldsymbol{v}.$$

The forces exerted on the fluid volume can be for example the Lorentz force $\boldsymbol{j}\times\boldsymbol{B}$, the pressure gradient force $-\nabla p$, gravity ρg (g being the gravitational constant) and the viscous force $\nabla\cdot\underline{\boldsymbol{S}}$, where $\underline{\boldsymbol{S}}$ is the viscous stress tensor. The MHD momentum equation then takes the form

$$\rho\frac{d\boldsymbol{v}}{dt} = \boldsymbol{j}\times\boldsymbol{B} - \nabla p + \rho g + \nabla\cdot\underline{\boldsymbol{S}}. \tag{2.6}$$

Conservation of plasma mass is described by the continuity equation (no sources nor sinks of plasma are assumed),

$$\frac{\partial\rho}{dt} + \nabla\cdot(\rho\boldsymbol{v}) = 0, \tag{2.7}$$

expressing that the rate of change of fluid mass in an elementary volume equals the mass flux into it. Finally, the set of equations is enclosed by the energy equation, simplified into the adiabatic form in case that the heating mechanisms do not affect pressure nor volume of the fluid's element:

$$\frac{d}{dt}\left(\frac{p}{\rho^{\gamma_0}}\right) = 0, \tag{2.8}$$

with γ_0 being the heat capacity ratio. Formulae presented above form a set of MHD non-linear equations, coupled in unknowns $(\boldsymbol{E}, \boldsymbol{j}, \boldsymbol{B}, \boldsymbol{v}, \rho, p)$.

Two branches of MHD are typically recognised, depending on the relative importance of plasma motion to the magnetic diffusion in the temporal evolution of the magnetic field, expressed by the magnetic Reynold's number R_m. This quantity is calculated as a ratio of terms on the right hand side of the induction equation, Eq. (2.5). The convective and diffusion term can be approximated with the typical length scale L and velocity v, yielding

$$\frac{\nabla\times(\boldsymbol{v}\times\boldsymbol{B})}{\eta\nabla^2\boldsymbol{B}} \approx \frac{vB/L}{\eta B/L^2} = \frac{vL}{\eta} = R_\mathrm{m}. \tag{2.9}$$

In the perfectly conducting limit, $R_\mathrm{m} \gg 1$, the induction equation becomes

$$\frac{\partial\boldsymbol{B}}{\partial t} = \nabla\times(\boldsymbol{v}\times\boldsymbol{B}), \tag{2.10}$$

a constitutional equation for the *ideal MHD* with the typical time scales given by the inverse of the Alfvèn velocity $v_\mathrm{A} = B/\sqrt{\mu_0\rho}$,

$$\tau_\mathrm{A} = \frac{L}{v_\mathrm{A}}. \tag{2.11}$$

In this limit, a frozen-flux theorem holds, stating that the magnetic flux through any closed circuit, moving with the local fluid velocity, is constant in time, i.e. the magnetic field lines behave as they move with the plasma and the magnetic field is thus 'frozen' with respect to the plasma [33]. An important consequence of the flux conservation is the fact that the magnetic field topology forms an invariant, i.e. the magnetic field lines cannot intersect, as this would affect the flux tube topology.

In the *resistive MHD limit*, $R_{\mathrm{m}} \ll 1$, the induction equation becomes a diffusion equation,

$$\frac{\partial \boldsymbol{B}}{\partial t} = \eta \nabla^2 \boldsymbol{B}, \tag{2.12}$$

with the field variations/currents diffusing away over a resistive diffusion time scale τ_{R},

$$\tau_{\mathrm{R}} = \frac{\mu_0 L^2}{\eta}. \tag{2.13}$$

The resistive diffusion allows for breaking of the field lines topology via the reconnection phenomenon [34, 35]. A simple model for magnetic reconnection is illustrated in Fig. 2.1. Initially, an equilibrium between two anti-parallel fields is assumed, with a built-up current sheet, across which the field reverses. An initial perturbation might create regions of larger magnetic pressure and owing to the finite resistivity, magnetic field diffuses faster in the region of larger density of the field lines (i.e. in the region of strong ∇B). Diffusive process reduces the magnetic pressure and in the end the opposing field lines can be 'cut' in half and reconnect (with a sharp bending through the current sheet), with a resulting tension forces (in the horizontal direction as shown in the figure). Owing to the tension forces, plasma can be accelerated along the current sheet and be expelled at high speed on both sides of the diffusion region. Process of reconnection thus converts the magnetic energy into the thermal (via Ohmic dissipation due to finite resistivity) and kinetic energy. This phenomenon can occur also in highly conducting plasmas, assuming that the plasma resistivity is finite only in the vicinity of the current sheet.

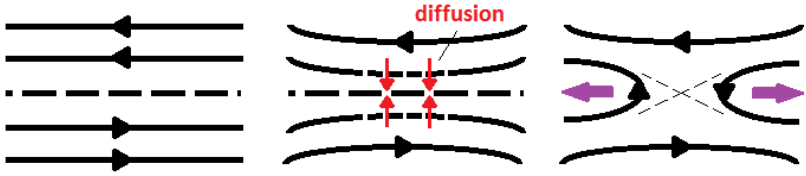

Figure 2.1: *Illustration of the magnetic reconnection phenomenon.*

2.1.2 Conditions of validity

Treating the plasma as a single fluid requires that it is collision dominated, i.e. the mean free path, λ_{mfp}, between the collisions must be much smaller than the typical plasma length scale L. Same applies for the Debye length λ_D, assuring the plasma to be quasineutral. In case that the plasma size exceeds the ion Larmor radius, $r_{\mathrm{L,i}}$, significantly, Hall and electron diamagnetic effects, included in the

electron momentum equation, can be omitted. The electron inertia is thus no longer considered separately and plasma can be treated as a single fluid in MHD. Restrictions on the required length scales can be summarised such that

$$\lambda_{\mathrm{mpf}}, \lambda_{\mathrm{D}}, r_{\mathrm{L,i}} << L.$$

Unlike is in the direction perpendicular to the field line, the condition is often not satisfied for mean free path parallel to the field line, where λ_{mfp} can become very large in hot plasmas, thus well exceeding the plasma length scale L. Further conditions require that the typical plasma time scales are long enough to allow plasma species to reach the equilibrium state and that the frequency of events concerned in the MHD theory are much lower than the characteristic plasma frequency and electron/ion cyclotron frequencies.

Those conditions imply that MHD concerns macroscopic, low-frequency, long-wavelength phenomena occurring in plasma. Using MHD, conditions of macroscopic force balance can be well described, together with the system dynamics. The theory can be also successfully used for prediction of the stability and development of large scale instabilities (modes) in magnetically confined plasmas in fusion reactors of complex geometrical configurations.

2.2 Ideal MHD equilibrium in toroidal geometry

In a steady state limit, $\partial/\partial t = 0$, and with an assumption of zero plasma velocity, $v = 0$, the momentum equation, Eq. (2.6), simplifies to

$$\nabla p = \boldsymbol{j} \times \boldsymbol{B}, \tag{2.14}$$

describing the *magnetostatic equilibrium* (gravitational and viscous forces were neglected). In particular, Eq. (2.14) expresses the balance between plasma pressure and forces due to magnetic fields and it implies that $\boldsymbol{B} \cdot \nabla p = 0$, forbidding thus the existence of pressure gradient along the field lines (i.e. magnetic surfaces are surfaces of constant pressure). Moreover, $\boldsymbol{j} \cdot \nabla p = 0$ holds, implying that the current field lines lie on the isobaric surfaces.

An analytical solution of Eq. (2.14) (in the limit of perfectly conducting plasmas) can be found in case of plasma confined in linear geometrical configuration, such as that of a *theta* (Fig. 2.2a) or *Z-pinch* (Fig. 2.2b). In the former case, the plasma confinement is achieved via an axial magnetic field and poloidal current. Theta pinch represents a stable configuration, since bending or compression of the axial field lines is counteracted by the field tension force. On the other hand, it suffers from particle end losses. In the latter case, the pinch confines plasma via an axial current and a self-generated poloidal magnetic field. Equilibrium pressure profile is parabolic and its maximum achievable value is dependent on the total plasma current I_{p} (independent of the current density profile) quadratically and increases with the decreasing plasma minor radius a as $\propto a^{-2}$. Intensity of the magnetic field increases with the plasma radius, however, confinement is assured via the field line tension pointing inwards. Due to the closed nature of the field lines, theoretically, Z-pinch does not suffer from the end losses. However, in case that the plasma channel is locally compressed/bent, resulting gradient of the

magnetic pressure will generate a radial force, enhancing the initial perturbation and resulting in instabilities such as sausages and kinks, illustrated in Fig. 2.2c.

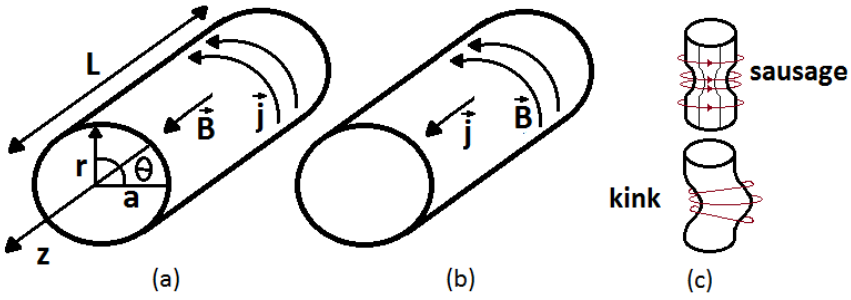

Figure 2.2: *a) Geometry of the theta pinch, b) Z-pinch and c) illustration of sausage and kink instabilities in the linear plasma configuration.*

The system can be stabilized with addition of an axial field to the Z-pinch configuration, with resulting helical nature of the field lines. Such geometry defines a *screw pinch*. Maximum pressure is independent of the plasma radius, on the other hand, the screw pinch suffers from end losses due to the field line geometry. Solution of this problem might be to enclose the cylinder ends in itself, passing thus into an axisymmetric 2D toroidal geometry, i.e. the configuration typical of the tokamak. Fig. 2.3a displays a resulting geometry of flux surfaces forming a set of nested toroids. Note that the angle ϕ represents a toroidal coordinate that can be ignored, simplifying thus the equilibrium determination to the poloidal plane that can be characterized by set of $\{R, z\}$ or $\{r, \theta\}$ coordinates.

When determining the tokamak equilibrium conditions, a flux function Ψ ($= f(R, z)$) is typically introduced. This function is given by the poloidal flux enclosed within each magnetic surface and is thus constant on the corresponding surface. Components of the magnetic field in the poloidal plane can be expressed with the help of the flux function as

$$B_{\mathrm{R}} = -\frac{1}{R}\frac{\partial \Psi}{\partial z} \text{ and } B_{\mathrm{z}} = \frac{1}{R}\frac{\partial \Psi}{\partial R}. \tag{2.15}$$

Quantities in the further derived equilibrium condition, the so called Grad-Shafranov equation [36],

$$\Delta^{*}\Psi + \mu_0 R^2 \frac{dp(\Psi)}{d\Psi} + F(\Psi)\frac{dF(\Psi)}{d\Psi} = 0, \tag{2.16}$$

are a function of the current flux function $F(\Psi)$,

$$\Delta^{*}\Psi = \frac{\partial}{\partial R}\left(\frac{1}{R}\frac{\partial \Psi}{\partial R}\right) + \frac{\partial^2 \Psi}{\partial z^2}. \tag{2.17}$$

Eq. (2.16) is a second order elliptic partial differential equation, typically solved numerically. One such (non-circular) solution is shown in Fig. 2.3b (exhibiting a reconnection phenomenon introduced in Sec. 2.1.1). Note that the last closed plasma surface in the shaped plasma (characterized by elongation κ and triangularity δ) is denoted as the plasma separatrix.

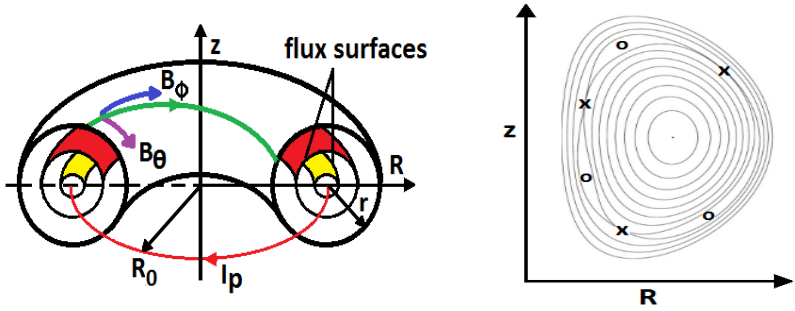

(a) (b)

Figure 2.3: *(a) Tokamak geometrical configuration. Note the nested toroidal flux surfaces. (b) Example of tokamak equilibrium magnetic surfaces. A magnetic island (introduced in Sec. 2.3.2) is located at $q = 3/2$ rational surface (P.R. Garabedian et al., 2010). O and X island points are depicted by 'o' and 'x' symbols, respectively.*

Finally, in tokamak, each magnetic field line can be characterised by the associated value of a safety factor q, defined as a ratio of m toroidal to n poloidal turns travelled per self-enclosing field line ($q = m/n$). Surfaces with rational value of q are called resonant surfaces. In a large aspect ratio A ($A = R_0/a$, R_0 being the major radius) tokamak, safety factor can be approximated as

$$q = \frac{r}{R_0}\frac{B_\phi}{B_\theta}. \tag{2.18}$$

The basic properties of the equilibrium toroidal field B_ϕ can be derived upon using the Ampère's law and evaluation of a circular line integral around a toroidal circuit of radius R within the external toroidal field coils. The resulting expression is the following:

$$B_\phi = \frac{\mu_0 I_\mathrm{p}}{2\pi R}. \tag{2.19}$$

The equilibrium toroidal field thus decays as $\propto 1/R$. At the inner part of the torus the field intensity is stronger than at the outer part, discriminating thus between sides of the high (HFS) and low-field side (LFS) intensities.

2.3 MHD equilibrium stability

Inspection of the equilibrium stability allows to identify conditions under which an initial perturbation grows and ultimately destroys the equilibrium state. To test the stability, one can define a fluid displacement vector and linearise the MHD momentum equation in terms of the displacement vector and a force operator. Whether the applied displacement leads to an unstable situation can be inspected for example via the energy method [6] that examines the resulting change in the plasma potential energy. In case that this decreases, the energy conservation principle, valid in MHD, assures that the kinetic energy increases. Hence, the equilibrium is not stable.

The stability condition is typically decided upon the sign of the potential energy variation, with a positive increment assuring the system stability. Whether the variation is positive or negative depends on amplitude of particular terms included in the force operator. Some of the terms can be negative, hence potentially destabilizing. For example, value of the pressure gradient can support appearance of pressure-driven modes (such as ballooning modes in toroidal devices). Amplitude of the interaction between a magnetic field associated with the perturbation and the equilibrium current gradient might potentially give rise to current-driven kink instabilities. Other types of instabilities, such as the Rayleigh-Taylor instability (driven by gravitational-stratification) or Kelvin-Helmholtz instability (driven by fluid velocity shear) can be driven unstable. Furthermore, another class of instabilities (the so called tearing modes, introduced in Sec. 2.3.2, forming the magnetic islands in tokamaks) is introduced in case of a resistive MHD. In the following sections, destabilization of kinks and magnetic islands (the most dangerous modes in the context of disruption onset) will be briefly discussed.

For the purpose of further discussion, it is useful to introduce the so called plasma β, defined as a ratio of kinetic to magnetic pressure,

$$\beta = \frac{\text{kinetic pressure}}{\text{magnetic pressure}} = \frac{p}{B^2/2\mu_0}. \tag{2.20}$$

Small β ($\beta \ll 1$) indicates that magnetic dominates the thermal pressure, a situation typical of fusion reactors.

2.3.1 Destabilization of ideal kinks

As was stated above, interaction between the equilibrium current gradient and the perturbed magnetic field might potentially give rise to current-driven kinks. For large aspect ratio and negligible plasma β tokamak, it is shown in Ref. [16] that the external kink is stabilized when $m/n < q_\mathrm{a}$ (q_a being the safety factor at $r = a$), i.e. the resonant surface is located in the plasma. When $m/n > q_\mathrm{a}$, i.e. the mode resonant surface is outside of the plasma, the kink can become unstable. Application of the energy method (adjusted for the here examined case) with a toroidal current density profile of different peakiness (assured via variation of ν) prescribed by:

$$j(r) = j_0\left(1 - \left(\frac{r}{a}\right)^2\right)^\nu \tag{2.21}$$

lead to construction of a stability diagram in the $q_\mathrm{a}/q_0(q_\mathrm{a})$ space, with q_0 being the safety factor value at the magnetic axis. The q_a/q_0 term accounts for the current profile peaking via $q_\mathrm{a}/q_0 = \nu + 1$. It was shown that in case of current profiles with $\nu < 1$, the $j(r)$ is flat enough to destabilize kink modes of any structure. For current profiles of class $\nu > 1$, the profile peakiness assures instability stabilization, with an exception of cases where the external resonant surfaces approach closely the plasma boundary. There, the modes of lowest m are the most unstable ones and the experimental boundary in terms of stability to external kinks is setting the limiting edge safety factor to $q_\mathrm{a} \sim 2$. It is worth noting that experimentally, destabilization of external kinks can be observed when the plasma current ramp-up rate is too fast with respect to the current diffusion time. The current density does not thus have enough time to redistribute itself into a peaked, stable, profile and the conditions are favourable for destabilization of external kinks of the $m = q_\mathrm{a}$ [6].

In case of the non-negligible β the pressure gradient influences the kink stability. The β non-negligibility typically applies in the proximity of the resonance surfaces and results in destabilization of pressure driven modes of high n. Low n instabilities appear problematic for the so called tokamak advanced scenarios having a specially tailored safety factor profile [6] (typically elevated at the magnetic axis).

An overall limit of the plasma β for destabilization of number of ideal instabilities was retrieved in Ref. [37] by varying pressure and current profiles and resulted in the following relation (the so called Troyon β limit),

$$\beta_{\max} = \beta_{\mathrm{N}} \cdot \frac{I_{\mathrm{p}}}{aB_{\mathrm{t}}}[\%] \tag{2.22}$$

with the proportionality constant given by normalized beta β_{N}. Eq. (2.22) was confirmed using data from various tokamaks. The value of β_{N} is usually of the order unity and can be increased by modifying the plasma shape from non-circular to elongated plasmas and by increasing the current density profile peaking [6].

Finally, it is worth noting that the so called Kruskal-Shafranov limit states that the value of safety factor at any radial position must exceed 1 to avoid kink modes (from here the 'safety' label) [38, 39]. In practical applications, a limit on the minimum edge safety factor, $q_{\mathrm{a}} > 2$ is set, see above. The Kruskal-Shafranov limit is nevertheless encountered in the tokamak operation in the context of q_0 that must exceed 1 in order to avoid appearance of internal m/n = 1/1 kink modes.

2.3.2 Destabilization and growth of magnetic islands

In the previous section, destabilization of kink instability was discussed in terms of an ideally conducting plasma, neglecting the plasma resistivity. However, a resistive form of the kink instability, a tearing mode, can be driven unstable too. Experimental observations show that perturbations can lead to breaking up of the topology of nested flux surfaces and onset of tearing modes through the magnetic reconnection (recall Sec. 2.1.1). Typical time scales associated with the magnetic field lines diffusion are about $\tau_D \approx 1$ ms, suggesting that diffusive region is of a typical length of 10^{-2} m, which is of about two orders of difference in comparison of the usual plasma size. Resistive layers are typically located near the resonant surfaces and in the remaining plasma region, the ideal MHD can be applied.

Resistive destabilized modes adopt a form of magnetic islands. An example of an island located at $q = 3/2$ surface is given in Fig. 2.3b. In the figure, the so called O and X-points of the island are highlighted. The O-point refers to the island centre (and defines the point at which the radial extent of the island, its width w, is normally considered). The X-point is located at the intersection of the island separatrix and the resonant surface.

An island can extend over a substantial part of the plasma radius and reduce the plasma confinement. In particular, the island allows a fast (parallel to the field lines) transport of the heat and particle in the radial direction. The latter is in the island absence typically delimited by the relatively slow perpendicular diffusion timescale [40]. Equilibration of the temperature (and density) across the island typically results in the local plasma cooling.

Growth rates associated with the resistive modes are longer than those of ideal MHD. An analytical formula providing the island growth rate can be obtained by dividing plasma into the regions of ideal and resistive MHD validity and solving ideal MHD equation in the plasma bulk ('outer region') and resistive MHD in a thin layer of width δ at the resonant surface location. The solutions have to match at the interface continuously. It can be shown that in the outer region, the so called tearing mode equation,

$$\frac{1}{r}\frac{d}{dr}\left(r\frac{d\tilde{\psi}}{dr}\right) - \frac{m^2}{r^2}\tilde{\psi} - \frac{\mu_0}{B_\theta(1-q(r)n/m)}\frac{dj(r)}{dr}\tilde{\psi} = 0, \tag{2.23}$$

singular at $q(r) = m/n$, governs the spatial distribution of a perturbed helical flux function $\tilde{\psi}$, associated with the mode magnetic field [16]. Stability conditions can be in the scope of a linearised theory approached by examining first the limit of $\delta \to 0$ and $\tilde{\psi}$ vanishing at the wall, thus assuming a perfectly conducting wall at $r = r_\mathrm{w}$ (those conditions will be again discussed in Sec. 2.5.2). For a given current profile (prescribed, for example, by Eq. (2.21)), integration of Eq. (2.23) at the two outer regions and their continuous connection at $r = r_\mathrm{s}$ reveals a discontinuity of the $(d\tilde{\psi}/dr)\tilde{\psi}$ at the resonant surface [6]. The discontinuity determines the so called stability index $\Delta' = [(d\tilde{\psi}/dr)/\tilde{\psi}]_{r_\mathrm{s}^-}^{r_\mathrm{s}^+}$. Sign of the discontinuity then determines the system stability. In particular, it is unstable if $\Delta' > 0$ and the index magnitude can be interpreted as a free energy source driving the instability growth. The stability index is thus a function of the equilibrium current density profile, the position of the rational surface (imparted from the mode structure) and the boundary conditions, such as proximity of the mode location to the conducting shell. Ref. [6] further reports on an increasing system stability for increasing m.

Out of the $\delta \to 0$ limit, the ideal and resistive MHD solutions have to match at the edge of the tearing mode (adopting a magnetic island form). Details of the derivation can be found for example in [6, 25]. Here, it is reported that the so called constant psi approximation, that assumes the perturbation flux function $\tilde{\psi}$ being constant within the island extent, allows the island width parametrization using the strength of the magnetic perturbation,

$$w = 4\sqrt{\frac{q|\tilde{\psi}|}{q'B_\theta}}_{r=r_\mathrm{s}}. \tag{2.24}$$

Maxwell's equations combined with the Ohm's law (incorporating the resistivity, η, within the island region) and the relation $w^2 \propto |\tilde{\psi}|$, arising from Eq. (2.24), yield the following expression for the island width evolution:

$$\frac{dw}{dt} \cong \frac{\eta}{\mu_0}\Delta'. \tag{2.25}$$

The island growth rate is positive when $\Delta' > 0$. Eq. (2.25) can be reformulated in terms of the resistive diffusion time (Eq. (2.13)) $\tau_\mathrm{R} = (\mu_0/\eta)r_\mathrm{s}^2$ to the form of the so called Rutherford equation [41],

$$\frac{dw}{dt} \cong \frac{r_\mathrm{s}^2}{\tau_\mathrm{R}}\Delta', \tag{2.26}$$

that can be in turn presented in the context of the plasma temperature using the expression for the Spitzer resistivity [42] scaling as $\eta \propto T_e^{-3/2}$, yielding

$$\frac{dw}{dt} \propto \frac{\Delta'}{\mu_0 T_e^{3/2}}. \tag{2.27}$$

Stability diagrams in the $q_a/q_0(q_a)$ space were examined for the case of the tearing modes in number of references, for example in Refs. [16,43]. Imposing the Kruskal-Shafranov limit on the central safety factor, $q_0 \geq 1$, the latter reference reported on increase of the current gradient in between the $q = [1\ 2]$ surfaces, resulting in increasing Δ' with decreasing q_a. In Ref. [44], the stability index was examined for fixed $q_0 \sim 1$ and q_a by varying the current profile peaking, expressed via the plasma internal inductance l_i. A tearing mode unstable region in the $l_i(q_a)$ space has been identified. In Ref. [45] the l_i/q_{95} ratio (q_{95} substitutes q_a in elongated plasmas and it is defined as the safety factor at the flux surface enclosing 95% of the toroidal flux) has been used as a parameter discriminating disruptive and non-disruptive plasmas. There, the ratio has been interpreted as a proxy for Δ', i.e. the free energy driving the mode growth.

The discussion above concerned the so called classically (un)stable tearing modes. A new tearing mode class, classically stable, can be destabilized under hereby described favourable conditions. Due to the $\sim 1/R$ dependence of the equilibrium toroidal field a particle trapping phenomenon occurs in the tokamak. Collisions between passing and trapped particles give rise to a spontaneous bootstrap current [46]. The so called neoclassical tearing modes (NTMs) are destabilized within helical 'holes' in the bootstrap current [47,48]. Those holes are typically caused by local pressure profile flattening caused by a seeding island. The NTMs are, just as the classical tearing modes, preferentially driven unstable at low mode structures. It can be shown that for small seeding islands, the NTM growth is suppressed. The NTM destabilization thus requires a seeding MHD mode of a certain critical extent. Furthermore, it can be shown that NTMs are growing under favourable (high) plasma pressure conditions. Destabilization of neoclassical tearing modes thus represents a practical limitation of the plasma performance as they are normally seeded at high plasma beta, competing thus with the rather rarely experimentally observed ideal MHD Troyon β limit, discussed in Sec. 2.3.1.

2.4 Phenomenological disruption description

Following the ideal/resistive mode destabilization (under favourable plasma conditions), its growth can lead to the plasma confinement loss, the disruption. Phenomenological description of this event typically consists of multiple phases, recognisable in the distinct plasma parameter evolutions. An example of a mode destabilization and growth is shown in Fig. 2.4, left. At a certain point, a plasma thermal quench, i.e. a sudden (on millisecond time scale) drop in the plasma temperature takes place (see Fig. 2.4, right, first panel, the thermal quench is initiated at $t = t_{TQ}$). The sudden decrease in the thermal energy content is explained on the basis of a magnetic field line stochastization following a multiple island overlap, illustrated in Fig. 2.5. Owing probably to the subsequent current profile flattening (recognisable as a decrease in l_i in Fig. 2.4, the second panel)

a transient negative spike in the loop voltage V_{loop} (i.e. the voltage created in a loop concentric with the plasma column, resulting from the poloidal magnetic flux variation) follows and given the flux conservation, a transient positive spike in the plasma current is observable. Fall in the plasma temperature increases its resistivity. The externally induced voltage is usually not able to sustain the plasma current under such conditions and the plasma current decays to zero during the so called current quench phase. The *disruption time*, t_{disr}, is set hereby at the onset of a current spike of the largest amplitude that precedes the current quench. It is at this moment when the plasma usually gets vertically destabilized.

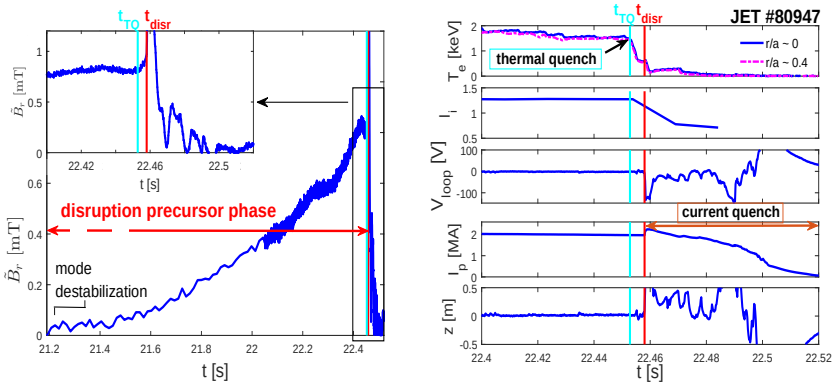

(a) (b)

Figure 2.4: *Example of a tokamak discharge terminated by a disruption. (a) After destabilization, the mode grows and disrupts the plasma. The mode radial field component $\tilde{B}_r$ is displayed, calculation details are given in Sec. 3.1.1. (b) The thermal quench, recognizable as a sudden drop of T_{e}, takes place at $t = t_{\mathrm{TQ}}$. The drop in l_{i} follows, together with the negative transient loop voltage and positive plasma current spikes (onset at $t = t_{\mathrm{disr}}$) and the vertical plasma destabilization. In the last phase of the disruption, the current quenches.*

The above presented sequence of events accompanies the *major disruption*. During a *minor disruption*, te thermal quench is observed too, but the plasma confinement is not completely lost. In fact, the plasma temperature is often observed to recover its pre-minor disruptive value [49].

In the disruption description presented above the vertical destabilization has not been the primary cause of the disruption onset. It is worth noting, however, that elongated plasmas are prone to the so called vertical displacement events (VDE), where the vertical destabilization is the primary disruption cause. Those events are particularly dangerous since the plasma can carry substantial portion of the plasma current when it impacts the wall. The subsequent closed plasma-vessel current loop can result in substantial forces applied on the vessel structural components. Prevention of the VDEs relies on vertical position feedback control [50].

Based on empirical observations, tokamak operation diagrams often include stability boundaries dependent on the plasma density. An example of such stability diagram, a variant of the so called Hugill diagram [51], is shown in Fig. 2.6a,

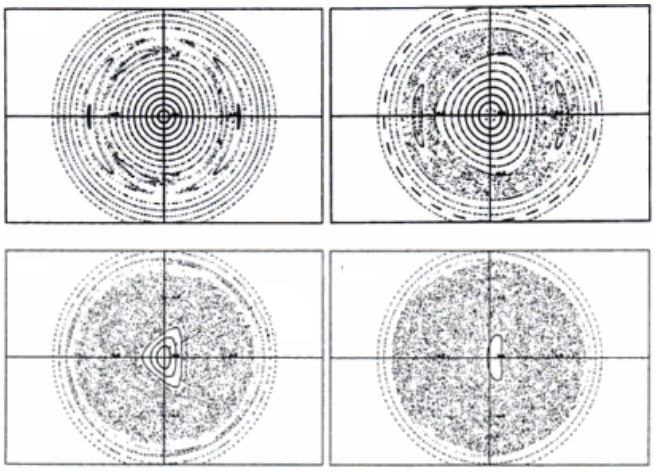

Figure 2.5: *Illustration of magnetic field line stochastization leading to the plasma confinement loss [34].*

where the stable and unstable regions are separated in the $q_{\mathrm{a}}(\bar{n}_{\mathrm{e}}R/B_{\phi})$ space [52] with $\bar{n}_{\mathrm{e}}$ being an average plasma density.

The density limit physics origin has not been fully understood since linking the mode destabilization with the increase in plasma density is not straightforward. It is assumed that the modes are current-driven, and that the current profile varies as the temperature decreases, the latter being a consequence of the density increase and the fact that pressure is constant on flux surfaces. It is thought that the density limit is linked to the plasma conditions at the plasma edge. This is supported by the fact that the empirical Greenwald density limit, formulated in terms of the maximum line averaged density, the Greenwald density n_{GW} [53],

$$n_{\mathrm{GW}} = \frac{I_{\mathrm{p}}}{\pi a^2}, \tag{2.28}$$

is mainly sensitive to the density at the plasma edge, i.e. the core region can have densities $n > n_{\mathrm{GW}}$. Onset of the density limit is closely bound with the development of toroidally symmetric MARFE (multi-faceted axisymmetric radiation from the edge) via particle (fuel and impurity) recycling from the wall. MARFE is a region of cold, dense and highly radiating plasma, typically located at the torus high field side close to the so called X-point (point of null B_{θ} located at the separatrix) of the plasma adopting a diverted configuration. The latter is favourable for a controlled power and particle exhaust within the so called divertor usually formed at the bottom of the confining vessel (see Fig. 2.6b). A poloidal MARFE destabilization has been reported as a possible cause of the current profile modification leading to the onset of a tearing mode [54].

Impurities play an important role in the disruptive process not only trough the MARFE formation. In general, impurity sources are various, e.g. particles can be eroded from the wall and plasma facing component materials during transient events; impurity particles can be intentionally puffed to plasma in dedicated experimental campaigns etc. Impurities act as energy sinks through the radiation. The radiated power density for a given ion specie is proportional to the

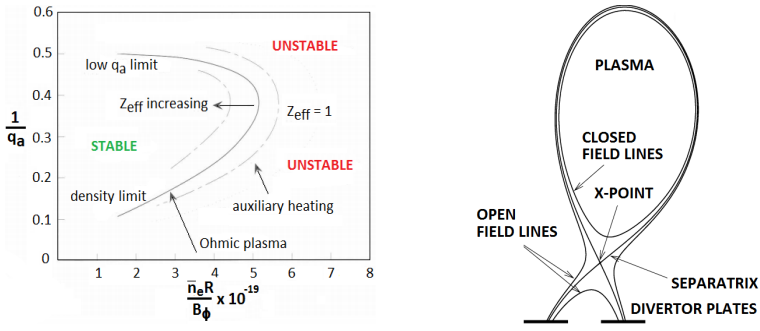

(a) (b)

Figure 2.6: *(a) Variant of a Hugill diagram delimiting the stable tokamak operation regime in the $q_a(\bar{n}_e R/B_\phi)$ plane [16]. (b) Illustration of a diverted plasma configuration [55].*

radiation parameter R_p, which is temperature dependent [16] (see Fig. 2.7). The plasma contamination by impurities can be expressed upon its effective charge, Z_{eff}, calculated as

$$Z_{eff} = \frac{\sum_i Z_i^2 n_i}{n_e} \tag{2.29}$$

where Z_i is the charge state of the ion species and n_i the ion density. Larger Z_{eff} can support radiative losses and move the stable boundary in terms of the density limit towards lower densities. The boundary can be moved back to stable higher densities by application of the auxiliary heating (see Fig. 2.6a). If, for any reason, the external heating is switched off during the discharge, the stability boundaries can move and the plasma can pass, at the given density and impurity content, to the region favourable for the density limit disruption onset. It is worth noting that l_i typically progressively increases when the density limit is approached, owing probably to the edge plasma cooling. This usually results in a steepening of the current profile. The l_i/q_{95} ratio, proxy for the mode growth energy source, can thus increase towards the disruption, unless the q_{95} is modified externally and/or l_i relaxes (temporarily) through a minor disruption.

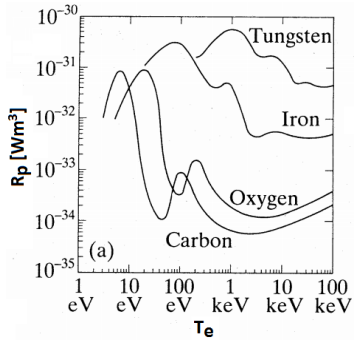

Figure 2.7: *Radiation parameter R_p shown as a function of the electron temperature T_e [16].*

In Ref. [56], an influence of the wall material on the current quench rate has been discussed. It was shown that passage from the carbon first wall material to tungsten resulted in extension of the current quench phase. The usual low temperatures accompanying the current quench can be in favour of significant carbon radiation, speeding up the energy losses when this impurity is abundant, such as when it constitutes the first wall components. Another important consequence of the passage to the tungsten first wall material configuration was the observed influx of this element to the plasma core [57]. High temperatures within this region are favourable for significant tungsten radiation (see Fig. 2.7) and hollow temperature profiles were reported. Consequently, the current density profile can become hollow, which can lead to an elevated safety factor profile (of a sombrero shape) in the plasma core region (see Fig. 2.8). Such q-profile might result in appearance of double tearing modes, i.e. modes of the same m/n structure but different minor radii.

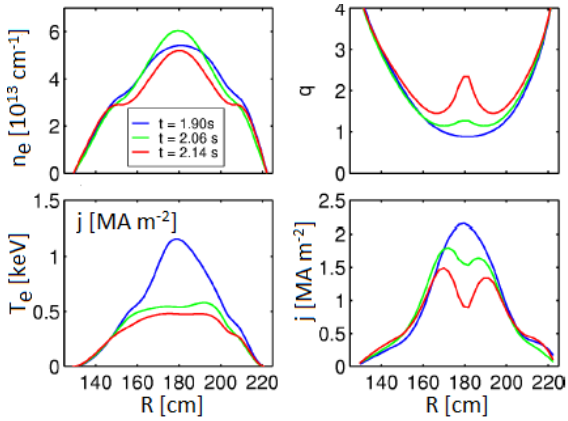

Figure 2.8: *Illustration of the in-core tungsten impurity influx effect on the density and temperature profiles. Eventually, the current density profile becomes hollow and the central elevated safety factor profile favours onset of double tearing modes [58].*

Finally, a sudden fall of a macroscopic object in the plasma can induce the disruption via significant radiative losses (modifying the current profile), accompanying the object travel through the plasma. Example of such an event, captured by in-vessel viewing fast sampling camera, is shown in Fig. 2.9.

2.5 Rotation and locking of MHD modes

Modes are observed to either rotate or to be static in laboratory frame when destabilized. Locking of initially rotating tearing modes to the wall is frequently observed in tokamaks. Given the disruptive potential of the braking modes, a considerable effort has been invested in the description of this phenomenon in the past. The mode rotation, constituting the necessary prerequisite for the onset of locking, is closely bound with the plasma rotation driven by extrinsic and

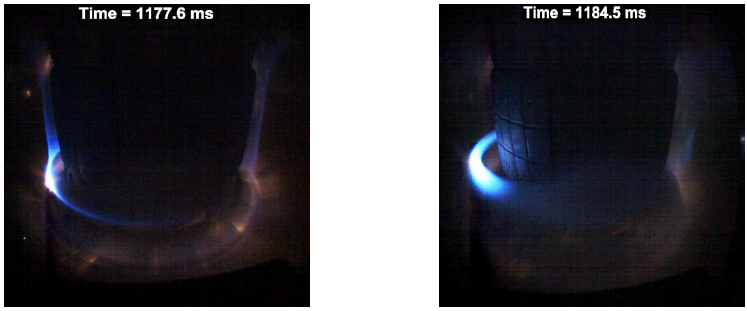

Figure 2.9: *Macroscopic piece of material inducing disruption, captured by fast sampling camera viewing the COMPASS tokamak vessel interior.*

intrinsic sources. Origins of the latter are not fully understood, despite extensive theoretical and experimental research. The *born-locked modes* can of course disrupt the plasma too and description of conditions favourable for their onset has been presented in number of references. Rotation, locking and appearance of born-locked MHD modes disrupting the plasma constitute integral phenomena studied in this work and in the following sections contextually relevant terms associated with those phenomena will be presented. Basic introduction to the tearing mode rotation is given in Sec. 2.5.1. The model for mode braking, particularly important in Chap. 5, yielding an estimate of the braking duration and critical mode width for locking, is presented in Sec. 2.5.3. This section exploits features of the perturbation field associated with a rotating mode located in vicinity of resistive wall, discussed in Sec. 2.5.2. Finally, the locked mode characteristics, together with discussion concerning excitation of born-locked modes, are contained in Sec. 2.5.4.

2.5.1 Tearing mode rotation

The mode movement is bound with the plasma rotation that can be driven by intrinsic and extrinsic sources.

The main extrinsic rotation source is due to the application of neutral beam injection, resulting in torque T_{NBI}, supplied to the plasma via ionization and collisions of the neutral particles (moving mainly in the toroidal direction) with the plasma particles. The transferred momentum is a function of the energy and amount of neutrals and the beam-plasma angle [59].

Intrinsic rotation sources, appearing to be of different origins in the core and plasma edge regions [60, 61], are not fully understood. Because of the higher ion mass, the plasma bulk velocity v_ϕ is mainly associated with the toroidal ion velocity v_{i} (motion in the poloidal direction is assumed damped [62]). Theoretical description of v_{i} requires two fluid plasma model, not embedded in MHD and approaches the velocity as a sum of the $\mathbf{E}\times\mathbf{B}$ and ion diamagnetic $\mathbf{v}_{\mathrm{i,dia}}$ drifts [63], the latter arising from a gyration of a particle in the presence of a pressure gradient,

$$\mathbf{v}_{\mathrm{i,dia}} = \frac{\nabla p_{\mathrm{i}} \times \mathbf{B}}{n_{\mathrm{i}} e B^2}. \tag{2.30}$$

The following empirical dimensionless scaling for spontaneous v_ϕ was derived in

Ref. [64]:

$$v_\phi = C\beta_\mathrm{N}\rho^* / v_\mathrm{A}, \tag{2.31}$$

with $C \approx 1$ and ρ^* being the normalized Larmor radius $\rho^* = r_{\mathrm{L,i}}/a$, presenting thus the velocity in the context of the characteristic plasma length scale.

The mode rotation is assumed to be a sum of the ion bulk velocity and the electron diamagnetic drift (i $\rightarrow$ e in (2.30)),

$$v_\mathrm{MHD} = v_\phi + v_\mathrm{e,dia}, \tag{2.32}$$

(given that within the two fluid model, the magnetic field is frozen in the electron fluid [6]) with $v_\mathrm{e,dia}$ being perpendicular to the field lines. Eq. (2.32) holds for small islands, where the temperature and density might not be flattened [25], i.e. the pressure gradient can be significant. In case of large islands, the gradient vanishes and the mode moves with the plasma bulk (the mode does not 'slip' through it). The expression for the mode frequency ω_MHD reflects its helical structure (expressed via the ratio of the poloidal to toroidal mode numbers, m/n),

$$\omega_\mathrm{MHD} = 2\pi f_\mathrm{MHD} = n\omega_\phi - m\omega_\theta, \tag{2.33}$$

and using the conversion between the angular frequency and velocity, one obtains [27]:

$$\omega_\mathrm{MHD} = n\left(\frac{v_\phi + v_{\mathrm{e,dia},\phi}}{R}\right) - m\frac{v_{\mathrm{e,dia},\theta}}{r}. \tag{2.34}$$

The sign associated with the diamagnetic drift depends on the NBI module injection (setting the direction of plasma rotation) relative to the direction of the plasma current and differs thus for cases with co and counter-current NBI injection.

Large mode rotation can lead to its stabilization in the vicinity of a conducting structure (see Sec. 2.5.2). Maintaining/increasing the mode rotation rate has thus been in the focus of disruption avoidance schemes [65–68].

It should be noted that the momentum transfer from neutral beam modules becomes less effective for larger plasmas due to the larger inertia [69]. Furthermore, T_NBI scales as $\sim 1/\sqrt{E_\mathrm{NBI}}$, where E_NBI is the accelerated beam energy. To assure penetration of the heating beam to the plasma centre, E_NBI is estimated to ~ 1 MeV in ITER [70]. The beam induced torque will be thus decreased in ITER in comparison to current NBI designs in smaller devices, where the necessary beam energy is comparatively lower. Understanding of the intrinsic rotation sources and their enhancement is thus fundamental for the future large devices.

2.5.2 Rotating mode field in the vicinity of a resistive wall

In accordance with a typical experimental situation, rotating modes are located in the vicinity of a resistive wall in tokamaks. Rotating modes induce mirror currents in the wall structure (decaying at the wall characteristic temporal constant), those in return affect the perturbed helical magnetic field $\tilde{\mathbf{B}}$ associated with the mode. In particular, mode can become stabilized when rotating fast relative to inverse of the wall temporal constant. Wall resistivity also becomes important in the derivation of force causing the mode braking. In the following section, basic

properties of $\tilde{\mathbf{B}}$ in the vicinity of a resistive wall will be examined. First, the no-wall form of $\tilde{\mathbf{B}}$ will be derived for reference and further application in Chap. 5.

Properties of the mode field $\tilde{\mathbf{B}}$ can be derived by examining the scalar flux function, introduced in Sec. 2.3.2, of form $\tilde{\psi}(r,\theta,\phi) = \tilde{\psi}(r)e^{i(m\theta - n\phi - \omega t)}$. Radial and poloidal components of $\tilde{\mathbf{B}}$ are retrieved via

$$\tilde{B_{\mathrm{r}}} = -\frac{1}{r}\frac{\partial\tilde{\psi}}{\partial\theta} = -\frac{im}{r}\tilde{\psi}, \tag{2.35}$$

$$\tilde{B_{\theta}} = \frac{\partial\tilde{\psi}}{\partial r}. \tag{2.36}$$

Mode located at $r = r_{\mathrm{s}}$ is a source of a surface current $\tilde{J}_{\mathrm{s}}(r,\theta,\phi) = J_{\mathrm{s}}^{\dagger}\delta(r - r_{\mathrm{s}})e^{i(m\theta - n\phi - \omega t)}$ with $J_{\mathrm{s}}^{\dagger} = \mathrm{cte}$. Analogically, current induced in the wall due to the perturbation field is defined in the form $\tilde{J}_{\mathrm{w}}(r,\theta,\phi) = J_{\mathrm{w}}^{\dagger}\delta(r - r_{\mathrm{w}})e^{i(m\theta - n\phi - \omega t)}$ with r_{w} the wall minor radius. In the 'thin wall' approximation, the current is assumed to be constant over the wall thickness b. Those definitions will be used to retrieve analytical expression for the flux function in the absence or presence of a conductive medium in the vicinity of the mode. The mode properties in terms of its growth rate γ and rotation rate ω_{MHD} are included in term ω,

$$\omega = i\gamma + \omega_{\mathrm{MHD}}. \tag{2.37}$$

The following discussion applies to the case of a cylindrical screw pinch, the 'straight tokamak' configuration, with ignorable variation of solution along the cylinder axis passing through its bases, unless specified differently, and it is assumed that a concentric cylindrical conducting shell ('wall') is surrounding the cylindrical plasma.

Vacuum solution

In the absence of a conductive structure, magnetostatic equations apply and Laplace's equation, governing the properties of the flux function, becomes:

$$\frac{1}{r}\frac{d}{dr}\left(r\frac{d\tilde{\psi}}{dr}\right) + \frac{1}{r^2}\frac{d^2\tilde{\psi}}{d\theta^2} = \frac{1}{r}\frac{d}{dr}\left(r\frac{d\tilde{\psi}}{dr}\right) - \frac{m^2}{r^2}\tilde{\psi} = 0. \tag{2.38}$$

In linear configuration, Eq. (2.38) has a solution of the flux function of a form:

$$\tilde{\psi} = (\alpha r^m + \beta r^{-m})e^{im\theta}. \tag{2.39}$$

where α and β are coefficients to be determined. Solution domain can be separated in two regions, $\tilde{\psi}_{\mathrm{I}} = \tilde{\psi}(r < r_{\mathrm{s}})$ and $\tilde{\psi}_{\mathrm{II}} = \tilde{\psi}(r > r_{\mathrm{s}})$, with the respective constants $\{\alpha,\beta\}_{\mathrm{I/II}}$. The latter are retrieved upon accounting for the boundary conditions of the presented problem. At $r = r_{\mathrm{s}}$, $\psi_{\mathrm{I}} = \psi_{\mathrm{II}}$, imposing the continuity of the solution along the radial coordinate. Interface condition for the tangential component of the magnetic field applies:

$$\mathbf{n} \times (\mathbf{B_I} - \mathbf{B_{II}}) = \mu_0\tilde{\mathbf{J}}_{\mathbf{s}}, \tag{2.40}$$

with $\mathbf{n}$ being a vector normal to the interface. Finally, ψ_{I} and ψ_{II} are imposed to be finite in the respective limits $r \to 0$ and $r \to \infty$, yielding $\alpha_{\mathrm{II}} = \beta_{\mathrm{I}} = 0$.

Analytical form of the flux function becomes:

$$\tilde{\psi}_{\mathrm{I}} = \frac{\psi^{\dagger}}{m}\left(\frac{r}{r_{\mathrm{s}}}\right)^{m} e^{im\theta}, \tag{2.41}$$

$$\tilde{\psi}_{\mathrm{II}} = \frac{\psi^{\dagger}}{m}\left(\frac{r_{\mathrm{s}}}{r}\right)^{m} e^{im\theta}, \tag{2.42}$$

where $\psi^{\dagger} = \mu_0 J_{\mathrm{s}}^{\dagger} r_{\mathrm{s}}/2$. Calculation of the respective $\tilde{\mathbf{B}}$ components using the Eqs.(2.35)-(2.36) for the two solution domains given by Eqs.(2.41)-(2.42) serves for evaluation of the relation between the two filed components. The respective relations are:

$$\tilde{B}_{\mathrm{r,I}} = -i\tilde{B}_{\theta,\mathrm{I}}, \tag{2.43}$$

$$\tilde{B}_{\mathrm{r,II}} = i\tilde{B}_{\theta,\mathrm{II}}, \tag{2.44}$$

i.e. the components are shifted in the complex plane, but the absolute values are equal in both cases.

Bending the plasma column in an axisymmetric configuration implies correction of the flux function solutions (Eqs. (2.41)–(2.42)) for the effect of toroidicity, both along the radial and poloidal coordinates. Higher order effects can be included by correcting for plasma non-circular cross-section, i.e. for its elongation and triangularity (this treatment is not considered here).

Usage of Ampére's law revealed a $B_{\phi} \propto 1/R$ dependence of the equilibrium toroidal field on the R coordinate (see Sec. 2.2). Unlike was the case of the 'straight tokamak', this dependency means that B_{ϕ} is no longer constant on a given flux surface. Bending of the plasma column into a torus implies that the poloidal field created by the plasma current will be of different intensity at the inner and outer part of the torus, in particular, weaker at the torus low-field side than at the high-field side. Together with other forces, this would lead into unbending of the torus back to the cylinder. It is by adding an extra vertical magnetic field that the radial forces balance, however, the intensity of B_{θ} remains asymmetrical, stronger at the low-field side, and proportional to the toroidicity restoring force comprising local pressure β_p,

$$\frac{1}{\beta} = \frac{1}{\beta_p} + \frac{1}{\beta_t}, \tag{2.45}$$

(subscripts 'p' and 't' refer to poloidal and toroidal, respectively) and the scalar current peaking expressed by l_i. Both field components are thus not constant on the flux surfaces, resulting in that the inclination of a magnetic field line of a $\{m, n\}$ helicity is not constant. Via the Merezhkin correction, transformation from the toroidal to 'straight' geometry is possible via defining the straight field line angle θ^*,

$$\theta^* = \theta - \frac{r_{m,n}}{R_{m,n}}\left(\hat{\beta}_p(r_{m,n}) + \frac{\hat{l}_i(r_{m,n})}{2} + 1\right)\sin(\theta) = \theta - \lambda(r_{m,n})\sin(\theta). \tag{2.46}$$

with '$\hat{}$' denoting averaging over poloidal cross-section enclosed by radius $r_{m,n}$. Parameter λ is maximised when $r \to a$. Variation of the phase of the vacuum

solution of the flux function without and with the effect of toroidicity included ($\lambda = 0$ and $\lambda > 0$, respectively) is shown in Fig.2.10a. Notable asymmetry in the phase along the poloidal coordinate is observed in the latter case and faster oscillations are observed at the inner part of the torus, $r < 0$ and $\theta \to \pi$. This modulation can be crucial for example in the analysis of the data from the poloidally displaced magnetic sensors aiming at determining the mode number m. Furthermore, passing from a cylindrical to toroidal configuration leads to the coupling of modes of the same n but different m mode number. This coupling results in interference and destabilization of kinks of different m (the same n number), limiting the achievable plasma β, particularly in the advanced scenario plasmas [6]. In Ref. [27], it was shown that the amplitude modulation $\tilde{A}(\theta, \phi)$ in an axisymmetric tokamak of circular cross-section is the following:

$$\tilde{A}(\theta,\phi) = \tilde{A}\cos(m\theta - n\phi) + \frac{\tilde{A}_1}{2}\Big\{\cos[(m-1)\theta - n\phi - \varphi_1] + \cos[(m+1)\theta - n\phi + \varphi_1]\Big\}. \tag{2.47}$$

In this expression, $\tilde{A}$ is the amplitude of the perturbation at a given point along the radial coordinate. The first term on the right-hand side represents the phase of the flux function related to the cylindrical geometry. The second term appears after modulation of the amplitude when passing to the case of generalized geometry, retrieved upon Fourier series expansion of the amplitude in the poloidal θ coordinate. The effect of toroidicity is pronounced for $j = 1$ and the $\Delta m = \pm 1$ sidebands justify the existence of the toroidally coupled modes. The same conclusion can be obtained by accounting for the Merezhkin correction (see above), expressing the phase in terms of a Bessel function of the first kind $J(\pm 1, m\lambda)$ [6]. This approach allows estimating the amplitude $\tilde{A}_1$ (under the condition $m\lambda \ll 1$),

$$\tilde{A}_1 = \tilde{A} m\lambda \approx \tilde{A}\frac{r}{R}, \tag{2.48}$$

The effect of toroidicity on the radially-dependent part of the flux function solution can be examined by combining Eq. (2.42) and Eq. (2.48), yielding exact solutions of the sideband flux functions for $r > r_{\mathrm{s},m+1}$:

$$\tilde{\psi}(r) = \frac{\psi^\dagger}{m+1}\left(\frac{r_{\mathrm{s},m}}{r}\right)^{m+1}\cos[(m+1)\theta]J(+1, m\lambda)\left(\frac{R_0}{r\cos\theta + R_0}\right), \tag{2.49}$$

$$\tilde{\psi}(r) = \frac{\psi^\dagger}{m-1}\left(\frac{r_{\mathrm{s},m}}{r}\right)^{m-1}\cos[(m-1)\theta]J(-1, m\lambda)\left(\frac{R_0}{r\cos\theta + R_0}\right). \tag{2.50}$$

The last term in Eq. (2.49) and Eq. (2.50) results from the $1/R$-dependence of the helical field in toroidal geometry, which for large aspect ratio expands to $1/(r\cos\theta + R_0)$. The R_0 term in the nominator is added for normalization purposes. The perturbation field components in toroidal geometry are the following:

$$\tilde{B}_{r,\mathrm{tor}} = -\frac{1}{2\pi R}\frac{1}{r}\frac{\partial\tilde{\psi}}{\partial\theta}, \tag{2.51}$$

$$\tilde{B}_{\theta,\mathrm{tor}} = \frac{1}{2\pi R}\frac{\partial\tilde{\psi}}{\partial R}. \tag{2.52}$$

For given λ, the full solution including the effect of toroidicity is obtained by adding the sidebands to the cylindrical case. In Fig. 2.10b, the radial decay of $\tilde{B}_{\theta,\mathrm{tor}}$ for the case of the midplane low-field side ($\theta = 0$) is plotted for progressively

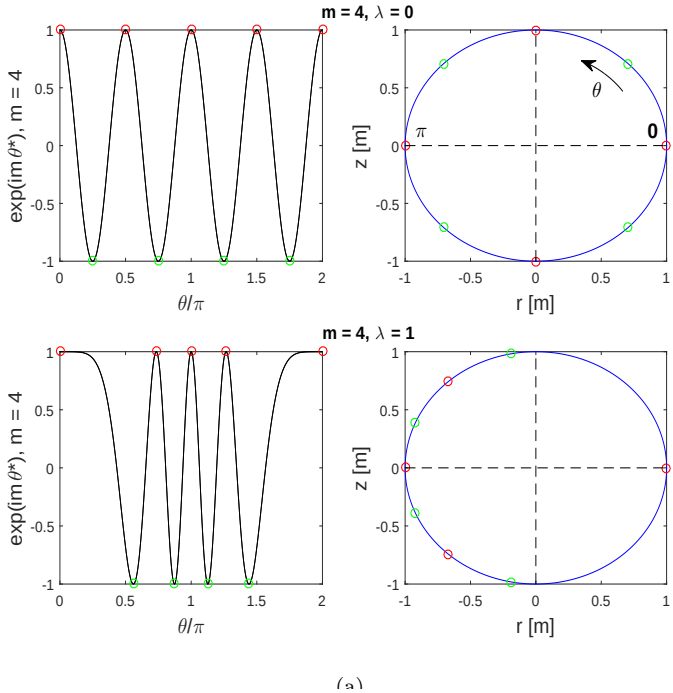

(a)

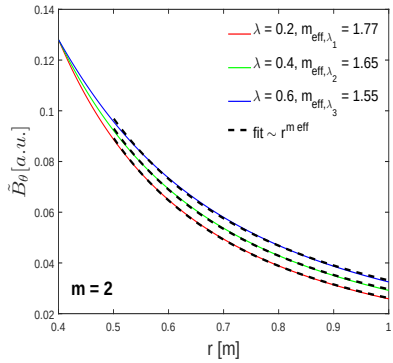

(b)

Figure 2.10: *(a) Effect of toroidicity on the flux function phase variation along the poloidal coordinate ($a = 1$ m, geometrical centre of the plasma cross-section is located at the $\{r, z\}$ axis origin). Note that the phase variation extrema (encircled in red and green) are densely spaced as $\theta \to \pi$ for $\lambda > 0$. (b) Radial decay of the poloidal component of the perturbation field, showing the effect of the toroidicity for various λ.*

increasing λ, $m = 2$. The typical ASDEX Upgrade values $R_0 = 1.65$ and $r_s = 0.4$ m (see Chap. 5) where adopted in the plot. The curves were fitted with an analytical function of the form $\alpha r^{m_{\text{eff}}}$ in the range $r = 0.5$ m to 1 m (the range is highlighted by the dashed lines). The fit parameter m_{eff} for the respective fits is displayed in the legend. Next, the m number was varied from 2 to 4, keeping fixed $\lambda = 0.4$ (adopting $\beta_p = 0.35$ $l_i = 1.4$ and the above mentioned geometrical values). The fitting procedure described above was applied for each m, retrieving the m_{eff} for every fit. The resulting relations $m = f(m_{\text{eff}})$ can be used in the expression for the mode poloidal field component, replacing m with its effective equivalent m_{eff}. For the high and low-field side cases, respectively, one obtains:

$$m_{\text{eff},\theta,\text{HFS}} = 2.57\, m - 1.30, \tag{2.53}$$

$$m_{\text{eff},\theta,\text{LFS}} = 0.81\, m + 0.03. \tag{2.54}$$

In case of the vacuum solution, the radial component of the perturbation field vanishes at the low and high-field side midplane. Given the symmetry of the problem, $\tilde{B}_{r,\text{tor}}(\theta = \pi/2) = \tilde{B}_{r,\text{tor}}(\theta = 3\pi/2)$, the resulting scaling relation for the effective mode numbers is:

$$m_{\text{eff,r}} = 0.98\, m + 0.86. \tag{2.55}$$

Resistive wall located in the mode vicinity

A conducting material placed at minor radius r_w, $r_w > r_s$, modifies the problem definition and adds a third region of solution of interest for the flux function, $\tilde{\psi}_{\text{III}} = \tilde{\psi}(r > r_w)$. In case of an ideal conductor the perturbation magnetic field is shielded instantaneously, i.e. $\tilde{\mathbf{B}}_{\text{III}} = 0$ and the interface conditions for the field radial component imply that $\tilde{B}_r = 0$ at the wall. It can be shown that the radial component of the perturbation field in the domain $r_s < r < r_w$ is reduced w.r.t. the vacuum solution, resulting in the mode stabilization.

Conductive wall of finite resistivity η_w placed in the mode proximity leads to further modification of the problem formulation. Unlike is the case of an ideal conductor, in which the current flows without a built-up of an electric field in the material, currents in the resistive wall decay on the time scale characterized by the wall resistive temporal constant τ_w and induce electric field $E_{w,\phi}$ (along the helical coordinate).

Under certain conditions, perturbation field can penetrate through the wall and a finite flux function $\tilde{\psi}_{\text{III}}(r > r_w)$ can be constructed. Then, it is of interest to retrieve analytical form of the flux function in the three regions of interest, again of the form given by Eq. (2.39) and with three pairs of coefficients $\{\alpha, \beta\}_{\text{I–III}}$. Continuity of the solutions along the interfaces r_s, r_w must be assured. Jump of the tangential component of the perturbation field is imposed by Eq. (2.40), using the appropriate surface currents $\tilde{J}_s$ and $\tilde{J}_w$. The latter is posed to be constant over the wall layer, i.e. $\tilde{J}_w = j_w b$. Following the requirement of finite $\tilde{\psi}_{\text{I,III}}$ at $r \to 0$ and $r \to \infty$, $\alpha_{\text{III}} = \beta_{\text{I}} = 0$. Radial component of the Faraday's equation is the following:

$$\frac{1}{r}\frac{\partial E_{w,\phi}}{\partial \theta} = -\frac{\partial B_r}{\partial t} = \frac{im}{r}\frac{\partial \psi}{\partial t} = \frac{m\omega}{r}\psi. \tag{2.56}$$

Using the Ohm's relation $\tilde{J}_w = E_{w,\phi}/\eta_w$, one obtains

$$\tilde{J}_w = \frac{\omega}{i\eta_w}\psi. \tag{2.57}$$

Coefficient α_{II} can be then expressed as

$$\alpha_{\mathrm{II}} = \frac{\mu_0 j_{\mathrm{w}} b r_{\mathrm{w}}}{m r_{\mathrm{w}}^m} = \frac{\mu_0 b r_{\mathrm{w}} \omega}{i m r_{\mathrm{w}}^m \eta_{\mathrm{w}}} \psi = -\frac{i\omega\tau_{\mathrm{w}}}{m r_{\mathrm{w}}^m} \psi, \tag{2.58}$$

where

$$\tau_{\mathrm{w}} = \frac{\mu_0 b r_{\mathrm{w}}}{2\eta_{\mathrm{w}}}. \tag{2.59}$$

In the limit of $\omega\tau_w/m \to 0$ the solution of vacuum flux function (Eq.(2.42)) at $r = r_{\mathrm{w}}$ can be inserted in Eq. (2.58). In this limit, $-i\omega\tau_w/m$ is the first term of the series expansion of $\omega\tau_{\mathrm{w}}/(i+\omega\tau_{\mathrm{w}})$. Final algebraic manipulation yields the full solution of the flux function in the three radial coordinate domains:

$$\tilde{\psi}_{\mathrm{I}} = \frac{\psi^\dagger}{m}\left[1 - \frac{\omega\tau_{\mathrm{w}}}{mi + \omega\tau_{\mathrm{w}}}\left(\frac{r_{\mathrm{s}}}{r_{\mathrm{w}}}\right)^{2m}\right]\left(\frac{r}{r_{\mathrm{s}}}\right)^m e^{i(m\theta-\omega t)}, \tag{2.60}$$

$$\tilde{\psi}_{\mathrm{II}} = \frac{\psi^\dagger}{m}\left[\left(\frac{r_{\mathrm{s}}}{r}\right)^m - \frac{\omega\tau_{\mathrm{w}}}{mi + \omega\tau_{\mathrm{w}}}\left(\frac{r_{\mathrm{s}}}{r_{\mathrm{w}}}\right)^{2m}\left(\frac{r}{r_{\mathrm{s}}}\right)^m\right] e^{i(m\theta-\omega t)}, \tag{2.61}$$

$$\tilde{\psi}_{\mathrm{III}} = \frac{\psi^\dagger}{m}\left[1 - \frac{\omega\tau_{\mathrm{w}}}{mi + \omega\tau_{\mathrm{w}}}\right]\left(\frac{r_{\mathrm{s}}}{r}\right)^m e^{i(m\theta-\omega t)}. \tag{2.62}$$

Relations between the radial and poloidal components of the mode magnetic field are:

$$\tilde{B}_{\mathrm{r,I}} = -i\tilde{B}_{\theta,\mathrm{I}}, \tag{2.63}$$

$$\tilde{B}_{\mathrm{r,II}}/\tilde{B}_{\theta,\mathrm{II}} = i\frac{\frac{mi+\omega\tau_{\mathrm{w}}}{\omega\tau_{\mathrm{w}}} r_{\mathrm{w}}^{2m} - r^{2m}}{\frac{mi+\omega\tau_{\mathrm{w}}}{\omega\tau_{\mathrm{w}}} r_{\mathrm{w}}^{2m} + r^{2m}}, \tag{2.64}$$

$$\tilde{B}_{\mathrm{r,III}} = i\tilde{B}_{\theta,\mathrm{III}}. \tag{2.65}$$

In the limit of $\omega\tau_{\mathrm{w}} \gg m$ $\tilde{\psi}_{\mathrm{III}} = 0$ and Eqs. (2.60)-(2.61) simplify to the ideal wall solution. For $\omega\tau_{\mathrm{w}} \to 0$, the no-wall limit is retrieved as $\tilde{\psi}_{\mathrm{II}} = \tilde{\psi}_{\mathrm{III}}$ and Eqs. (2.60)-(2.61) turn to Eqs. (2.41)-(2.42). Similarly, Eqs. (2.63)-(2.65) recover their ideal or no-wall solutions in the respective limits. It is worth noting that in case that $\omega_{\mathrm{MHD}}\tau_{\mathrm{w}} \gg 1$, the mode is stabilized via achieving the perfectly conducting wall limit, regardless of its growth rate γ [6].

For practical purposes, it is of interest to reformulate Eq. (2.64) in the following way:

$$\frac{|\tilde{B}_r(r_{\mathrm{s}})|}{|\tilde{B}_\theta(r_{\mathrm{c}})|} = \left(\frac{r_{\mathrm{c}}}{r_{\mathrm{s}}}\right)^{m+1} \cdot \frac{\sqrt{m^2 r_{\mathrm{w}}^{4m}\omega^2\tau_{\mathrm{w}}^2(r_{\mathrm{s}}^{2m} + r_{\mathrm{c}}^{2m})^2 + [m^2 r_{\mathrm{w}}^{4m} + \omega^2\tau_{\mathrm{w}}^2(r_{\mathrm{w}}^{2m} - r_{\mathrm{s}}^{2m})(r_{\mathrm{w}}^{2m} + r_{\mathrm{c}}^{2m})]^2}}{\omega^2\tau_{\mathrm{w}}^2(r_{\mathrm{w}}^{2m} + r_{\mathrm{c}}^{2m})^2 + m^2 r_{\mathrm{w}}^{4m}}, \tag{2.66}$$

where r_{c} represents a position at which experimental sensors sensitive to $B_{\theta,\mathrm{II}}$ are located. In Sec. 5.3, the ratio of the perturbation field poloidal components inside ('in') and outside ('out') the conducting structure will become important. Usage of Eqs. (2.61)-(2.62) and Eq. (2.36) results in the expression:

$$\frac{|\tilde{B}_{\theta,\mathrm{out}}|}{|\tilde{B}_{\theta,\mathrm{in}}|} = \left[\frac{m^2 + \omega^2\tau_{\mathrm{w}}^2}{m^2}\left(\frac{r_{\mathrm{c,out}}}{r_{\mathrm{c,in}}}\right)^{m+1} + \frac{\omega^2\tau_{\mathrm{w}}^2}{m^2}\frac{(r_{\mathrm{c,in}})^{m-1}(r_{\mathrm{c,out}})^{m+1}}{r_{\mathrm{w}}^{2m}}\right]^{-1}. \tag{2.67}$$

where $r_{\mathrm{c,in}}$ and $r_{\mathrm{c,out}}$ refer to the radial position of the sensors sensitive to the mode poloidal component located in front and behind the conducting structure, respectively.

From the expressions of the flux function, Eq. (2.61) and Eq. (2.62), the phase difference $\Delta\tilde{\theta}$ across the wall can be derived. This quantity depends on the wall properties and it is related to the force through which the mode loses its momentum to the wall (see Sec. 2.5.3). The angle θ represents a poloidal angle by which the sensors sensitive to the perturbation field are displaced. Similarly to Eq. (2.67), an expression for the phase shift can be established.

2.5.3 Model for mode braking

Mode dynamics

Full mode equation of motion comprises sum of all torques exerted on the mass bounded by the island structure,

$$I\frac{d\omega}{dt} = \sum T_\phi, \tag{2.68}$$

where I is the island moment of inertia, ω is defined by Eq. (2.34) (the subscript 'MHD' is dropped) and ϕ denotes that only toroidal motion of the island is considered. Following Ref. [29], it is assumed that the rotation is driven by viscous coupling between the mode and bulk plasma and the mode decelerates via electromagnetic interaction with the wall of finite resistivity. Two scenarios of the momentum transfer from decelerating mode to the plasma will be considered, accounting either for an isolated island braking or for simultaneous mode and plasma bulk deceleration. For both scenarios, the mass subjected to braking will be adjusted accordingly.

Eq. (2.68), reformulated with force terms F_{VS} and F_{RW} defined below (encompassing the moment of inertia associated with the braking mass), becomes

$$\frac{\mathrm{d}\omega}{\mathrm{d}t} = F_{\mathrm{VS}} - F_{\mathrm{RW}}. \tag{2.69}$$

The model for the viscous force term F_{VS} states that any deviation of the mode rotational frequency from the stationary state ω_0 is counteracted by the perpendicular viscous plasma-mode coupling [6]. The restoring viscous torque is proportional to $\omega - \omega_0$, with the proportionality factor containing the momentum diffusivity coefficient. Specifically, the following expression for the viscous restoring force is adopted [29]:

$$F_{\mathrm{VS}} = \frac{\omega_0}{\tau_{\mathrm{M0}}} - \frac{\omega}{\tau_{\mathrm{M}}}. \tag{2.70}$$

Herein, the global momentum confinement time τ_{M} is related to the plasma viscosity,

$$\tau_{\mathrm{M}} = L_\phi / T_{\mathrm{IN}} = \frac{1}{T_{\mathrm{IN}}} \int M_{\mathrm{eff}} n_{\mathrm{e}} R^2 \omega \,\mathrm{d}V, \tag{2.71}$$

with L_ϕ being the total toroidal angular momentum, T_{IN} the total torque input and M_{eff} the effective nucleon number. In discharges heated by neutral beams, T_{IN} may be fully determined by the torque induced by beams, i.e. $T_{\mathrm{IN}} \approx T_{\mathrm{NBI}}$. In

Sec. 2.3.2, it was mentioned that macroscopic MHD modes are known to deteriorate global confinement properties. In [71], a model describing this deterioration was developed, resulting in an expression for a decrement $\Delta\tau_{\mathrm{E,dec}}$ of the energy confinement time. It was shown that $\Delta\tau_{\mathrm{E,dec}}$ depends on the normalized radius of the mode's rational surface r_{s}/a, as well as the island width w. Often, one can approximate τ_{M} by τ_{E}, with some exceptions, e.g. in the case of discharges with peaked density profiles [72]. Therefore, following [29], the momentum confinement deterioration by the mode is taken into account by including in the mode locking model a correction of τ_{M}:

$$\tau_{\mathrm{M}} = \frac{\tau_{\mathrm{M0}}}{1 + f_{\mathrm{M}} w/a}. \tag{2.72}$$

The subscript '0' refers to the mode-free phase of the discharge and f_{M} is a constant factor that is assumed to represent various effects of confinement degradation not specified in further detail. Experimentally, it is difficult to isolate from f_{M} the effect on the confinement of the mode braking due to the wall drag. Other phenomena, such as the H-L mode transition which usually precedes the disruption onset, contribute to the confinement deterioration as well.

As a consequence of the mode rotation, shielding currents are driven in the vessel. Those currents decay on a time scale characterized by the temporal constant τ_w (see Sec. 2.5.2). Recall that Ohm's and Faraday's laws allow for expressing the shielding current j_{w}. This is further used to evaluate the $\mathbf{F}_{\mathrm{wall}} = \mathbf{j} \times \mathbf{B}$ force exerted in turn on the mode, leading to the decrease of mode's rotational frequency. In particular, the toroidal and poloidal components of the force are bound in the following way [16]:

$$F_{\mathrm{wall},\theta} = j_{\mathrm{w}} \tilde{B}_{\mathrm{r}} = \frac{R}{r}\frac{m}{n} F_{\mathrm{wall},\phi}, \tag{2.73}$$

and $\tilde{B}_{\mathrm{r}}$ is evaluated at $r = r_{\mathrm{w}}$, using Eq. (2.62). Ref. [28] presents the wall force term followingly:

$$F_{\mathrm{RW}} = -A \frac{\omega\tau_{\mathrm{w}}}{(\omega\tau_{\mathrm{w}})^2 + m^2} \left(\frac{w}{a}\right)^4, \tag{2.74}$$

where A is a parameter depending on the mass subjected to braking. Two scenarios of momentum transfer can be considered at the interface between the mode and the plasma bulk:

- Mode momentum losses are perfectly coupled to the motion of the plasma bulk, implying common deceleration ('co' scenario).
- The island deceleration is completely decoupled from the plasma ('de' scenario).

Both situations are illustrated in Fig. 2.11. In the case of perfect coupling, the radial momentum transfer is maximised and the local momentum losses experienced by the mode are instantaneously transferred to deceleration of the plasma bulk over the full radial extent. On the other hand, in the decoupled case the momentum diffusivity at the radii $r_{\mathrm{s}} \pm w/2 = 0$ is zero. It has been earlier reported that the experimental situation is likely a compromise between the two variants [73]. For the parameter A, the following analytical expressions for the 'co' and 'de'

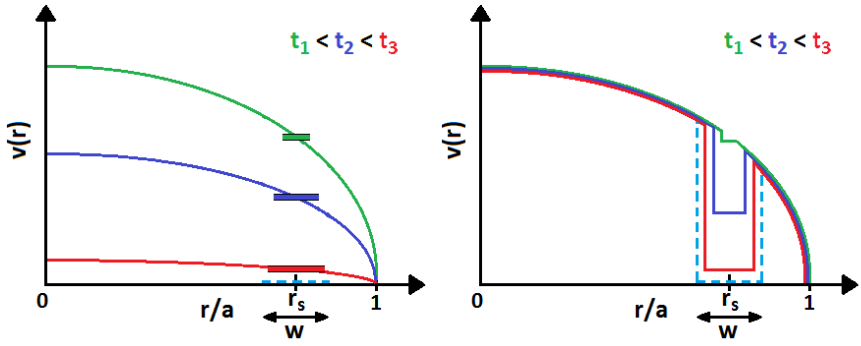

(a) (b)

Figure 2.11: *Schematic illustration of the rotational velocity profile $v(r)$ for the two extreme scenarios 'co' and 'de' for mode deceleration. The profile is depicted at three time points for an island of progressively increasing width w, located at a rational surface $r = r_s$. (a) displays the situation in which momentum losses experienced by the mode are transferred instantaneously to the plasma bulk braking (case 'co'). In (b), the island deceleration is fully decoupled from the plasma bulk movement (case 'de').*

scenarios are obtained, respectively, assuming a flat density profile [16]:

$$A_{\mathrm{co}} = \left(\frac{m}{16}\right)^2 \left(\frac{r_\mathrm{s}}{r_\mathrm{w}}\right)^{2m} \left(\frac{q'}{q}\right)^2_{r_\mathrm{s}} \frac{a^2 B_\theta^2(r_\mathrm{s})}{\mu_0 n_\mathrm{e} m_\mathrm{i}} \frac{2n^2}{R_0^2} = \frac{A_0}{\tau^2_{\mathrm{A,co}}}, \tag{2.75}$$

$$A_{\mathrm{de}} = \left(\frac{m}{16}\right)^2 \left(\frac{r_\mathrm{s}}{r_\mathrm{w}}\right)^{2m} \left(\frac{q'}{q}\right)^2_{r_\mathrm{s}} \frac{a^2 B_\theta^2(r_\mathrm{s})}{\mu_0 n_\mathrm{e} m_\mathrm{i}} \frac{a^2}{r_\mathrm{s} w} \frac{n^2}{R_0^2} = \frac{A_0}{\tau^2_{\mathrm{A,de}}}. \tag{2.76}$$

Here, q' is the radial derivative of the safety factor,

$$A_0 = \frac{m^2}{256} \left(\frac{r_\mathrm{s}}{r_\mathrm{w}}\right)^{2m} \left(\frac{q'}{q}\right)^2_{r_\mathrm{s}} a^2$$

and

$$\tau^2_{\mathrm{A,co}} = \frac{\mu_0 n_\mathrm{e} m_i R_0^2}{2n^2 B_\theta^2(r_\mathrm{s})}, \qquad \tau^2_{\mathrm{A,de}} = \frac{\mu_0 n_\mathrm{e} m_i R_0^2 r_\mathrm{s} w}{n^2 B_\theta^2(r_\mathrm{s}) a^2} \quad (n_\mathrm{e} \approx n_\mathrm{i})$$

are the associated Alfvén times. Frequency dependent part of the wall force is peaked, with the maximum located at $\omega\tau_w = m$.

The locking duration t_{lock}, one of the parameters of interest within the scope of disruption avoidance, is defined as the time interval from the initiation of the frequency decay from the mode's initial angular frequency ω_0 until the locked state. It can be shown that for a mode growth prescribed by a power law in η

$$\frac{w}{a}(t) = (\gamma t)^\eta + \left(\frac{w}{a}\right)_{\mathrm{off}}, \tag{2.77}$$

with γ a parameter describing the mode growth rate, $(w/a)_{\mathrm{off}}$ an offset mode width and under the condition $\omega_0\tau_{\mathrm{w}}/\sqrt{2} \gg m$, the ratio of the braking phase durations for the 'co' and 'de' scenarios is the following:

$$\frac{t_{\mathrm{lock,co}}}{t_{\mathrm{lock,de}}} = \left(\frac{A_{\mathrm{de}}}{A_{\mathrm{co}}}\right)^{1/5} = \left(\frac{1}{2}\frac{a^2}{r_{\mathrm{s}}w}\right)^{1/5}, \tag{2.78}$$

implying that $t_{\mathrm{lock,co}} > t_{\mathrm{lock,de}}$.

Combination of Eq. (2.69) with Eq. (2.70) and Eq. (2.74) yields the expression for the mode frequency evolution:

$$\frac{\mathrm{d}\omega}{\mathrm{d}t} = \frac{\omega_0}{\tau_{\mathrm{M0}}} - \frac{\omega(1+f_{\mathrm{M}}w/a)}{\tau_{\mathrm{M0}}} - A\left[\frac{w}{a}(t)\right]^4 \frac{\omega\tau_{\mathrm{w}}}{(\omega\tau_{\mathrm{w}})^2+m^2}. \tag{2.79}$$

Numerical integration of Eq. (2.79) can provide an estimate of the braking duration t_{lock}. The critical condition for locking is discussed in the following section.

Note that the model for mode braking presented here incorporates only two force terms. The force arising for example from the interaction of the mode field with device error fields (see Sec. 2.5.4), is neglected, as the error fields are often of too low an intensity or corrected by external actuators [74–77]. This force term thus typically becomes important only at the final stage of locking, i.e. the mode coming to a complete rest, not examined here.

Condition for mode locking

For the purpose of derivation of the condition for mode locking, static solutions of Eq. (2.79) are examined by posing $\dot{\omega} = 0$. In the following, the normalized island width will be progressively increased and solutions of static equation of motion in terms of $\omega\tau_{\mathrm{w}}$ will be derived. For a given mode width, those solutions represent situations with balanced forces [78, 79]. Eq. (2.79), reformulated in the following way,

$$\frac{d(\omega\tau_w)}{dt} = \frac{1}{\tau_{M0}}\left(\omega_0\tau_w - \omega\tau_w\left(1+f_{\mathrm{M}}\frac{w}{a}\right)\right) - A\tau_w\left(\frac{w}{a}\right)^4 \frac{\omega\tau_w}{(\omega\tau_w)^2+m^2}, \tag{2.80}$$

allows to calculate the difference between F_{VS} and F_{RW} in terms of $\omega\tau_{\mathrm{w}}$ for a given (w/a). In the static case, $d(\omega\tau_w)/dt = 0$, Eq.(2.80) can adopt a cubic function form,

$$\begin{aligned}(\omega\tau_w)^3 - (\omega\tau_w)^2\frac{\omega_0\tau_w}{1+f_{\mathrm{M}}\frac{w}{a}} + \omega\tau_w\left[m^2 + A\tau_{M0}\tau_w\left(\frac{w}{a}\right)^4\frac{1}{1+f_{\mathrm{M}}\frac{w}{a}}\right] \\ - \frac{\omega_0\tau_w m^2}{1+f_{\mathrm{M}}\frac{w}{a}} = 0.\end{aligned} \tag{2.81}$$

Roots of the cubic function represent the above mentioned points of balanced forces. Six scenarios (I.-VI.) can be encountered for a given mode width. In scenario I., the forces are equal at exactly one point (for illustration emphasized as $\omega\tau_{\mathrm{w}} = \omega_{\mathrm{s}}\tau_w$ in Fig. 2.12) and the $F_{\mathrm{VS}} - F_{\mathrm{RW}}$ function is strictly monotonic. Forces balance at exactly one point again in scenario II., but the $F_{\mathrm{VS}} - F_{\mathrm{RW}}$ function is not strictly monotonic, local extrema $\omega_{\mathrm{l,min}}\tau_{\mathrm{w}}$ and $\omega_{\mathrm{l,max}}\tau_{\mathrm{w}}$ can be distinguished

('l' stands for 'local'). Exact values of the extrema can be determined by searching for the roots of Eq. (2.79) derivative,

$$\frac{d}{d(\omega\tau_{\mathrm{w}})}\left(\frac{d(\omega\tau_{\mathrm{w}})}{dt}\right) = \frac{d}{d(\omega\tau_{\mathrm{w}})}\left(F_{\mathrm{VS}} - F_{\mathrm{RW}}\right) = -\frac{1}{\tau_{\mathrm{M}}} - A\tau_{\mathrm{w}}\left(\frac{w}{a}\right)^4\left[\frac{m^2-(\omega\tau_{\mathrm{w}})^2}{[(\omega\tau_{\mathrm{w}})^2+m^2]^2}\right] = 0. \tag{2.82}$$

Manipulation with Eq. (2.82) leads to solving the following equation:

$$(\omega\tau_{\mathrm{w}})^4 + (\omega\tau_{\mathrm{w}})^2\left[2m^2 - A\tau_{\mathrm{M}}\tau_{\mathrm{w}}\left(\frac{w}{a}\right)^4\right] + m^4 + Am^2\tau_{\mathrm{M}}\tau_{\mathrm{w}}\left(\frac{w}{a}\right)^4 = 0 \tag{2.83}$$

and search for roots of Eq. (2.83) is done upon substituting $(\omega\tau_{\mathrm{w}})^2 \equiv x$. The solutions are the following:

$$x_{1,2} = -m^2 + \frac{1}{2}A\tau_{\mathrm{M}}\tau_{\mathrm{w}}\left(\frac{w}{a}\right)^4 \pm \frac{1}{2}\sqrt{A\tau_{\mathrm{M}}\tau_{\mathrm{w}}}\left(\frac{w}{a}\right)^2\sqrt{A\tau_{\mathrm{M}}\tau_{\mathrm{w}}\left(\frac{w}{a}\right)^4 - 8m^2}. \tag{2.84}$$

It is required that $x_{1,2} \in \Re$, i.e.

$$A\tau_{\mathrm{M}}\tau_{\mathrm{w}}\left(\frac{w}{a}\right)^4 > 8m^2, \tag{2.85}$$

rewritten as

$$\frac{w}{a}\frac{1}{\sqrt[4]{1+f_{\mathrm{M}}\frac{w}{a}}} > \sqrt[4]{\frac{8m^2}{A}\frac{1}{\tau_{\mathrm{M0}}\tau_{\mathrm{w}}}}. \tag{2.86}$$

Backward substitution yields the 4 solutions of Eq. (2.82), $\{\omega_{\mathrm{l,min/max}}\tau_{\mathrm{w}}\}_{\mathrm{i}} = \pm\sqrt{x_{1,2}}$, $i = [1,2]$. Eq. (2.83) is an even function, therefore only positive solutions are of interest,

$$\omega_{\mathrm{l,min}}\tau_w = \sqrt{-m^2 + \frac{1}{2}A\tau_{\mathrm{M}}\tau_{\mathrm{w}}\left(\frac{w}{a}\right)^4 - \frac{1}{2}\sqrt{A\tau_{\mathrm{M}}\tau_{\mathrm{w}}}\left(\frac{w}{a}\right)^2\sqrt{A\tau_{\mathrm{M}}\tau_{\mathrm{w}}\left(\frac{w}{a}\right)^4 - 8m^2}}, \tag{2.87}$$

$$\omega_{\mathrm{l,max}}\tau_{\mathrm{w}} = \sqrt{-m^2 + \frac{1}{2}A\tau_{\mathrm{M}}\tau_{\mathrm{w}}\left(\frac{w}{a}\right)^4 + \frac{1}{2}\sqrt{A\tau_{\mathrm{M]}\tau_{\mathrm{w}}}\left(\frac{w}{a}\right)^2\sqrt{A\tau_{\mathrm{M}}\tau_{\mathrm{w}}\left(\frac{w}{a}\right)^4 - 8m^2}}}. \tag{2.88}$$

Condition of existence of real solutions $\omega_{\mathrm{l,max/min}}\tau_{\mathrm{w}}$ can be formulated as

$$\left(\frac{w}{a}\right)^4\frac{1}{1+f_{\mathrm{M}}\frac{w}{a}} + \left(\frac{w}{a}\right)^2\frac{1}{A\tau_{\mathrm{M0}}\tau_{\mathrm{w}}}\sqrt{\frac{A\tau_{\mathrm{M0}}\tau_{\mathrm{w}}}{1+f_{\mathrm{M}}\frac{w}{a}}}\sqrt{A\tau_{\mathrm{M0}}\tau_{\mathrm{w}}\frac{1}{1+f_{\mathrm{M}}\frac{w}{a}}\left(\frac{w}{a}\right)^4 - 8m^2} > \frac{2m^2}{A\tau_{\mathrm{M0}}\tau_{\mathrm{w}}}. \tag{2.89}$$

In scenario III., the forces are balanced at two different points. In particular,

$$\frac{1}{\tau_{\mathrm{M0}}}\left(\omega_0\tau_{\mathrm{w}} - \omega_{\mathrm{s,min}}\tau_{\mathrm{w}}\left(1+f_{\mathrm{M}}\frac{w}{a}\right)\right) - A\tau_{\mathrm{w}}\left(\frac{w}{a}\right)^4\frac{\omega_{\mathrm{s,min}}\tau_{\mathrm{w}}}{(\omega_{\mathrm{s,min}}\tau_{\mathrm{w}})^2+m^2} = 0, \tag{2.90}$$

where $\omega_{\mathrm{l,min}} \equiv \omega_{\mathrm{s,min}}$ and $\mathrm{sign}((F_{\mathrm{VS}} - F_{\mathrm{RW}})(\omega_{\mathrm{l,max}}\tau_{\mathrm{w}})) > 0$. Forces are balanced for 3 different $\omega\tau_{\mathrm{w}}$ in scenario IV., $\mathrm{sign}((F_{\mathrm{VS}} - F_{\mathrm{RW}})(\omega_{\mathrm{l,min}}\tau_{\mathrm{w}})) < 0$ and $\mathrm{sign}((F_{\mathrm{VS}} - F_{\mathrm{RW}})(\omega_{\mathrm{l,max}}\tau_{\mathrm{w}})) > 0$. In scenario V., $\mathrm{sign}((F_{\mathrm{VS}} - F_{\mathrm{RW}})(\omega_{\mathrm{l,min}}\tau_{\mathrm{w}})) < 0$ and

$$\frac{1}{\tau_{\mathrm{M0}}}\left(\omega_0\tau_{\mathrm{w}} - \omega_{\mathrm{s,max}}\tau_w\left(1 + f_{\mathrm{M}}\frac{w}{a}\right)\right) - A\tau_{\mathrm{w}}\left(\frac{w}{a}\right)^4 \frac{\omega_{\mathrm{s,max}}\tau_{\mathrm{w}}}{(\omega_{\mathrm{s,max}}\tau_{\mathrm{w}})^2 + m^2} = 0. \quad (2.91)$$

for $\omega_{\mathrm{l,max}} \equiv \omega_{\mathrm{s,max}}$. Finally, in case VI., forces are again balanced for only one particular mode frequency.

For each solution of the force balance equation (being it the case of one root or multiple roots), one can consider stability of the solution in case of adding a positive or negative increment ($\pm\Delta\omega\tau_{\mathrm{w}}$) in the frequency domain. For scenarios I.-IV., solutions are stable, or recover stable solution in the close frequency range. An example can be the case of $\omega_{\mathrm{s,min}}\tau_{\mathrm{w}}$ solution in scenario III. For $\omega_{\mathrm{s,min}}\tau_{\mathrm{w}} + \Delta\omega\tau_{\mathrm{w}}$, $F_{\mathrm{VS}} > F_{\mathrm{RW}}$ and the larger viscous force restores the solution. For a negative frequency increment, $\omega_{\mathrm{s,min}}\tau_{\mathrm{w}} - \Delta\omega\tau_{\mathrm{w}}$, $F_{\mathrm{VS}} > F_{\mathrm{RW}}$, and the forces would be rebalanced again at the $\omega_{\mathrm{s,min}}\tau_{\mathrm{w}}$ root. Similar reasoning applies to other roots appearing in scenarios I.-IV. In scenario V. a negative frequency increment to the root $\omega_{\mathrm{s,max}}\tau_{\mathrm{w}}$ would only lead to further frequency decrease (due to $F_{\mathrm{VS}} < F_{\mathrm{RW}}$) and the stable solution would only be reached at the 'distant' (in the frequency domain) second root. Therefore, large variation in frequency would be observed. This sudden 'jump' in the frequency domain is referred to in literature as reaching a 'forbidden frequency' range [78]. The limits of the forbidden frequency interval are given by the two roots of the $F_{\mathrm{VS}} - F_{\mathrm{RW}}$ function. Note that it is for the scenario V. where $d\omega\tau_{\mathrm{w}}/dt = F_{\mathrm{VS}} - F_{\mathrm{RW}} \leq 0$ for all frequencies larger than the first root. In scenario VI. the time derivative is strictly negative on the respective frequency interval.

The above considerations imply that for a certain interval of normalized island widths, the force balance yields multiple solutions for stable $\omega\tau_{\mathrm{w}}$. This interval is delimited by scenarios III. and V., i.e. $(w/a) \in [(w/a)_{\mathrm{crit,min}}\ (w/a)_{\mathrm{crit,max}}]$ (see Fig. 2.12). However, it is for $(w/a) = (w/a)_{\mathrm{crit,max}}$ that from the stability considerations, the solution of the force balance, $\omega_{\mathrm{s,max}}$, 'runs away' quickly towards the low frequency root, 'jumping' over the forbidden frequency range, i.e. the locking bifurcation takes place.

One can consider this island width to be critical from the mode locking avoidance point of view. $\{w/a_{\mathrm{crit,max}}, \omega_{\mathrm{s,max}}\tau_{\mathrm{w}}\}$ pair thus represents the ultimate point of interest for the mode locking avoidance schemes and the Eqs. (2.86)-(2.91) combined yield the exact existence conditions of the $\{w/a_{\mathrm{crit,max}}, \omega_{\mathrm{s,max}}\tau_{\mathrm{w}}\}$ pair for this mode locking model, further illustrated for an arbitrary set of input parameters in Fig. 2.13. $F_{\mathrm{VS}} - F_{\mathrm{RW}}$ functions for the six respective scenarios are plotted in graph Fig. 2.13a, with an emphasis on colour and symbol coding of the points of balanced forces. In Fig. 2.13b, only the frequencies corresponding to the balanced forces are plotted as a function of monotonically increasing (w/a). At $(w/a) = (w/a)_{\mathrm{crit,min}}$, first multiple root appears. Two individual force balance solutions following this multiple root continue to increase/decrease in the frequency domain, respectively, for increasing (w/a). At $(w/a) = (w/a)_{\mathrm{crit,max}}$, second multiple root appears, denoting the unstable force balance solution. Fluctuation in frequency domain leads here to restoration of the balanced point at the low frequency range, jumping over the forbidden frequency interval. Extent of the

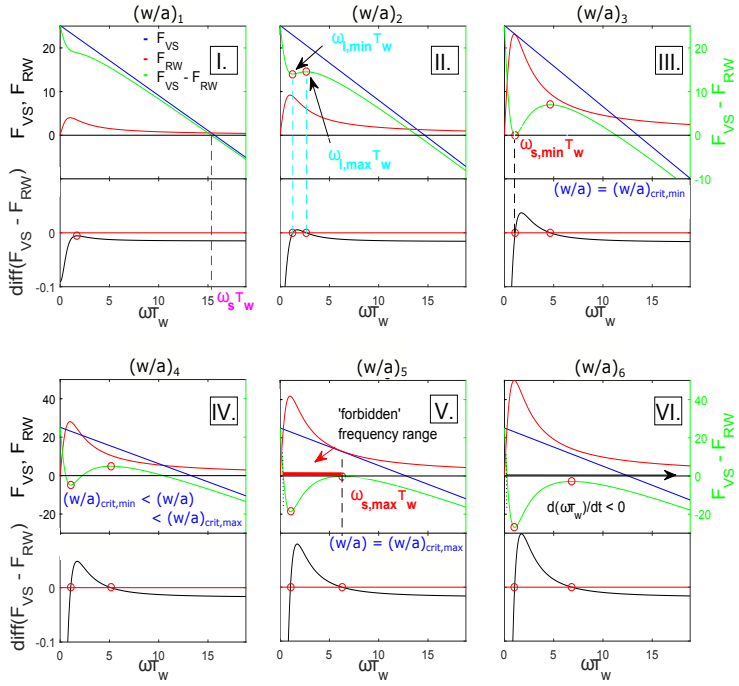

Figure 2.12: *Eq.* (2.79) *evaluated for respectively increasing* (w/a), $(w/a)_{\mathrm{i}} > (w/a)_{\mathrm{j}}$, $i > j$ ($f_{\mathrm{M}} = 0$, $\tau_{M0} = 1$ *s*, $A\tau_{\mathrm{w}} = 1$, $\tau_w = 1$ *ms*, $\omega_0/2\pi = 4$ *kHz*, $m = 1$) *for the six scenarios of interest. Upper plot shows* F_{VS}, F_{RW} *and* $F_{\mathrm{VS}} - F_{\mathrm{RW}} = f(\omega\tau_{\mathrm{w}})$ *for given* (w/a). *Lower plot displays* $d(F_{\mathrm{VS}} - F_{\mathrm{RW}})/d(\omega\tau_{\mathrm{w}})$ *(note the encircled roots of the derivative, corresponding to the extrema in the* $F_{\mathrm{VS}} - F_{\mathrm{RW}}$ *plot).*

forbidden frequency band can be readily retrieved from the graphics.

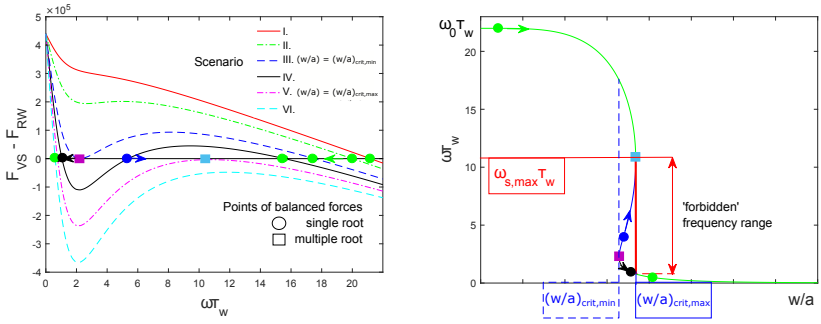

(a) (b)

Figure 2.13: *(a) $F_{\mathrm{VS}} - F_{\mathrm{RW}}$ functions for the six respective scenarios introduced in Fig. 2.12. Note the distinct colour and symbol coding of the points of balanced forces. (b) Frequencies corresponding to the balanced forces plotted as a function of monotonically increasing (w/a). Note that for this mode locking model, the mode frequency asymptotically approaches zero, $\omega\tau_{\mathrm{w}} \to 0$ for $w/a \to 1$, but never decays to the actual locked state, $\omega\tau_{\mathrm{w}} = 0$. Decay to the locked state is assured by adding additional terms in the force balance equation, such as the force applied on the mode due to interaction with external error fields [78].*

Eqs. (2.86)-(2.91) provide formula for the $\{(w/a)_{\mathrm{crit,max}}, \omega_{\mathrm{s,max}}\tau_{\mathrm{w}}\}$ pair. Condition given by Eq. (2.85) defines existence interval of real solutions prescribed by Eq. (2.84). For further increasing mode width, the following condition is fulfilled:

$$A\tau_{\mathrm{M}}\tau_{\mathrm{w}}\left(\frac{w}{a}\right)^4 \gg 8m^2. \tag{2.92}$$

In this limit, expression for the solution of Eq. (2.82) simplifies considerably to:

$$\omega_{\mathrm{s,max}}\tau_{\mathrm{w}} = \sqrt{A\tau_{\mathrm{M}}\tau_{\mathrm{w}}}\left(\frac{w}{a}\right)^2 \tag{2.93}$$

and

$$\omega_{\mathrm{s,min}}\tau_{\mathrm{w}} = \sqrt{-m^2},\ \omega_{\mathrm{s,min}}\tau_{\mathrm{w}} \notin \Re. \tag{2.94}$$

This situation corresponds to the high frequency limit of Eq. (2.91). Series expansion of Eq. (2.91) at this limit adopts the following form:

$$\frac{1}{\tau_{\mathrm{M0}}}\left(\omega_0\tau_{\mathrm{w}} - \omega_{\mathrm{s,max}}\tau_{\mathrm{w}}\left(1 + f_{\mathrm{M}}\frac{w}{a}\right)\right) - A\tau_{\mathrm{w}}\left(\frac{w}{a}\right)^4 \frac{1}{\omega_{\mathrm{s,max}}\tau_{\mathrm{w}}} = 0, \tag{2.95}$$

which then leads to the expression for the critical normalized width,

$$\left(\frac{w}{a}\right)^2\left[\left(1 + f_{\mathrm{M}}\frac{w}{a}\right)^{3/2} + \sqrt{1 + f_{\mathrm{M}}\frac{w}{a}}\right]\Bigg|_{\mathrm{crit,max}} = \frac{\omega_0\tau_{\mathrm{w}}}{\sqrt{A\tau_{M0}\tau_{\mathrm{w}}}}. \tag{2.96}$$

In the limit of $f_{\mathrm{M}} = 0$, the expression reduces to:

$$(w/a)_{\mathrm{crit,max,co}} = \left(\frac{\omega_0 \tau_{\mathrm{A,co}}}{2}\right)^{1/2} \left(\frac{\tau_{\mathrm{w}}}{\tau_{\mathrm{M0}} A_0}\right)^{1/4}, \tag{2.97}$$

$$(w/a)_{\mathrm{crit,max,de}} = \left(\frac{\omega_0 \tau_{\mathrm{A,de}} a}{2w}\right)^{2/3} \left(\frac{\tau_{\mathrm{w}}}{\tau_{\mathrm{M0}} A_0}\right)^{1/3}, \tag{2.98}$$

for the case of plasma braking and for isolated island braking, respectively. Recall that $\tau_{\mathrm{A,de}} \propto w/a$, therefore right-hand side of Eq. (2.98) does not depend on the island width. In Ref. [29], it has been shown that in this high frequency limit,

$$\omega_{\mathrm{s,max}} \tau_{\mathrm{w}} = \frac{\omega_0 \tau_{\mathrm{w}}}{2\left(1 + f_{\mathrm{M}} \frac{w}{a}\right)}. \tag{2.99}$$

It is worth examining whether a specific interval of $\omega\tau_{\mathrm{w}}$ exists for which the static force balance equation has strictly one real solution. For simplicity, $f_{\mathrm{M}} = 0$, m = 1 is considered first. Static Eq. (2.79) then reduces to:

$$\omega_0 \tau_{\mathrm{w}} - \omega \tau_{\mathrm{w}} = \alpha \frac{\omega \tau_{\mathrm{w}}}{(\omega \tau_{\mathrm{w}})^2 + 1}, \tag{2.100}$$

where $\alpha = A(w/a)^4 \tau_{\mathrm{M0}} \tau_{\mathrm{w}}$. Further manipulation with Eq. (2.100) leads to the simplified form of the cubic Eq. (2.81):

$$(\omega \tau_{\mathrm{w}})^3 - (\omega \tau_{\mathrm{w}})^2 \omega_0 \tau_{\mathrm{w}} + \omega \tau_{\mathrm{w}}(1 + \alpha) - \omega_0 \tau_{\mathrm{w}} = 0. \tag{2.101}$$

Strictly negative discriminant of Eq. (2.101) ($\Delta < 0$) sets the condition on existence of exactly one real solution,

$$\Delta = -4(\omega_0 \tau_{\mathrm{w}})^4 + (\omega_0 \tau_{\mathrm{w}})^2(\alpha^2 + 20\alpha - 8) - 4(1 + \alpha)^3 < 0. \tag{2.102}$$

Variable parameters in Eq. (2.102) are $\omega_0\tau_{\mathrm{w}}$ and α, both being strictly positive. As can be seen in Fig. (2.14), for progressively increasing $\omega_0\tau_{\mathrm{w}}$, $\Delta = f(\omega_0\tau_{\mathrm{w}} = (\omega_0\tau_{\mathrm{w}})_{\mathrm{fixed}}, a)$ passes from being strictly negative to mixed signs as a function of α. Positive root of the derivative of discriminant with respect to α,

$$\begin{aligned} \frac{d\Delta}{d\alpha} &= \alpha^2 - \alpha\left(\frac{1}{6}\omega_0 \tau_{\mathrm{w}}^2 - 2\right) - \frac{5}{3}\omega_0 \tau_{\mathrm{w}}^2 + 1 = 0, \\ \alpha_+ &= -1 + \frac{(\omega_0 \tau_{\mathrm{w}})^2}{12} + \frac{\omega_0 \tau_{\mathrm{w}}}{2}\sqrt{\frac{(\omega_0 \tau_{\mathrm{w}})^2}{36} + 6}, \end{aligned} \tag{2.103}$$

yields the position of the maximum of the discriminant distribution in the $\{\omega_0\tau_{\mathrm{w}} > 0, \alpha > 0\}$ plane, $\max(\Delta(\omega_0\tau_{\mathrm{w}}, \alpha_+))$. Eq. (2.102) recalls the condition of the strictly negative sign of Δ at this maximum, $\max(\Delta(\omega_0\tau_{\mathrm{w}}, \alpha_+)) < 0$. The problem is reduced to search for validity of Eq. (2.102) for $\alpha = \alpha_+$. Calculation yields the following formula:

$$\omega_0 \tau_{\mathrm{w},0}(\omega_0 \tau_{\mathrm{w,lim}} - 3\sqrt{3}) < 0. \tag{2.104}$$

Since of interest is the interval of positive frequencies, of relevance is the $\omega_0\tau_{\mathrm{w,lim}} = 3\sqrt{3}$ root and the resulting inequality

$$\omega_0 \tau_{\mathrm{w}} < 3\sqrt{3}. \tag{2.105}$$

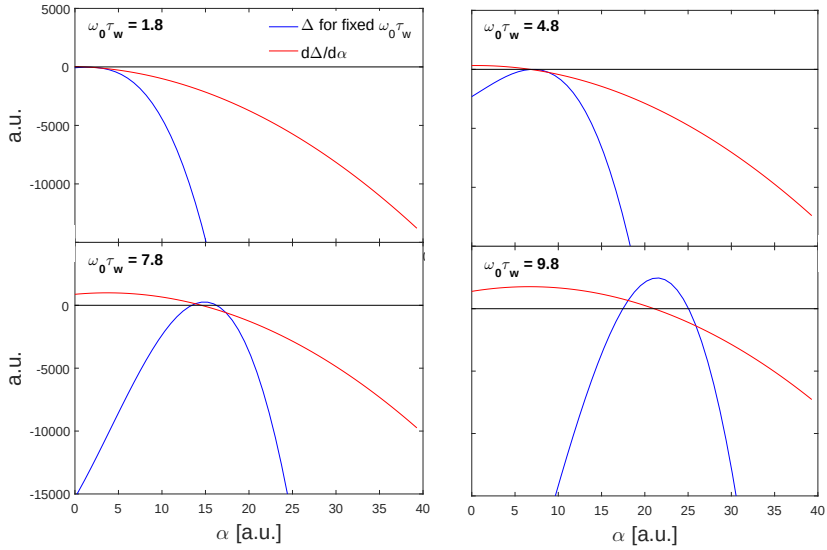

Figure 2.14: *Discriminant of the cubic Eq.* (2.101) Δ *calculated for respectively increasing* $\omega_0\tau_w$ *and its derivative with respect to* α. *Note the transition of strictly negative domain of* Δ *to mixed signs within the range* $\omega_0\tau_w \in [4.8\ 7.8]$. *Condition for* $\Delta < 0$ *is fulfilled for* $\omega_0\tau_w = 3\sqrt{3} \approx 5.20$.

Interval of validity of Eq. (2.102) in the $\{\omega_0\tau_w > 0, \alpha > 0\}$ plane is shown in Fig. 2.15a. Note that when Eq. (2.105) is fulfilled, one stable real solution of Eq. (2.100) exists for $\forall\alpha > 0$, as illustrated in Fig. 2.15b. In such case, no forbidden frequency range is defined and the transition from high to low frequency interval of mode rotation is smooth.

For arbitrary $m > 1$, $\alpha_+ = -m^2 + (\omega_0\tau_w)^2/12 + \omega_0\tau_w/2\sqrt{(\omega_0\tau_w)^2/36 + 6}$ and the condition for the negative discriminant of the cubic equation is modified to:

$$\Delta = -4(\omega_0\tau_w)^4 m^2 + (\omega_0\tau_w)^2(\alpha^2 + 20m^2\alpha - 8m^4) - 4(m^2 + \alpha)^3 < 0. \quad (2.106)$$

It can be shown that the observed dependency $\omega_0\tau_{w,lim} = f(m)$ can be approximated by analytical function of the form $\propto a \cdot m^b + c$, which can be reformulated in an exact way developing upon results obtained in Ref. [78],

$$\omega_0\tau_{w,lim} = 3\sqrt{3} \cdot m, \quad (2.107)$$

defining thus the necessary condition for the locking bifurcation.

Static vs. dynamic condition for locking bifurcation

The critical islands for a locking bifurcation (Eqs. (2.97)-(2.98)) were derived by examining solutions of the static version of equation of motion for a given, in the manipulation progressively increasing, mode normalized width. In practice, static

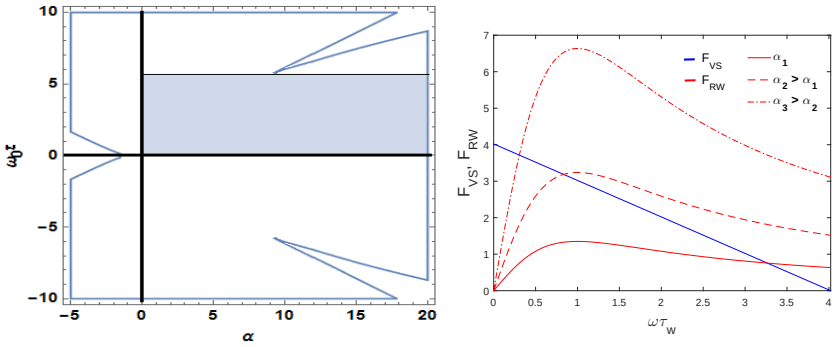

(a) (b)

Figure 2.15: *(a) Interval of validity of Eq.* (2.102) *in the* $\{\omega_0\tau_w > 0, \alpha > 0\}$ *plane (shaded region). (b) When condition given by Eq.* (2.105) *is fulfilled, the transition from the high to low frequency domain of mode rotation is smooth, as for* $\forall\alpha = A(w/a)^4\tau_{M0}\tau_w$ *only one stable solution of the force balance equation exists.*

case can be approached when the mode width evolves on a time scale much longer than that of the momentum redistribution, determined by τ_M. Then, the braking and restoring forces applied on the decelerating mass balance each other at all times [80].

If the island width increases quickly relative to the momentum redistribution, the static critical island width given by Eqs. (2.97)-(2.98), for simplicity from here on denoted as $(w/a)_{crit,s}$, is not an actual point of the locking bifurcation. Fig. 2.16a displays the static braking curve, 'co' scenario, analogical to that shown in Fig. 2.13b ($1/\gamma = 50$ ms, $f_M = 0$, other parameters are given in Tab. 2.1). For the purpose of obtaining the curve, the increment in island width was prescribed by Eq. (2.77) with $(w/a)_{off} = 0$. This formula needs an input in terms of the mode growth rate (adopted from the table), although strictly speaking, the static curve is constructed for an arbitrary (increasing) $(w/a) \neq f(t)$. The cyan arrow in the figure refers to the fulfilment of condition given by Eq. (2.85), i.e. for any increasing (w/a), the solutions of Eq. (2.81) are real. The black and red arrows delimit the interval of (w/a) for which multiple force balance solutions exist. For comparison, the *numerically integrated* braking curve (obtained by integration of Eq. (2.79)) is shown in the same plot (magenta curve), 'co' scenario (same parameters as for the static curve were adopted and $\gamma\tau_{M0} = 1$). It can be seen that the integrated curve decays to the locked state at around three times 'later' than the static curve (recall that for the static case, $(w/a) \neq f(t)$).

According to Eq. (2.99), a locking bifurcation occurs at half of the initial rotational frequency of the mode ($f_M \to 0$). In the following, the critical island width $(w/a)_{crit,d}$ on the time-dependent braking curve is *defined* at the point where the bifurcation occurs (the subscript 'd' refers to 'dynamic').

It is instructive to compare the static (i.e. obtained by search for solutions of Eq. (2.79) under the neglected time variation of mode frequency for given (w/a)) and dynamic (i.e. numerically integrated Eq. (2.79)) critical island widths, defined above. Using Eq. (2.97) ('co') or Eq. (2.98) ('de') with the values in

Tab. 2.1, $(w/a)_{\mathrm{crit,s}}$ can be calculated, with current profile prescribed by Eq. (2.21) and $j(0) = I_{\mathrm{p}}(\nu+1)/\pi a^2$ [16]. To calculate the dynamic $(w/a)_{\mathrm{crit,d}}$, Eq. (2.79) with $f_{\mathrm{M}} = 0$ can be reformulated in terms of the ratio $w/a(t)/(w/a)_{\mathrm{crit,s}}$ and dimensionless variables $\tilde{t} = t/\tau_{\mathrm{M0}}$, $\tilde{\omega} = \omega/\omega_0$, $\tilde{\gamma} = \gamma\tau_{\mathrm{M0}}$. Using the expression for the mode width growth, Eq. (2.77), ($\eta \geq 1$, $(w/a)_{\mathrm{off}} = 0$), the manipulation results in:

$$\frac{d\tilde{\omega}}{d\tilde{t}} = 1 - \tilde{\omega} - \frac{1}{4\tilde{\omega}} \left[\frac{\tilde{\gamma}\tilde{t}}{(w/a)_{\mathrm{crit,s}}} \right]^{\alpha}. \tag{2.108}$$

Here, $\alpha = 4\eta$ (i.e. $\alpha \geq 4$) for the 'co' case, while $\alpha = 3\eta$ ($\alpha \geq 3$) for 'de'. In addition, the high-frequency limit was adopted, assuming that $m \ll \omega_0\tau_{\mathrm{w}}$. Eq. (2.108) was integrated until $t = 1$ s in the scope of a parametric scan, where $\tilde{\gamma}$ was varied over several orders of magnitude, keeping $\tau_{\mathrm{M}} = \tau_{\mathrm{M0}}$ constant. Several values of α were tested during the scan. Furthermore, $(w/a)_{\mathrm{crit,s}}$ was set to a constant value to allow scan in $\tilde{\gamma}$, in particular to 1, since for this value the fit (described below) was of high confidence for the largest range of α. An example of a parametric scan in the 'co' scenario with $\alpha = 4$ is shown in Fig. 2.16b. For $\tilde{\gamma} \ll 1$, $(w/a)_{\mathrm{crit,d}}$ approaches $(w/a)_{\mathrm{crit,s}}$, since in this case the mode grows slowly in comparison with the momentum redistribution time scale. In the other limit it can be seen that $(w/a)_{\mathrm{crit,d}} \gg (w/a)_{\mathrm{crit,s}}$, suggesting that the mode grows too fast for the forces to balance.

Considering a reasonable range of tokamak sizes and plasma temperatures (determining the plasma resistivity, which in turn sets the actual mode growth rate, see Sec. 2.3.2), the lower limit of $\tilde{\gamma}$ can be estimated to lie around 0.1. Data resulting from the scan, restricted to this lower limit, were fitted with an analytical expression of the form $(w/a)_{\mathrm{crit,d}}/(w/a)_{\mathrm{crit,s}} = c_1[\gamma\tau_{\mathrm{M0}}/(w/a)_{\mathrm{crit,s}}]^{c_2} + c_3$. In turn, this was done for values of α within interval $\alpha = [3\ 10]$, and the curves $c_i(\alpha)$ $(i = 1, 2, 3)$ were then fitted by a simple analytical function. This resulted in $c_1 \sim -0.035\alpha + 1.28$, $c_2 \sim 1/\alpha$ and $c_3 \sim 0.004\alpha + 0.26$. For a given set of input parameters, the expression for the critical island width for the 'co' scenario can be thus formulated in the form ('fit' stands for 'fitted'):

$$\frac{(w/a)_{\mathrm{crit,d,fit}}}{(w/a)_{\mathrm{crit,s}}} = (-0.035\alpha + 1.28) \left[\frac{\gamma\tau_{\mathrm{M0}}}{(w/a)_{\mathrm{crit,s}}} \right]^{1/\alpha} + 0.004\alpha + 0.26. \tag{2.109}$$

The variable $(w/a)_{\mathrm{crit,s}}$ appears in Eq. (2.109) although strictly speaking, it was kept constant during the parametric scan. Its generalization was tested on the case of the example shown in Fig. 2.16a. There, $(w/a)_{\mathrm{crit,s}} = 13.5\%$ (Eq. (2.97)), while $(w/a)_{\mathrm{crit,d}} \approx 31.0\%$, i.e. more than two times larger. Eq. (2.109) results in $(w/a)_{\mathrm{crit,d,fit}} \approx 29.1\%$ which is a good approximation of $(w/a)_{\mathrm{crit,d}}$. Hence, Eq. (2.109) will be used in the application of the mode locking model in Chap. 5 to evaluate the critical island width for the locking bifurcation. Eq. (2.109) should not be used far outside the parameter space in which it was fitted, since the formula can become imprecise. Eq. (2.109) is suitable for a real-time evaluation of the condition for mode locking, but an information concerning the mode growth has to be submitted to the calculation. Finally, it is noted that for $\tilde{\gamma} \gg 1$ the dynamic braking curves are always continuous functions (unlike in the static case due to existence of the forbidden frequency range), whether the condition Eq. (2.107) for the locking bifurcation is satisfied or not.

τ_w (ms)	q_{95}	R_0 (m)	$\omega_0/2\pi$ (kHz)	τ_{M0} (ms)	m/n
1.0	3.6	1.65	3.5	50	2/1

f_M	I_p (MA)	B_t (T)	n_e (m^{-3})	r_w/a	ν
0	1.0	2.5	5.0×10^{19}	1	2

Table 2.1: *Parameter values used for obtaining the solutions of the mode equation of motion shown in Fig. 2.16.*

2.5.4 Locked mode

A mode can turn locked, i.e. static in the laboratory frame, after a period of rotation and deceleration or can be excited locked. In large plasmas, the modes can be destabilized at low plasma rotation, resulting in excitation of nearly-locked modes, but the usual picture of the born-locked mode excitation is associated with an external field penetration [6, 16]. This field can be intentionally induced, for example, by feeding current through the so called resonant magnetic perturbation coils, or it can be intrinsic of the device due to an imperfect alignment of the machine coils. The latter is often reported as the device intrinsic error field. Large devices of presumably slow plasma rotation [64] are considered particularly prone to error field locked modes and in favour of the mode destabilization is a low plasma density (resulting in lower plasma bulk rotation, see Eq. (2.31)) and low edge safety factor (leading to low m/n rational surfaces proximity to the plasma edge). Large plasma volume of ITER together with the expected intensity of intrinsic error fields result in the necessity of the error field correction there [81] to prevent the error field locked mode excitation.

In Fig. 2.4a, a monotone (noisy) growth of the radial component of the mode field, $\tilde{B}_r$, was reported. In Chap. 6 it will be shown that often, the measured mode field amplitude fluctuates, with the fluctuation amplitude exceeding the noise level. Origin of the fluctuations is unclear since they often develop on a too fast a time scale to be resolved by some of the plasma diagnostic sensors. Candidate reasons for the fluctuations are presented in the above mentioned chapter.

Ref. [14] reported on that majority of the modes were locked at the disruption onset. In the same reference, the author retrieved the following empirical formula for the mode amplitude (using detectors sensitive to the radial mode field component of (quasi) stationary modes, see Sec. 3.1.1) at which the disruption was triggered:

$$B_{r,disr}(r_c) = (8.5 \pm 2.5) \cdot I_p^{1.07\pm0.11} \cdot a^{-1.1\pm0.14} \cdot q_{95}^{-1.2\pm0.12} \cdot l_i^{1.2\pm0.12} \cdot \rho_c^{-2.8\pm0.3}. \tag{2.110}$$

where $r_c = |R_{geo} - R_{SC}|$, $\rho_c = |R_{mag} - R_{SC}|/a$, R_{geo} and R_{mag} the geometric and magnetic major radii, respectively. Eq. (2.110) allows estimation of the disruptive mode amplitude in real-time for discharge specific conditions. The formula will be applied and validated on large experimental data set in Chap. 6.

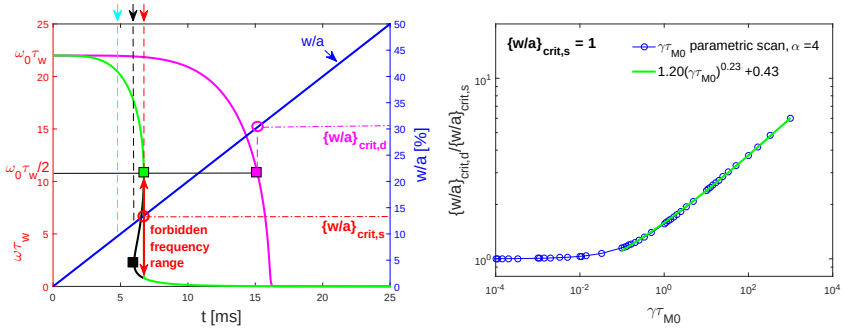

(a) (b)

Figure 2.16: *(a) Comparison of static (green and black) and dynamic (magenta) braking curves in the 'co' scenario. Recall that the static curve was obtained by omitting time variation of mode frequency in equation of motion and search for points of balanced forces for a given mode normalized width, while the dynamic curve was obtained by numerical integration of mode equation of motion. For the purpose of simple visualization, both braking curves are displayed as a function of time, although strictly speaking, the static curve is constructed for an arbitrary (increasing)* $(w/a) \neq f(t)$*. The cyan arrow refers to condition fulfilment of Eq.* (2.85)*. The black and red arrows delimit the interval of* w/a *for which multiple force balance solutions exist. The range of 'forbidden' frequencies is depicted by the double red arrow. (b) The blue solid line indicates* $(w/a)_{\mathrm{crit,d}}/(w/a)_{\mathrm{crit,s}}$ *for a parametric scan of* $\tilde{\gamma} = \gamma\tau_{\mathrm{M0}}$ *in the 'co' scenario, with* $\alpha = 4$ *(the individual points of the scan are encircled). The bold green line results from a fit of the function* $(w/a)_{\mathrm{crit,d}}/(w/a)_{\mathrm{crit,s}} = c_1(\gamma\tau_{\mathrm{M0}})^{c_2} + c_3$ *to the scan points (restricted to* $\tilde{\gamma} \gtrsim 0.1$*).*

3. Experimental setup

The following chapter presents experimental instruments used to retrieve key information concerning the plasma density, temperature, rotation, the mode properties (frequency and amplitude), equilibrium quantities and plasma radiation, all used in the remainder of the thesis. Basic concepts of the diagnostic methods are presented in Sec. 3.1. Sec. 3.2 reports on basic information concerning the devices of interest examined in the scope of single and multi-device approaches adopted in Chap. 5 and Chap. 6.

3.1 Plasma diagnostic methods

3.1.1 Magnetic measurements

Magnetic sensors assure calculation of key plasma parameters and represent a prerequisite for the tokamak operation. Below, basic principle of the measurement will be presented and the description of detection of both rotating and locked modes will follow.

Basic principle

Magnetic sensors sensitive to various fields produced by the tokamak plasma are typically passive and surround the plasma. Magnetic fields are detected by inducing currents in coils of N_{coil} turns. Faraday's law of induction relates the change of the magnetic flux with the electromotence (voltage) captured by the coil, U_{coil},

$$U_{\mathrm{coil}} = \oint_l \boldsymbol{E} \cdot d\boldsymbol{l} = N_{\mathrm{coil}} \cdot \frac{\partial}{\partial t} \int_S \boldsymbol{B} \cdot d\boldsymbol{S}, \tag{3.1}$$

with the surface integral capturing the magnetic flux. This equation implies that the sensors detect temporal variation of the magnetic field, in particular, its component perpendicular to the detection surface S. Hence, U_{coil} has to be integrated, either by using a hardware integrator of characteristic temporal constant or numerically. Note that the smaller is the surface S, the more localized are the measurements.

Illustration of typical set of tokamak magnetic sensors is shown in Fig. 3.1. The so called Rogowski coil is specially designed, by optimizing the winding surface S and implementing a return loop [82], to detect only the poloidal magnetic flux and it is one of the instruments used for calculation of the plasma current I_{p}. The single wired flux loop is typically used to detect the loop voltage V_{loop}. The Mirnov and saddle coils, often used to detect magnetic field components associated with the rotating and locked modes, respectively, are discussed below.

Detection of rotating modes

Mirnov coils, of typically small surfaces, are designed to detect local toroidal, radial and poloidal fields and their high sampling rate assures sensitivity to modes rotating at high frequencies. Since the modes are periodic in space (through the

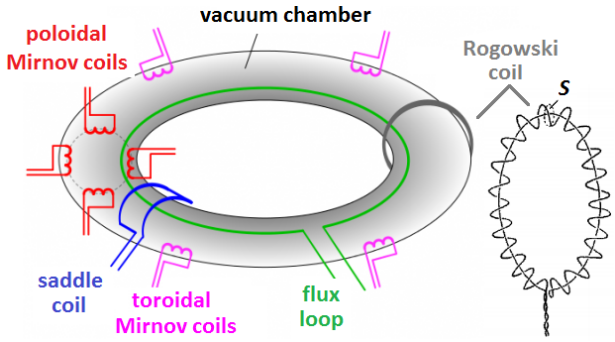

Figure 3.1: *Illustration of magnetic sensors used to detect magnetic fields produced in the tokamak plasma [83].*

associated m/n mode structure), a Fourier transform of the raw signal of typical oscillatory nature allows to retrieve the time variation of the mode amplitude and phase. The length of the temporal window to which the transformation is applied has to be chosen such that a compromise between the time and frequency resolution of the resulting spectrogram is found.

Since the Fourier amplitude is a time derivative of the local field (recall Eq. (3.1)), one obtains the actual mode field $\tilde{B}_{\mathrm{X}}$ (with X substituted by the requested field component) by dividing the Fourier amplitude by the mode frequency f.

Finally, Mirnov coils are often assembled in arrays along the poloidal and/or toroidal coordinates and the analysis of cross-phase and the phase fitting method allow to deduce the mode poloidal and toroidal numbers, respectively, i.e. the mode structure can be identified [27].

Detection of locked modes

The locked mode detectors are typically composed of multiple pairs N_{pair} of saddle coils (SC) displaced by a π/N_{pair} angle toroidally. The geometrical configuration of the coils is typically adjusted to resolve modes of odd toroidal numbers since modes of m/n_{odd} are empirically considered as the most dangerous for inducing disruptions. The radial component of the mode amplitude, $\tilde{B}_{\mathrm{r}}$, can be calculated as a squared sum of differences of fluxes Φ detected by opposing coils, and for j coils located at ϕ_{j} toroidal angles one can formulate the calculation in terms of a least square fit in matrix form,

$$\begin{pmatrix} \sin(\phi_1)-\sin(\phi_2) & \cos(\phi_1)-\cos(\phi_2) \\ \sin(\phi_3)-\sin(\phi_4) & \cos(\phi_3)-\cos(\phi_4) \\ \vdots & \vdots \\ \sin(\phi_{\mathrm{j}-1})-\sin(\phi_{\mathrm{j}}) & \cos(\phi_{\mathrm{j}-1})-\cos(\phi_{\mathrm{j}}) \end{pmatrix} \begin{pmatrix} a \\ b \end{pmatrix} = \begin{pmatrix} \Phi(\phi_1)-\Phi(\phi_2) \\ \Phi(\phi_3)-\Phi(\phi_4) \\ \vdots \\ \Phi(\phi_{\mathrm{j}-1})-\Phi(\phi_{\mathrm{j}}) \end{pmatrix}, \quad (3.2)$$

where a and b are the amplitudes of the $n = 1$ sine and cosine, respectively, and coil '1' is opposite to coil '2', coil '3' opposite to coil '4' etc. For a detector composed of four saddle coils (which will be the case of most of the examined devices, see Sec. 4.3), displaced by $\pi/2$ with respect to each other, the calculation

of the mode amplitude reduces to

$$\tilde{B}_{\mathrm{r}} = \frac{c}{2} \cdot \sqrt{\Big(\Phi(\phi_1) - \Phi(\phi_2)\Big)^2 + \Big(\Phi(\phi_3) - \Phi(\phi_4)\Big)^2} = c \cdot \sqrt{a^2 + b^2}. \tag{3.3}$$

The factor c depends on the coil geometrical properties and relates to the magnetic flux to field conversion. The mode phase is obtained as the inverse tangent of the flux ratio,

$$\text{phase} = \arctan\left(\frac{\Phi(\phi_1) - \Phi(\phi_2)}{\Phi(\phi_3) - \Phi(\phi_4)}\right). \tag{3.4}$$

The measured $\mathrm{d}\tilde{B}_{\mathrm{r}}/\mathrm{d}t$ signal is hardware integrated with a specific integration time constant. The hardware setup, together with wall properties captured in its resistive constant, acts as a low-pass filter with a device-specific upper detectable frequency f_{det} and the locked mode detector can thus recognize modes rotating at frequency $f < f_{\mathrm{det}}$.

3.1.2 Electron density measurements

Various diagnostic methods, such as interferometry, reflectometry, Thomson scattering, use of diagnostic particle beams (such as beam of lithium) etc. are used in tokamak experiments to determine the plasma (electron) density. In the following, principles of interferometry and Thomson scattering, both being active diagnostics, are discussed briefly.

Interferometry

This diagnostic method relies on the dependence of the plasma refractive index on the electron density. Typically, a laser beam is used to probe the plasma and the phase shift it experiences by passing through the plasma volume is proportional to the electron density. The phase shift, obtained by comparing phases of diagnostic and reference beams, reflects the density integrated along the diagnostic beam path of length L_{beam}. Division of the line integrated density by L_{beam} results in the line-averaged density in units $[\mathrm{m}^{-3}]$ [84].

Interferometry yields fast resolved and continuous density measurements, it, however, suffers from several drawbacks. Firstly, the number of diagnostic beams passing the plasma is typically limited and due to the line integration, the capacity of providing density profiles is limited. Secondly, owing to the plasma typical range of densities, the wavelength range of the diagnostic laser beam has to be in micrometers, thus posing restrictions on hardware instruments. Often, HCN, DCN, CO_2/He-Ne lasers are used [85, 86]. Furthermore, depending on multiple factors (such as the working wavelength, plasma size and the density range), the phase shift can exceed 2π, resulting thus in the so called fringes. The miscalculated phase shift can generate fringe jumps that have to be compensated in order to provide correct density calculation [87]. Complete loss of the diagnostic beams can also occur in regions with large density gradients, encountered for example during a pellet injection in the plasma (for fuelling, diagnostic or other experimental purposes) or along appearance of MHD modes. Refraction takes place in the region of the strong gradients and fringe jumps are recognizable in the density time traces too [88].

Thomson scattering (electron density)

Short energetic bursts of diagnostic laser beam into the plasma yield, owing to the Thomson scattering (TS) of the light on the electrons [89], information concerning the electron density by analysis of the intensity of the Doppler broadened scattered spectrum [90]. Time resolution of the method depends on the laser repetition rate, which is typically of the order of tens of miliseconds (unless the laser is operated in the so called pulse-burst mode [91]). Events developing on a time scale lower than this repetition rate are thus undetected by TS. On the other hand, the measurement suffers from no discontinuities analogical to fringe jumps presented in the interferometry case. TS diagnostic allows reconstruction of the density profiles of spatial resolution dependent on the instrument geometrical configuration.

3.1.3 Electron temperature measurements

Temperature of ions and electrons can be different in tokamaks as the collisions between the two species are rare, preventing the temperature equilibration [92]. In the scope of this work, the focus is set on calculation of the electron temperature by means of electron cyclotron emission and Thomson scattering.

Electron cyclotron emission (ECE)

Electrons gyrating in magnetic field emit radiation and the power of the cyclotron radiation is proportional to the emitter temperature [93, 94]. Given that the frequency of gyration ω_{ce} depends on the magnetic field intensity,

$$\omega_{\mathrm{ce}} = \frac{eB}{m_{\mathrm{e}}}, \tag{3.5}$$

it is possible to localize spatially the radiating source. ECE can thus provide radial profiles of temperature and the high temporal resolution of the method allows to study fast phenomena such as thermal quenches during the disruption (in Fig. 2.4b, the first panel shows temperature evolution captured by ECE).

ECE signals, when processed by a Fourier transform, can yield information about the radial extent of a rotating mode, details are provided in Ref. [27]. Here, it is noted that the mode width can be calculated as the distance between the maxima of the Fourier amplitude radial profile and the position of the rational surface is localized at a phase jump by π, recognisable in the radial profile of the Fourier phase.

Thomson scattering (electron temperature)

Analysis of the width of the scattered spectrum yields the electron temperature.

3.1.4 Plasma rotation

The so called charge exchange recombination spectroscopy (CXRS) is widely used for determination of the plasma (ion) rotation in tokamak experiments [95]. For the purpose of the measurement, a diagnostic beam of neutral particles has to be injected in the plasma, often in form of short pulses. Neutrals can lose electrons

to impurity ions present in the plasma (such as boron and carbon). The atoms losing a charge state emit light which is Doppler shifted and the analysis of the shift results in the determination of the ion rotation. Depending on the diagnostic geometrical configuration, a rotation profile might be obtained, since the atomic processes are spatially localized and yield information about the plasma state at the volume where the diagnostic and viewing optics intersect. Usage of a diagnostic beam (occasionally complementary with the heating beam) is a prerequisite for the CXRS measurements.

3.1.5 Equilibrium reconstruction

Solutions of the Grad-Shafranov equation (a formulation of the ideal MHD equilibrium in an axisymmetric configuration, recall Eq. (2.16), Sec. 2.2) are obtained numerically. Codes such as CLISTE [96] and EFIT [97] were developed in the past for this purpose.

For the given device configuration, the codes perform a fit of the current profile while posing a regularization condition (consisting of keeping the curvature as low as possible) on the parametrized measured signals. The equilibrium solution is retrieved iteratively. Input parameters in terms of the internal poloidal magnetic field (obtained typically by the motional stark effect diagnostic [98]), kinetic data (measurements of the plasma temperature and density), and other relevant information, such as localization and radial extent of the MHD modes, can be supplied to the code, increasing thus the precision of the output parameters. Standardly, however, the codes process data from coils only.

3.1.6 Detection of plasma radiation

Energy released from the plasma in form of radiation is typically detected by photo detectors sensitive to a specific spectral range (ultraviolet, soft-X ray etc.). A single diode facing the plasma detects total radiated power integrated along its line-of-sight. To retrieve a spatially localized information about the emitting region, multiple diodes are often arranged in 'fans'. Lines-of-sight of those diodes then cover a sufficiently wide area of the plasma cross-section and the Abel inversion or tomographic reconstruction of the acquired data can then provide cross-sectional 2D plots of the plasma radiation [99].

3.1.7 Cameras

Tokamaks are typically equipped with cameras viewing the vessel interior. The cameras are often sensitive to the range of visible light, but infra-red cameras are often in usage too, for example for recognition of hot surface spots undergoing excessive erosion due to transient events. The frame sampling has to be adjusted to the typical pulse length and the time scale of the studied phenomenon. An example of images taken by a fast camera sensitive to visible light is shown in Fig. 2.9.

3.2 Devices of interest

In the scope of this thesis, data acquired at 4 different tokamaks, COMPASS-D, ASDEX Upgrade, DIII-D and JET were used. The devices differ by plasma minor and major radius, but are of similar aspect ratio A. Furthermore, they all operate under geometrical configuration relevant to ITER, i.e. in a 'single-null' (single X-point) diverted plasmas (see Fig. 3.2). In the following, basic information concerning the devices are presented. Tab. 3.1 summarizes important geometrical and other device characteristics. For reference, ITER data are added to the table.

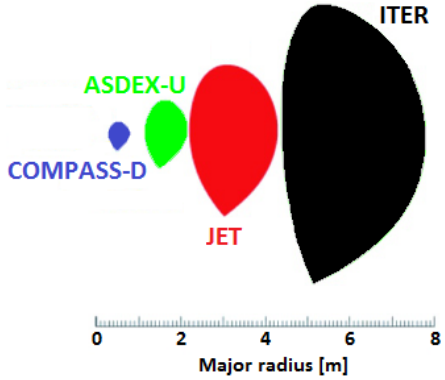

Figure 3.2: *Poloidal cross-sections of the COMPASS-D, ASDEX Upgrade, JET and ITER tokamaks, ordered along the major radius coordinate [100]. The tokamak DIII-D is similar to ASDEX Upgrade in the configuration and it is thus not included in the graphics.*

3.2.1 COMPASS-D

The tokamak COMPASS (COMPact ASSembly, -D denotes the 'D' shaped plasmas) was originally assembled in 1980s in the Culham Science Centre (UK). Its plasma dimensions make it to fall into category of small devices, but its technical configuration allows to operate under ITER-relevant conditions, for example, by achieving the H-mode confinement. The stainless steel vacuum vessel is protected from the heat and particle loads by graphite tiles. In 2006, the tokamak was moved to Prague, Czech republic, and at the time of compilation of this document, its operation was under the control of the Tokamak department of Institute of Plasma Physics (Czech Academy of Science) [101, 102]. Currently, an upgrade of the device is under preparation. The upgraded tokamak, COMPASS-U, will operate under strong magnetic field intensity (up to 5 T) and its experimental mission will, for example, explore the tokamak operation with the liquid metal divertor.

3.2.2 ASDEX Upgrade

The ASDEX (Axially Symmetric Divertor EXperiment) Upgrade middle-sized tokamak, successor of the ASDEX tokamak in which the H-mode was discovered in 1982 [103], went first in operation at the Max-Planck-Insistut fuer Plasmaphysik in Garching, Germany, in 1991. Over the years, the original in-vessel graphite components were coated by tungsten, until the device completed its transition to a full-tungsten wall [104].

3.2.3 DIII-D

The Doublet III machine, the third in a series of non-circular plasma devices operated by the General Atomics in San Diego (USA) evolved in the DIII-D tokamak in 1986 [105]. In the early years of its operation, it achieved the world's highest values of the β parameter and fusion rate. The material in-vessel mixture is similar to that of the COMPASS tokamak and its dimensions are slightly larger than those of the ASDEX Upgrade (resulting in a lower aspect ratio). In the past, the DIII-D experimental mission focused for example on the development of the advanced tokamak operating mode [106].

3.2.4 JET

The JET (Joint European Torus) machine operation was initiated in 1983 at the Culham Centre for Fusion Energy in Oxfordshire, UK. JET is the world's largest tokamak in operation and in the past, deuterium-tritium campaigns took place there. In 1997, the tokamak set the world record in terms of the fusion power output (16 MW), at Q = 0.66 for a transient time period [107]. The D-T campaign motivated the development of a unique remote handling system that is able to replace in-vessel components [108]. In 2009, the original in-vessel machine parts made of carbon were replaced by beryllium and tungsten. The same materials are foreseen for ITER, therefore it is denoted as the JET ITER-like wall configuration [109]. Another D-T campaign, for the first time performed with the ITER-relevant wall materials, is currently under preparation for JET [110]. This campaign will complete the device experimental mission prior to its decommissioning.

Device	COMPASS	AUG	DIII-D	JET	ITER
a (m)	0.23	0.50	0.65	1.0	2.0
R_0 (m)	0.56	1.65	1.67	2.96	6.20
$A = R_0/a$	3.33	3.13	2.78	3.03	3.10
$I_{\mathrm{p,max}}$ (MA)	0.36	1.2	2.0	4.8	15
$B_{\mathrm{t,max}}$ (T)	2.1	3.1	2.2	3.5	5.3
Discharge length (s)	< 0.5	< 10	< 10	< 20	-
First wall material	C	W	C	W&Be	W&Be
$P_{\mathrm{aux,max}}$ (MW)	0.6	27	23	38	50

Table 3.1: *Parameters of devices of interest. The first wall material corresponds to the device experimental year of interest (see Tab. 4.1). The ITER maximum discharge length depends on the experimental scenario.*

4. Assembly of database of disruptive discharges

A database of disruptive discharges, the main working set used in Chap. 5 and Chap. 6, is composed of discharges performed at the four tokamaks presented in Sec. 3.2. It is recalled that the devices are of similar aspect ratio, but differ by the plasma size and the first wall material (see Tab. 3.1). The same criteria were applied on all devices for the database assembly. In Sec. 4.1, the detection of discharges terminated by a disruption is described. Sec. 4.2 reports on the database filtering. The following Sec. 4.3 contains further details concerning the detection of amplitude and phase of rotating and locked modes. In this section, key terms used in Chap. 5 and Chap. 6 are defined, such as the saddle coil signal, mode locked and rotating phase durations. Then, Sec. 4.4 reports on plasma parameters calculated at important time points of the discharge, in accordance with the experimental input necessary for discussion in the following chapters. All disruptive discharges were classified according to the common disruption cause and the description of the classification is discussed in Sec. 4.5.

4.1 Detection of disruptive discharges

Recall that a *major disruption* is defined as a sudden drop in the plasma thermal energy content (the thermal quench), followed by a quench of the plasma current (Sec. 1.4). Vertical destabilization of the plasma column usually accompanies the major disruption. During a *minor disruption* the plasma thermal content can be reduced significantly via a thermal quench too, but the confinement is not completely lost and the plasma often recovers the pre-minor disruption state. Current spikes are recognizable both during the minor and major disruptions and, as was shown in Fig. 2.4, the current spike typically follows shortly after the thermal quench.

All device discharges pertaining to experimental years listed in Tab. 4.1 were scanned and disruptive shots were identified. The choice of campaign years was based on availability of the experimental input necessary for the study of disruption precursors. Furthermore, the device configuration closest to the ITER case was preferred. Therefore, the interest was focused on the JET ITER-like wall and full-W ASDEX Upgrade (AUG) campaigns. An empirical, device-specific threshold on the minimum detected current decay was set, discriminating thus discharges terminated by a controlled ramp-down from those experiencing a current quench [49].

The disruption could take place in any part of the discharge, but to be further considered, the plasma current at $t = t_{\mathrm{disr}}$ was required to be equal or larger than 35% of that of the (expected) current flat-top phase. This percentage was chosen empirically such that the disruptive discharges of low damaging potential, i.e. those disrupting close to the ramp-down finalization, are excluded from the database. Tab. 4.1 displays the relative occurrence of disruptions in the distinct discharge phases. For discharges disrupting in the current ramp-up phase (RU),

$\Delta I_p/\Delta t > 0$ (I_p is the plasma current and Δt is of the order of milliseconds). For the flat-top (FT) disruptions $\Delta I_p/\Delta t \sim 0$ and in the ramp-down (RD) case, $\Delta I_p/\Delta t < 0$. Furthermore, to be identified as a ramp-down case, $I_p(t = t_{disr})$ was required to be lower than 95% of the plasma current flat-top value. Here, ramp-downs intentionally induced by the plasma control system are not discriminated from the plasma current decrease due to the action of the disruption precursors. Discharges identified as disruptive were further filtered using criteria described in Sec. 4.2 and Sec. 4.3. Disruptions in the RU/FT/RD phases are listed in Tab. 4.1. It can be seen that only in the COMPASS device case, the majority of disruptions took place during the current flat-top phase.

If minor disruptions were observed prior to the major disruption onset, the time of the first minor disruption, $t_{min.disr}$ (set at the onset of the first current spike accompanying a minor thermal quench) was recorded and the number of minor disruptions occurring during the time interval $[t_{min.disr}\ t_{disr}]$, $N_{minor\ disr.}$, was counted. If no minor disruptions were observed prior to t_{disr}, $t_{min.disr} = t_{disr}$ and $N_{minor\ disr.} = 0$. In an example of a disruptive discharge (with disruption induced by a locking 2/1 mode) shown in Fig. 4.1, only one minor disruption took place prior to t_{disr}, in particular at $t_{min.disr} \sim 1.535$ s. The final counting of cases with $N_{minor\ disr.} > 0$ in the devices of interest is displayed in Tab. 4.1. Minor disruptive events were rarely observed in COMPASS, but in AUG and JET they were present in the majority of cases, as can be seen in Tab. 4.1.

4.2 Database filtering

The disruptive shots identified in Sec. 4.1 had to fulfil the following conditions to be included in the database:

- The plasma had to be vertically stable until the major disruption onset.
- Massive gas injection was triggered at the earliest during the current quench phase.
- The resonant magnetic perturbation coils (RMP) were not in operation during the duration of the mode (and shortly before the saddle coil signal onset time), unless used for the correction of the intrinsic error fields[1]. Interaction between the perturbation and external fields produced by the RMP coils is thus not considered in the discussion concerning the experimental saddle coil signal durations in Chap. 6.
- A minimum set of the plasma diagnostic data, yielding information on the mode duration and on the disruption cause (see Sec. 4.5), was available.

The final number of entries included in the database per device, N, is listed in Tab. 4.1.

4.3 Detection of rotating and locked modes

For disruptive discharges identified upon the occurrence of a current quench, data from diagnostics sensitive to both the rotation and locked phase of the mode were manually inspected.

[1] Applies to JET and DIII-D.

Device	COMPASS	AUG	DIII-D	JET
SC location (HFS or LFS)	HFS, LFS	HFS	LFS	LFS
(in or out-vessel)	out, out	in	out	out
R_{SC}/R_0	0.59/1.42	0.66	1.47	1.58
f_{det} (kHz)	~ 5.0	~ 2.1	~ 0.8	~ 0.6
τ_{w} (ms)	0.68*	0.73**	3.0 [29]	5.0 [111]
Experimental period	2014-2017	2012-2016	2015	2011-2012
Number of entries N	252	454	150	256
Discharge phase				
RU/FT/RD (%)	6/61/33	3/30/67	3/29/68	1/14/85
Cases with $N_{\mathrm{minor\ disr.}} > 0$ (%)	3	79	24	81
Mode dynamics				
ROT/IRLM/BLM (%)	50/45/5	27/54/19	21/37/42	4/54/43

Table 4.1: *Parameters concerning the device characteristics and database of disruptive discharges: basic saddle coil (SC) characteristics; database counting and relative occurrences of cases within groups introduced in Sec. 4.1 and Sec. 4.3.* $^*\tau_{\mathrm{w}}$ *calculated with Eq.* (2.59). ** *See Sec. 5.3.*

The mode rotating phase was identified using spectrograms acquired by Mirnov coils that detect the mode poloidal field component $\tilde{B}_\theta$ at the coil position r_{c}. If a conversion to the radial field component at the mode location r_{s} was needed, Eq. (2.66) was used. The mode structure in terms of the toroidal mode numbers (in AUG also the mode poloidal number) was resolved by analysis of the cross-phase (see Sec. 3.1.1).

For the purpose of Chap. 5 (focused on the mode braking model validation), the mode rotation frequency $f = \omega/2\pi$ was tracked in time in AUG using the spectrograms. Further details are provided in Sec. 5.2. An example of a tracked frequency is highlighted by dash-dotted magenta lines in the fourth panel of Fig. 4.1.

The locked mode detectors are composed of four (six in DIII-D) saddle coils (SC) located at $R = R_{\mathrm{SC}}$ along the radial coordinate, displaced by a $\pi/2$ ($\pi/3$) angle toroidally. The mode amplitude $\tilde{B}_{\mathrm{r}}$ and its phase were calculated using Eq. (3.3) and Eq. (3.4), respectively.

In AUG the saddle coils are in-vessel components, in the remaining devices, the coils are located outside of the vessel. The measured signal variations reflect the characteristic vacuum vessel magnetic penetration time, τ_{w}. As introduced in Sec. 3.1.1, the measured $\mathrm{d}\tilde{B}_{\mathrm{r}}/\mathrm{d}t$ signal is hardware integrated with a specific integration time constant and the hardware setup acts as a low-pass filter with a device-specific upper detectable frequency f_{det}. The locked mode detector can recognize modes rotating at frequency $f < f_{\mathrm{det}}$ and the time during which the signal can be distinguished from the noise has been occasionally reported as the *locked mode duration* in the past, although this time can comprise the mode rotation phase. It is important to emphasize that due to the mode rotation and the resulting attenuation of the mode radial field component, the measured amplitude is attenuated until the complete mode locking.

To avoid misleading terminology, the saddle coil signal onset time, t_{SC}, is defined as a time point at which the measured radial field amplitude surpasses the

noise level (see $\tilde{B}_r = f(t)$ in the example of Fig. 4.1, the saddle coil signal onset time is visualized by the green vertical line). The *saddle coil signal duration*, Δt_{SC}, is delimited by the interval $\Delta t_{SC} = t_{disr} - t_{SC}$. The time variation of the mode phase (the third panel in Fig. 4.1) shows that the mode was rotating initially, decaying to the locked state only around a time point highlighted by the cyan dashed line. After this point, the time variation of the phase is minor (not exceeding 180° until the onset of the major disruption). Due to this slight variation in phase, the mode is, strictly speaking, quasi-stationary. In number of examined cases, owing probably to the interaction with the error fields, the mode phase was roughly constant, i.e. the mode was static in the laboratory frame. The *locked phase duration* Δt_{LP} is defined as an interval separating the disruption onset from the moment when the mode becomes (quasi) stationary, $\Delta t_{LP} = t_{disr} - t_{LP}$. In COMPASS, the mode phase was not calculated, Δt_{LP} is defined there as a time interval during which the measured poloidal mode field (detected by the Mirnov coils) evolves without oscillations. The *mode rotation phase* Δt_{ROT} is delimited by the onset of rotating mode and its (quasi) locking. In Fig. 4.1 this interval is emphasized by double black arrows above the fourth panel. This particular time interval will become important in Chap. 5.

An offset in the measured saddle coil signal was manually subtracted to assure a correct mode amplitude calculation. Finally, it is noted that in the case of the COMPASS device, two sets of saddle coils were used for the mode detection, located at the low-field-side (LFS) and high-field-side (HFS) of the vacuum vessel. In other devices, only one set of sensors was used.

The database entries were divided in groups defined according to the mode dynamics:

- Modes (slowly) rotating until the major disruption onset (ROT), $\Delta t_{LP} = 0$.
- Initially rotating locked modes (IRLM), $\Delta t_{SC} > \Delta t_{LP}$, $\Delta t_{LP} \neq 0$.
- Born-locked modes (BLM), $\Delta t_{SC} = \Delta t_{LP}$.

The relative occurrence of entries in ROT/IRLM/BLM groups per device is listed in Tab. 4.1.

From the above it is clear that in all database entries $\Delta t_{SC} > 0$. In Sec. 6.2, this time interval will be used as a measure of the mode duration and multiple factors that can influence this time interval will be discussed therein. Regression analysis of the duration will be restricted in Sec. 6.3 to cases with $\Delta t_{LP} > 0$, as this time interval is assumed to be less influenced by the diagnostic-dependent settings.

4.4 Calculation of plasma parameters at important discharge phases

In this section, ranges of multiple important plasma parameters, calculated at the saddle coil signal and major disruption onset times, i.e. at $t = t_{SC}$ and $t = t_{disr}$, are provided. This information is important in the context of the disruption classification presented in Sec. 4.5. Furthermore, it provides a context for the presentation and discussion of results contained in Chap. 5 and Chap. 6.

The ranges are shown in Tab. 4.2. Plasma density and temperature measurements were preferentially obtained from the plasma core region. Some of the

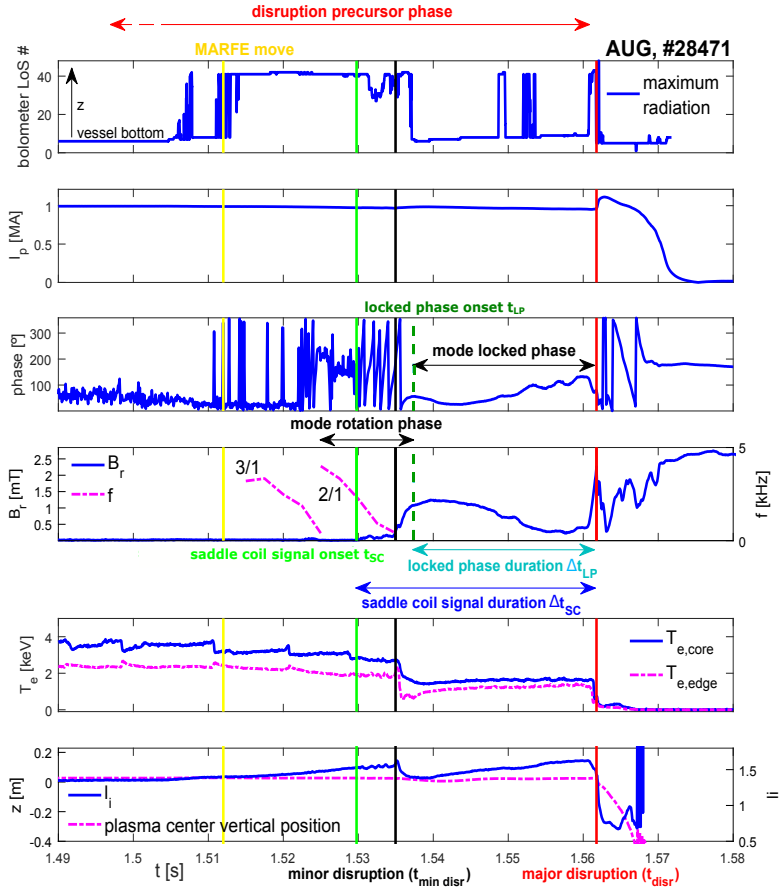

Figure 4.1: *Example of an initially rotating locked mode (an IRLM AUG group entry) disrupting at $t = t_{\mathrm{disr}}$. The disruption precursor phase, consisting of a poloidal destabilization of the MARFE from its position near the plasma X-point and sequential onset of initially rotating 3/1 and 2/1 modes, is highlighted. The calculated radial component of the mode field ($\tilde{B}_{\mathrm{r}}$) surpasses the noise level at $t = t_{\mathrm{SC}}$, determining the starting point of the saddle coil signal duration Δt_{SC}. The mode phase is, however, roughly constant during a time interval Δt_{LP}, defining the locked phase duration. Here, $\Delta t_{\mathrm{LP}} < \Delta t_{\mathrm{SC}}$.*

parameter distributions were considerably skewed, dispersions of the distributions are thus captured by median($x(t = t_{\mathrm{ref}})$) ± MAD, where MAD is the median absolute deviation and t_{ref} is the time of interest. Due to the occasional occurrence of minor disruptions, switching off the external heating modules etc. prior to t_{disr}, the temperature data were, for reference, calculated at one additional time point, at $t = t_{\mathrm{SC}} - \Delta t$ where $\Delta t = [0.02, 0.5, 0.5, 3]$ s for the respective four devices. Those data are displayed in italics in the last row of the table.

Device	COMPASS	AUG	DIII-D	JET
a (m)	0.18 ± 0.01	0.51 ± 0.02	0.60 ± 0.02	0.95 ± 0.03
R_{geo} (m)	0.55 ± 0.01	1.60 ± 0.02	1.68 ± 0.02	2.84 ± 0.04
R_{mag} (m)	0.56 ± 0.01	1.68 ± 0.02	1.73 ± 0.03	2.94 ± 0.02
κ	1.73 ± 0.28	1.60 ± 0.08	1.75 ± 0.12	1.65 ± 0.07
	1.75 ± 0.28	1.55 ± 0.10	1.64 ± 0.14	1.46 ± 0.15
δ_{l}	0.50 ± 0.20	0.35 ± 0.04	0.48 ± 0.14	0.32 ± 0.06
	0.48 ± 0.19	0.33 ± 0.04	0.36 ± 0.19	0.18 ± 0.10
I_{p} (MA)	0.17 ± 0.05	0.79 ± 0.30	1.06 ± 0.18	1.90 ± 0.21
	0.16 ± 0.05	0.74 ± 0.28	0.94 ± 0.18	1.64 ± 0.29
B_{t} (T)	1.17 ± 0.08	2.47 ± 0.18	1.93 ± 0.23	2.18 ± 0.26
l_{i}	1.08 ± 0.05	1.44 ± 0.27	1.07 ± 0.38	1.18 ± 0.19
	1.07 ± 0.15	1.74 ± 0.34	1.53 ± 0.51	1.31 ± 0.10
q_{95}	3.55 ± 0.79	4.73 ± 0.63	4.03 ± 0.75	3.42 ± 0.48
	3.53 ± 0.78	4.77 ± 0.64	4.08 ± 0.82	3.88 ± 0.60
β_{N} (%)	1.07 ± 0.28	0.50 ± 0.33	0.67 ± 0.52	0.20 ± 0.12
	0.91 ± 0.26	0.36 ± 0.18	0.40 ± 0.50	0.26 ± 0.10
P_{NBI} (MW)	0.25 ± 0.06	4.91 ± 2.61	3.78 ± 2.34	2.13 ± 3.05
	0.25 ± 0.06	4.89 ± 2.47	3.50 ± 1.90	1.81 ± 3.08
$n_{\mathrm{e,core}}$ ($10^{19}\mathrm{m}^{-3}$)	5.21 ± 3.02	6.33 ± 3.77	2.90 ± 1.94	3.67 ± 1.58
	5.09 ± 2.85	5.96 ± 2.49	2.71 ± 1.58	2.07 ± 1.29
$T_{\mathrm{e,core}}$ (keV)	0.65 ± 0.23	0.97 ± 0.78	1.53 ± 0.66	0.77 ± 0.58
	0.62 ± 0.22	0.34 ± 0.45	1.50 ± 0.68	0.41 ± 0.21
	0.78 ± 0.39	*1.66 ± 0.97*	*1.55 ± 0.63*	*1.91 ± 0.73*

Table 4.2: *Ranges of various plasma parameters presented in the format median($x(t = t_{\mathrm{ref}})$) ± MAD, $t_{\mathrm{ref}} = t_{\mathrm{SC}}$ (first line) or $t_{\mathrm{ref}} = t_{\mathrm{disr}}$ (second line, not shown if the medians at the two temporal points differ by < 10%). The last row contains T_{e} calculated* $[0.02, 0.5, 0.5, 3]$ *s prior to t_{SC} in the respective devices.*

4.5 Disruption classification

In Ref. [112] a large set of JET disruptive discharges was investigated in detail, with the goal of describing the chain of events leading to a disruption. A classification was presented and in Ref. [56] it was updated for the upgrade to the JET ITER-like wall. The classification was adopted and further developed for the AUG analysis in Ref. [113]. Here, the disruption classification presented in the

references is followed. The description of the disruption classes is provided in the respective sections of this document, see the second column of Tab. 4.3 for the section number.

Each database entry was affiliated with a disruption class. To do so, time traces of the plasma parameters were visually inspected together with the operator comments and, when applicable, records from fast sampling cameras viewing the vessel interior. In classifying the disruption, it was particularly useful to compare the examined discharge plasma parameters within the $l_i(q_{95})$ operation diagrams, constructed at the major disruption onset for each device. Distinct disruption classes tend to be located within different parts of the diagram [73, 113]. Current-driven instabilities, typically triggered when a density limit is approached, tend to be located in the region of highly peaked current profiles, while the pressure-driven instabilities, such as NTMs, have usually a rather flat current profile and thus lower value of l_i. Example of a $l_i(q_{95})$ diagram is shown for the AUG case (restricted to ROT and IRLM database entries, in accordance with Chap. 5) in Fig. 5.10.

The relative occurrence of the classes in a particular device, presented in Tab. 4.3, is a combination of multiple factors. Impurity sources can be related to the level of vacuum vessel conditioning (done, for example, upon a regular wall boronization), amount of in-vessel loose material and dust, occurrence of disruptions and run-away electrons that can lead to excessive wall erosion or the level of intentional impurity gas puffing during routine/specialized experiments. The first wall material influences the impurity mixture, too. Tokamaks with in-vessel components covered by tungsten (AUG and JET) are prone to its core accumulation, leading eventually to the core temperature collapse. In COMPASS, the influx of boron has been identified as responsible for core cooling. In DIII-D, similar cases were not recognised.

Preferential discharge settings during experimental campaigns are reflected in the class occurrence as well. In DIII-D, for example, discharge parameters were often set to result in a low value of the edge safety factor, approaching thus the ideal MHD disruptive limit. In combination with the often encountered low plasma density, the disruptions are prone to fall in the category of born-locked modes excited by error fields (reported to be of a relatively high intensity [114]). Low plasma density settings might explain the vulnerability of DIII-D to the modes seeded during the early phase of the discharge too. On the other hand, a relatively high number of (intentional) ideal β limits were identified in this device.

In AUG and JET, plasmas routinely develop the divertor detachment. Occasionally, the detached cold region gets destabilized poloidally, leading to MHD mode growth, as described in Sec. 1.4. This sequence of events is often encountered during the density limits. In contrast, in COMPASS the potential of retrieving detached plasmas has only been explored very recently [115].

Given the fact that most COMPASS discharges from the database are Ohmic, its chances to have disruptions identified within a NBI heating related class naturally decrease. On the other hand, MHD precursors, serving as seeding islands for NTMs, are observed almost routinely in this device, owing to the, in general, large value of the plasma β.

A large relative occurrence of error field born-locked modes has been identified in JET (and DIII-D, see above). Large devices of presumably slow plasma rotation [64] are considered particularly prone to this disruption class. In Ref. [75], on

the other hand, it has been discussed that for COMPASS (small plasma volume of high rotation rate) the excitation of born-locked error field modes is unlikely because of too weak an intrinsic error field. A recent experimental campaign, focused on determination of the COMPASS intrinsic error fields, appears to support these findings.

Other factors, such as the decisions taken by the plasma control system during exceptional events, can influence the disruption class occurrence too. Gas fuelling in the chamber is routinely feedback controlled in real-time. In case of failure of the density control, the plasma can reach a disruptive density limit. The level of technical failures in the particular case of the JET device was studied in Ref. [112] and for a complete picture of the disruption class incidence rate (that is out of the scope of this thesis), this information should be considered as well.

Class code	Code explanation	Relative occurrence COMPASS/AUG/ DIII-D/JET (%)
DL	Density limit, Sec. 2.4	<1/53/15/25
IMP	Radiative collapse due to impurities, Sec. 2.4	8/12/<1/17
NTM	Neoclassical tearing mode, Sec. 2.3.2	67/8/22/5
ACC	In-core impurity accumulation, Sec. 2.4	4/12/0/32
LON	Error-field locked modes, Sec. 2.5.4	<1/2/11/13
RU	Too fast a current ramp-up, Sec. 2.3.1	9/6/22/1
NBIOFF	DL after NBI switch off, Sec. 2.4	2/7/13/5
BLIM	Troyon β limit, Sec. 2.3.1	5/<1/11/0
LOQ	Too low an edge q, Sec. 2.3.1	4/0/5/2

Table 4.3: *Disruption classification: class code, brief code description and relative occurrence of the class in a particular device in %.*

It is noted that the final relative occurrence of cases within RU/FT/RD, ROT/IRLM/BLM and distinct disruption classes is a combination of device-specific physics, engineering and experimental setting constraints (typical of the experimental period of interest) and the database filtering criteria (Sec. 4.2). The relative occurrences presented here are thus not necessarily representative of the device experimental program.

5. Validation of a model for mode braking

5.1 Motivation

Since MHD modes are observed to induce disruptions, their amplitude represents an important quantity to be considered in the disruption prediction schemes. Sec. 2.5.1 reported on that prior to locking, modes can rotate. Given the stabilizing effect of conducting structures on rotating modes (supported by differential rotation of the resonant surfaces), discussed in Sec. 2.5.2, maintaining (or increasing) the mode rotation frequency is a key instrument for disruption avoidance, as highlighted in Sec. 2.5.1. According to the braking model presented in Sec. 2.5.3, losses of the mode angular momentum leading to locking are supposed to be linked to the mode width. Efforts to reduce the radial extent of the mode in real time have involved current drive and heating localized on the rational surface of interest [116–118]. A combination of sustained plasma rotation and reduction of the mode width could therefore be instrumental for disruption avoidance schemes, thus maintaining good plasma confinement, and directing the discharge parameters towards a non-disruptive area of the device operational space. Hence, the expected duration of the locking phase is a key information that should be provided to the plasma control system to determine the settings of the actuators affecting the mode rotation frequency and instability width. In addition, the critical island width for locking can serve as a warning to prepare the plasma control system for a potentially disruptive state. Both quantities should be accessible in real time during the discharge.

In this chapter, it is intended to demonstrate that the locking phase duration and critical island width may be obtained in real time on the basis of the physical model for mode braking introduced in Sec. 2.5.3. As pointed out in Sec. 1.5, it is of interest to *validate* the model for a large set of discharges, thereby considering a broad variety of operational scenarios etc., allowing to explore its limitations. For this purpose, the AUG database of disruptive discharges (the one containing the highest number of initially rotating modes), presented in Sec. 3.2, restricted to cases with an initially rotating mode, was used. This reduced database contains a broad variety of braking dynamics, ranging from fast growing and locking modes to quasi-stable islands braking over long temporal periods. The physical braking model was invoked with the aim to reproduce the experimental braking curves. Both scenarios of momentum transfer at the interface between the mode and the bulk plasma, presented in Sec. 2.5.3, were applied in order to identify the scenario that best explains the experimental observations. In addition, key predictions by the model (braking phase duration and critical mode width for locking) were compared with the experiment and, in the event of a discrepancy, the possible causes were examined.

The contents of next sections are as follows. Sec. 5.2 presents the reduced database of AUG disruptive plasmas. Sec. 5.3 discusses preparation and validation of the experimental input necessary for application of the braking model.

In Sec. 5.4, a critical condition for locking is evaluated both theoretically and experimentally for selected cases. Reconstruction of braking curves is presented and situations where the model breaks down are investigated in detail. Sec. 5.5 contains a discussion of the results, and discusses the model limitations and its potential extensions.

5.2 Reduced database of ASDEX Upgrade disruptive discharges

AUG database entries pertaining to groups ROT and IRLM, defined in Sec. 4.3, are of primary interest in the study presented here, as they are populated by initially rotating modes. To be eligible for further analysis, the input torque from the NBI heating modules had to remain constant during the mode braking phase. The reduced database of initially rotating disruptive modes fulfilling this additional criterion consists of more than 220 entries. Distinct disruption root causes can affect the locking dynamics differently. Therefore, at times the mode braking details will be discussed in the context of the disruption class, affiliated to the database entries in Sec. 4.5.

5.3 Experimental input preparation

An experimental input necessary for the model application was assembled and the following subsections provide additional details concerning the gathered data and presents their validation.

Mode frequency and amplitude

A toroidal array of Mirnov coils located at the AUG outer midplane was used to detect the poloidal component of the mode field $\tilde{B}_\theta$. Spectrograms, with a frequency resolution $\Delta f = 0.4$ kHz and temporal resolution $\Delta t = 2.5$ ms, allowed to track the experimental mode frequency ω and amplitude. The initial rotational frequency ω_0 was defined as the maximum of the tracked frequency preceding the mode deceleration. In the example of a spectrogram shown in Fig. 5.2a, the mode braking is initiated at $t = 3.652$ s and the mode initial frequency is $\omega_0/2\pi = 14.8$ kHz. The experimental time point of the mode braking initiation is commonly denoted as t_{slow}.

Mode structure

Following the analysis of the mode structure in terms of the m and n numbers, described in Sec. 3.1.1, it was found that about 50% of the initially rotating modes were of $(m/n)_{\mathrm{ini}} = 3/1$ structure, followed by $\approx 42\%$ $(m/n)_{\mathrm{ini}} = 2/1$ and $\approx 6\%$ $(m/n)_{\mathrm{ini}} = 4/1$ modes. Other mode structures ($(m/n)_{\mathrm{ini}} = 3/2, 5/1$) were present in less than 2% of the cases.

In Sec. 2.5.1, it was stated that within the two-fluid plasma description, the mode frequency can be expressed as a sum of the bulk plasma and the electron diamagnetic drift velocities. In Fig. 5.1 the sign of the mode rotation is shown

in the context of the discharge specific heating scheme and the l_i/q_{95} calculated at $t = t_{slow}$. The latter distinguishes only two scenarios, either the NBI modules were used ('NBI-heated') or not ('no NBI') prior to t_{slow}. Two observations can be inferred from the plot. Firstly, counter-clockwise (as seen from the top view of the vacuum vessel) toroidal direction of rotation is labelled with a "+" sign and the plasmas heated with the tangential NBI modules typically rotate in this direction due to their dominant momentum input. Modes tend to systematically co-rotate with the plasma bulk and adopt the same sign. In case of no torque injection from the NBI modules, the mode direction of rotation depends on the specific discharge parameters, such as the pressure and density gradients [61, 119] and in Fig. 5.1 the corresponding data points are evenly distributed in both positive and negative point clusters. Secondly, in case of more peaked current profiles, modes of lower poloidal mode number are driven unstable. This trend is emphasized by the green arrows (note that $l_i > 0$ and $q_{95} < 0$ for none reversed B_t discharges). This observation is in line with the theory of stability of tearing modes, discussed in Sec. 2.3.2 and the references cited therein, in particular with the theoretical statement that with increasing current profile peaking, modes from higher to lower m number progressively stabilize.

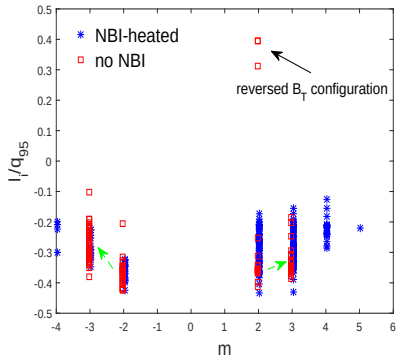

Figure 5.1: *Signs of mode rotation displayed in the context of the discharge associated heating scheme.*

MHD equilibrium reconstruction

For the modes locking during the flat-top phase (67%) of the discharge, a constraint on the central value of the safety factor was set, $q_0 = 1$, in correspondence with the typical current redistribution during this discharge phase. The resulting equilibrium profiles, calculated by the CLISTE code, are expected to be more realistic compared to the standard reconstructed profiles without constraints on q_0. It is noted that about 7% of the locking modes occurred in the current ramp-up phase and 26% during ramp-down.

The position of the rational surface of interest was compared with ECE measurements for a selected discharge #32505 experiencing a braking 2/1 mode, shown in Fig. 5.2. The equilibrium reconstruction yielded the minor radius of the

$q = 2$ surface, further converted to the $\{R, z\}$ coordinates, $R_s(q = 2)$. The location of the phase jump and the minimum of the FFT amplitude (recall Sec. 3.1.3) along the major radial coordinate was compared with $R_s(q = 2)$ and a reasonable agreement between the quantities was found, see Fig. 5.2b.

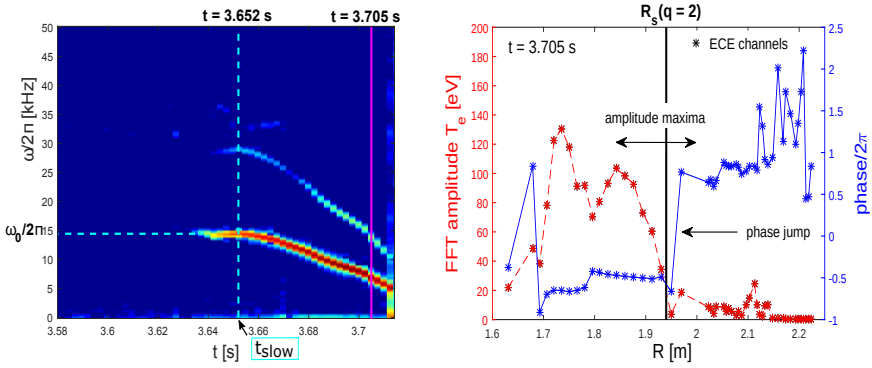

(a) (b)

Figure 5.2: *AUG discharge #32505 (a) Example of a spectrogram allowing to track mode frequency and amplitude ($m/n = 2/1$). The mode decceleration is initiated at $t = t_{\mathrm{slow}} = 3.652$ s. (b) Fourier amplitude and phase of ECE data acquired at $t = 3.705$ s. $R_s(q = 2)$ is in reasonable accordance with the position of the π jump in the phase and local minimum of the amplitude.*

Resistive wall time

For the AUG vacuum vessel, Eq. (2.59) yields the theoretical value $\tau_{\mathrm{w,th}} = 25$ ms ($\sigma_{\mathrm{w}} = 1/\eta_{\mathrm{w}} = 10^7\ (\Omega m)^{-1}$, $r_{\mathrm{w}} \approx 0.8$ m, $b \approx 0.005$ m). Since this parameter is fundamental for the model application, an experimental technique to determine it was used as well. In particular, the frequency-dependent attenuation of the mode field due to the vacuum vessel wall was calculated using Eq. (2.67). This evaluation was based on measurements by magnetic sensors located on both sides of the wall, at the same toroidal angle and approximately the same poloidal angle (coils Bp2i01 and Bp2a01). The displacement of the coils along the poloidal coordinate was $\Delta\theta = 0.0314$ rad. The sensors are located at the low-field side, midplane. Data averaged over five discharges with a single 2/1 mode were used to experimentally determine the ratio. The data were fitted to Eq. (2.67) (see Fig. 5.3a) and the best fit was obtained for $\tau_{\mathrm{w,att}} \approx 0.82$ ms. Similarly, the phase difference between the signals acquired with the same pair of coils was measured and fitted with the corresponding analytical expression. Apart from τ_{w}, a phase shift $\Delta\varphi$ was added as a free fit parameter, since the integrated signals from the coils could be phase-shifted due to the hardware integration through the raw signal processing. Furthermore, the displacement of the coils along the poloidal coordinate $\Delta\theta$ was considered. The best fit yielded $\tau_{\mathrm{w,phase}} \approx 0.64$ ms (see Fig. 5.3b).

The construction of a frequency-dependent function of the field attenuation and phase shift associated with single locking modes can be considered as a conve-

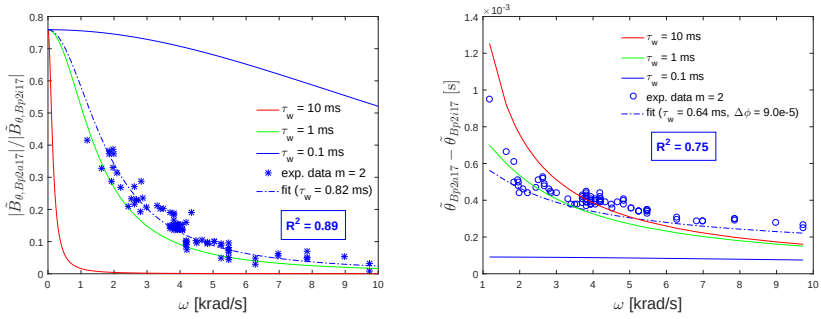

(a) (b)

Figure 5.3: *(a) Attenuation of the absolute value of the poloidal component of the mode field, after passing through the vessel wall. Solid lines show examples of theoretical curves, calculated with Eq.* (2.67) *for various* τ_w *(*$m = 2$*), considering the actual geometrical configuration of the coils. The best fit of the analytical formula to the experimental data yielded* $\tau_{w,att} \approx 0.82$ *ms. (b) The fit of the phase shift between the mode field components yielded* $\tau_{w,phase} \approx 0.64$ *ms (*$m = 2$*).*

nient approach to deduce properties of a single conducting structure of interest in which helical mirror currents are driven. An average value $\bar{\tau}_w = 0.73$ ms of $\tau_{w,att}$ and $\tau_{w,phase}$ was thus used in applications of the mode locking model. This value is clearly different from $\tau_{w,th} = 25$ ms, admittedly calculated under the highly idealized assumption of a cylindrical shell of constant thickness.

Island width

The width of magnetic islands was estimated from magnetic sensor data, measuring the poloidal component $\tilde{B}_\theta$ of the perturbation magnetic field, as well as the magnetic equilibrium, using Eq. (2.24). Eq. (2.64) (specifically Eq. (2.66)) was used to calculate the radial component $\tilde{B}_r(r_s)$ of the magnetic field at the rational surface, from the data of the poloidal component $\tilde{B}_\theta(r_c)$ measured at the coil position r_c. As a cross-check, the island width obtained from the magnetic measurements (w_{mag}) was compared with the ECE data contour plot (w_{ECE}) for a selected discharge #32505 experiencing a large mode (see Fig. 5.4). Estimation of w_{ECE} suffers from uncertainties due to imperfect flattening of the temperature within the island region. It should thus be considered as an upper limit of the experimental mode width. It was found that w_{mag}, corrected for the effect of toroidicity $w_{mag,tor}$ (see Eq. (2.54)), was in good agreement with w_{ECE}.

Momentum confinement time

In case of auxiliary heated AUG discharges, the experimental input needed for the calculation of τ_{M0} was obtained with individual runs of the TRANSP code [120]. Out of the ROT and IRLM cases, only 139 discharges could be processed with TRANSP due to occasional absence of experimental data. The calculated τ_{M0} was compared to τ_{E0}, both estimated at the same temporal point in the instability-free part of the discharge preceding the onset of mode locking. The mean of the

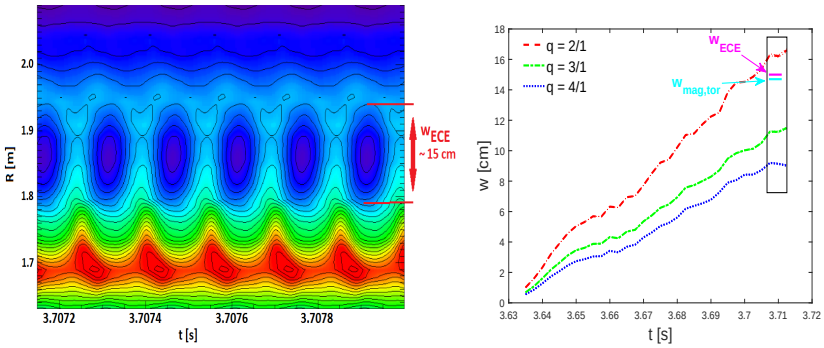

(a) (b)

Figure 5.4: *AUG discharge #32505 (a) ECE data contour plot data showing a region of flat temperature associated with a resistive mode. Island separatrix can be recognised and the island width is estimated to* $w_{ECE} \sim 15$ *cm at* $t \sim 3.7079$ *s. (b) Time traces of island widths of modes of distinct structure* $(m/n = 2/1 - 4/1)$ *calculated with Eq.* (2.24) *and Eq.* (2.66)*. The measured poloidal component of perturbation magnetic field* $\tilde{B}_\theta$ *was supplied to the formulae. Mode structure was identified to* $2/1$*, red dashed line is thus of interest. At* $t = 3.708$ *s,* $w_{\mathrm{mag}} \sim 16.3$ *cm,* $w_{\mathrm{mag}} \sim 15$ *cm and* $w_{\mathrm{mag,tor}} \sim 14.7$ *cm.*

$\tau_{\mathrm{M0}}/\tau_{\mathrm{E0}}$ was calculated to 1.09 ± 0.57. Therefore, in case of absence of experimental data necessary to calculate τ_{M0}, a value of $1.09\,\tau_{\mathrm{E0}}$ was used. During transient phases of the discharge, the confinement times should take into account the temporal derivative of the plasma energy or angular momentum, i.e.

$$\tau_{\mathrm{E0}} = \frac{W_{\mathrm{th}}}{P_{\mathrm{tot}} - \frac{\mathrm{d}W_{\mathrm{th}}}{\mathrm{d}t}}, \tag{5.1}$$

with P_{tot} the total power input and W_{th} the plasma thermal energy, and

$$\tau_{\mathrm{M0}} = \frac{L_\phi}{T_{\mathrm{IN}} - \frac{\mathrm{d}L_\phi}{\mathrm{d}t}}. \tag{5.2}$$

These expressions will be referred to as 'dynamic' confinement times. However, $\mathrm{d}L_\phi/\mathrm{d}t$ could not always be evaluated due to signal discontinuities. In that case the 'static' $\tau_{\mathrm{M0}} = L_\phi/T_{\mathrm{IN}}$ was used. A comparison of calculated dynamic and stationary τ_{M} can be found in Figs. 5.6b,5.8b. It can be seen that during the transient discharge phase, τ_{M}(dynamic)$\sim$ (0.5-0.9)τ_{M}(static). Furthermore, it is noted that the temporal evolution of τ_{M} and τ_{E} can differ substantially during discharge transient phases.

Plasma density

The electron density n_{e} at the rational surface of interest was calculated from TS measurements. If those were unavailable, or if there were less than two TS data points during the mode duration, data from a DCN interferometer were used instead, which views the plasma region along a line-of-sight at a normalized radius

$r/a \approx 0.8$. In case the interferometer data were suffering from fringe jumps, the density was calculated during the previous available time point without fringe jumps. It is noted that in most cases this point was separated from the locked mode onset time by a short temporal interval, it is thus reflecting the plasma density conditions in the particular line-of-sight plasma shortly before the onset of the transient discharge period.

Parameter ranges at locking onset

The experimental AUG period 2012–2016 covers a broad range of operation conditions and plasma parameters (recall Tab. 4.2). In addition, the temporal evolution of the growth of the instability for the ROT and IRLM database entries can be very different from case to case. There are instabilities that grow explosively and lock immediately (Fig. 5.5, left), others are of a quasi-stable nature (Fig. 5.5, right), etc. Tab. 5.1 shows the extent of the parameter space in which the mode locking model was applied. The table contains various plasma parameters, either not shown in Tab. 4.2 or differing from the values presented there by more than 10%. The range across the database is again presented in the format median($x(t = t_{\mathrm{ref}})$) $\pm$ MAD, this time with $t_{\mathrm{ref}} = t_{\mathrm{slow}}$. Confinement times were deduced shortly before the mode onset and γ was obtained by fitting the analytical mode growth formula Eq. (2.77) to the experimental data. In multiple cases, γ was observed to vary during the period of mode rotation.

The mode rotation phase duration Δt_{ROT} has a particularly broad and skewed distribution in the database, with a median of 21 ms and an average of 135 ms. Often, rotating modes exhibited a quasi-stationary phase during their existence. Tab. 5.2 presents Δt_{ROT} for the various disruption classes. The shortest rotating mode durations are associated with the modes driven unstable at high plasma density, while the longest modes tend to be NTMs. On the other hand, maximum *locking* phase durations were of the order of tens of milliseconds. Modes decelerating during the plasma flat-top phase had the longest locking durations (with an average value of 33 ms and median 10 ms). The distribution of the locking durations in the ramp-down phase was narrow, peaking at ≈ 10 ms. The ramp-down phase typically shows a strong variation of plasma parameters, particularly in case of an emergency ramp-down initiated by the plasma control system. Fast current density redistribution (supported, for example, by development of a cold plasma edge) might accelerate mode locking and pose a rather strict upper limit to the locking phase duration. The DL database entries were mostly of $\omega_0/2\pi < 4$ kHz. Modes of higher $\omega_0/2\pi$ belonged mainly to the ACC and NTM categories. The parameter f_{M} in Eq. (2.72), accounting for the degradation of the momentum confinement, was not determined, as this would require modelling the momentum diffusion during the mode growth.

The model for mode locking used in this work was derived for cylindrical plasmas. However, modes within the database typically lock in a diverted plasma configuration. The actual mass undergoing braking is thus underestimated if the plasma minor radius given by CLISTE is used in the mode equation of motion. To compensate partially this effect, an effective minor radius a_{eff} was used, obtained by forcing the plasma shaping factor $S = q_{95}/q_{\mathrm{cyl}} = 1$ ($q_{cyl} = 2\pi a^2 B_{\mathrm{t}}/R_0 I_{\mathrm{p}}$) [121],

W_{th} (MJ)	H98	τ_{E0} (ms)	τ_{M0} (ms)
0.11 ± 0.06	0.56 ± 0.22	57 ± 18	53 ± 19
$n_{\mathrm{e}}(r_{\mathrm{s}})$ ($\times 10^{19}$ m^{-3})	l_{i}	I_{p} (MA)	$B_\theta(r_{\mathrm{s}})$ (T)
6.11 ± 2.12	1.40 ± 0.15	0.78 ± 0.11	0.36 ± 0.03
T_{NBI} (Nm)	$\omega_0/2\pi\|_{2/1}$ (kHz)	$\omega_0/2\pi\|_{3/1}$ (kHz)	r_{w}/a
3.92 ± 1.76	2.4 ± 0.8	2.0 ± 0.8	1.8 ± 0.0
$r_{\mathrm{s}}/a\|_{2/1}$ (LFS)	$r_{\mathrm{s}}/a\|_{3/1}$ (LFS)	$1/\gamma$ (ms)	Δt_{ROT} (ms)
0.72 ± 0.10	0.91 ± 0.04	33 ± 32	21 ± 16

Table 5.1: *Ranges of various plasma parameters presented in the format median($x(t = t_{\mathrm{ref}})$) ± MAD ($t_{\mathrm{ref}} = t_{\mathrm{slow}}$).*

Disruption class	DL	IMP	NTM	ACC	RU	NBIOFF
Mean	13	13	99	69	63	13
Median	93	45	460	113	111	59

Table 5.2: *Mean and median of Δt_{ROT} (ms) within the distinct disruption classes. LON and BLIM class entries are not included in the reduced AUG database.*

yielding

$$a_{\mathrm{eff}} = \sqrt{\frac{q_{95} R_0 I_{\mathrm{p}}}{5 B_{\mathrm{t}}}}. \tag{5.3}$$

This leads to a better representation of the braking mass in shaped plasmas. As $a < a_{\mathrm{eff}}$, the aspect ratio reduces and consequently the neoclassical transport effects would be artificially amplified, but this is not considered in the model for mode deceleration employed here.

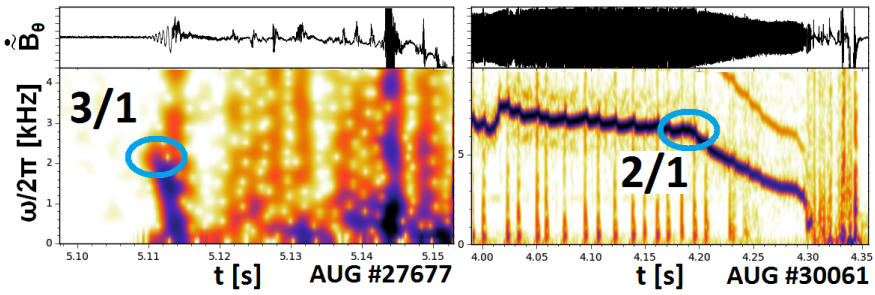

Figure 5.5: *Examples of IRLM database entries: immediately locking radiation-driven mode near the density limit (left), quasi-stable NTM (right). Points marking the initiation of the mode deceleration are encircled.*

m	2	3	4
$\omega_{0,\min}/2\pi$ (kHz)	2.23	3.35	4.47
$\omega_0/2\pi > \omega_{0,\min}/2\pi$	59%	20%	–

Table 5.3: $\omega_{0,\min}/2\pi$ *calculated for different poloidal mode numbers. The last row shows the number of locking modes for which the condition for mode bifurcation is fulfilled.*

5.4 Application of the mode locking model

5.4.1 Theoretical evaluation of the locking bifurcation condition

In applying the mode locking model outlined in Sec. 2.5.3 to the modes observed in the AUG reduced database, the condition Eq. (2.107) for the locking bifurcation was first investigated. Tab. 5.3 lists the minimum $\omega_{0,\min}/2\pi$ for which this condition was satisfied. About 59% of the $m = 2$ locking modes and 20% of the $m = 3$ modes had an initial rotational frequency exceeding $\omega_{0,\min}$, thus exhibiting a locking bifurcation. For the remaining cases—a substantial fraction—the point of locking bifurcation, i.e. the critical mode width for locking (Eq. (2.97) and Eq. (2.98)), was not defined. Within the scope of the model, these modes should thus decay continuously in frequency. In the absence of an estimate of the critical mode width where the locking bifurcation takes place, the definition of the dynamic critical mode width breaks down. This will become important in Sec. 5.4.3.

Then, the minimum w/a for the existence of real solutions of the stationary form of Eq. (2.79) was evaluated for all concerned discharges. On average, the condition given by Eq. (2.85) was satisfied when $w/a \geq 11\%$.

5.4.2 Reconstruction of experimental braking curves

Next, the reconstruction of experimental braking curves for the discharges in the AUG reduced database, by solving the mode equation of motion Eq. (2.79) numerically, is discussed. Both the cases of plasma bulk breaking ('co') and island deceleration ('de') were considered as those represent the extreme braking scenarios. The temporal variation of the input parameters was taken into account, with the factor A_{co} (see Eq. (2.75)) or A_{de} (see Eq. (2.76)) being time-dependent. τ_{M} was obtained by integration of the concerned parameters over the full plasma radius. The experimentally obtained island widths $w/a(t)$ were smoothed and fitted with an analytical function of the form of Eq. (2.77). In a number of cases, the best fit yielded $\eta < 1$. The fitted function was used to extrapolate $w/a(t)$ to a point of complete mode locking. In case of multiple (coupled) modes decelerating simultaneously, the mode with the strongest field was selected for reconstruction of the braking curve.

Out of the about 220 plasmas with initially rotating modes that were suitable for further analysis using the mode locking model, the braking curve could be integrated for 103 discharges. For the other cases, there were various reasons why $w/a(t)$ could not be fitted by Eq. (2.77), e.g. because a minor disruption took place

during the deceleration phase, or due to a wildly fluctuating temporal evolution, or because the fit was of insufficient quality (the coefficient of determination, R^2, was $\lesssim 0.8$).

In a number of discharges, the calculated amount of decelerating torque was not sufficient to reproduce experimental braking curves (a similar observation was reported in [122]). In such cases, the mode locking model used here allows matching experimental and theoretical curves by increasing the parameter f_M in Eq. (2.72), i.e. allowing for large plasma momentum losses due to the mode itself. The value of f_M has to lead to a rough match between the experimental momentum confinement time in the locked state and that predicted by Eq. (2.72). Alternatively, the experimentally observed mode width may be increased with a factor f_w, yielding a modified mode equation of motion:

$$\frac{\mathrm{d}\omega}{\mathrm{d}t} = \frac{\omega_0}{\tau_{\mathrm{M}0}} - \frac{\omega(1 + f_\mathrm{w} f_\mathrm{M} w/a)}{\tau_{\mathrm{M}0}} - A\left[f_\mathrm{w}\frac{w}{a}(t)\right]^4 \frac{\omega\tau_\mathrm{w}}{(\omega\tau_\mathrm{w})^2 + m^2}. \tag{5.4}$$

It is noted that in the wall force term (last term on the right-hand side) the multiplication factor makes an important contribution, with a factor f_w^4. This effect is dominant with respect to the influence of f_w on decreasing the plasma momentum confinement (second term on the right-hand side). While setting $f_\mathrm{M} \gg 1$ may correspond to a physically plausible scenario, using a factor $f_\mathrm{w} > 1$ for the island width is a more artificial intervention. On the other hand, the value of f_w, which turns out to be discharge-specific, does provide information concerning the amount of missing torque due to the mode-wall interaction.

Cases with $f_\mathrm{M} > 0$, $f_\mathrm{w} = 1$

Assuming first that $f_\mathrm{w} = 1$ and by varying $f_\mathrm{M} > 0$ to match the experimentally observed momentum confinement, good agreement was obtained between the numerical solution of the equation of motion and the experimental braking curve for 15 of the 103 initially rotating modes. An example of such a case is shown in Fig. 5.6 for AUG discharge #30838, during which high-Z material accumulated in the core, leading to enhanced radiation from this plasma region. Strong MHD activity was observed and the 2/1 mode of interest appeared at $t \approx 3.52$ s (denoted by 'mode ini' in the plots). At that point the momentum confinement was relatively high ($\tau_{\mathrm{M}0} \approx 120$ ms) and for the first tens of milliseconds after its onset, the mode remained in a quasi-stationary state. Mode braking initiated at $t \approx 3.56$ s ('lock ini') and ended at $t \approx 3.66$ s, although the mode continued to rotate at low frequency.

Plasma rotational profiles reveal that the mode was located within a region of high rotational shear. Indeed, Fig. 5.6c points out that deceleration started with the island, reaching the plasma centre only at a later time. The dynamic τ_M suggests that the plasma angular momentum content started to drop shortly before the mode onset (the input torque density, not shown, was roughly uniformly distributed during the mode duration). This may have been caused by an MHD mode that appeared shortly before the examined 2/1 locking mode. This MHD mode was recognisable in the spectrogram during the temporal interval $t \approx 3.487$–3.507 s, with a decaying amplitude and braking from $\omega_0/2\pi \approx 5.6$ kHz to 4.8 kHz before it disappeared. Growth of the 2/1 mode of interest initially occurred in a nonlinear fashion, reaching a saturated width of $w/a \approx 17\%$ at $t = 3.575$ s. After

that, the mode started to grow exponentially. In both phases of the mode growth, Eq. (2.77) was fitted to the experimental curve, separately to the two growth segments. The final data vector representing the mode width temporal evolution, considered for the numerical integration of the mode equation of motion, was thus composed of the two mode growth phases along the distinct temporal intervals.

As the mode grew towards saturation, τ_{M} was first affected only mildly, but then started to decrease noticeably during the phase of exponential mode growth (Fig. 5.6d, rightmost arrow). f_{M} was set to a non-zero value only at the start of the braking phase, accounting for the influence of the mode on the rate of momentum redistribution. Initially, the $q = 2$ surface was located at $r_{\mathrm{s}}/a \approx 0.82$, shifting to $r_{\mathrm{s}}/a \approx 0.75$ by the end of the locking phase, i.e. a change of about 10%. In Ref. [71], a dependence of f_{M} on r_{s}/a was suggested, but f_{M} was kept constant for the numerical solution.

Fig. 5.6a displays the experimental and reconstructed braking curves. An agreement between the two curves for the case of full plasma column braking was obtained when $f_{\mathrm{M}} = 17$. For the decoupled island braking, setting $f_{\mathrm{M}} = 9$ resulted in the agreement with the experiment. At the end of the locking phase, w/a had grown to about 36%, which can be substituted in Eq. (2.72) to predict the decrease of τ_{M}. Using the dynamic formula for the experimental confinement time τ_{M}, a decrease from about 90 to 10 ms was observed (initial data point read at the mode onset, see Fig. 5.6b). In case of the static τ_M, the decrease happens from 120 ms to ≈ 12 ms. Those final values of $\approx 10 - 12$ ms are in reasonable agreement with that predicted by Eq. (2.72) for $f_{\mathrm{M}} = 17$ (≈ 17 ms). For $f_{\mathrm{M}} = 9$, the predicted drop in τ_{M} (≈ 28 ms) overestimates the experimental situation.

For the other 14 cases for which the experimental braking curve could be reconstructed with $f_{\mathrm{w}} = 1$, $f_{\mathrm{M}} > 0$, the manually obtained value of the parameter f_{M} was found to lie between 1 and 18, decreasing the momentum confinement time by a factor of $\lesssim 6$ at locking. In Fig. 5.7, the parameter f_{M} is plotted against the discharge-specific ratio $\tau_{\mathrm{M0}}/t_{\mathrm{lock}}$. The general rising trend is in accordance with physical arguments that were already mentioned, i.e. that correction of the momentum confinement losses due to the mode becomes increasingly critical as the ratio of momentum redistribution time to locking time rises. As a rule of thumb, the model is able to reproduce the experimental braking curve, such that $\omega_{\mathrm{exp}}(t) \approx \omega_{\mathrm{int}}(t)$ during the entire braking phase, when $\tau_{\mathrm{M0}}/t_{\mathrm{lock}} \lesssim 2$.

Cases with $f_{\mathrm{M}} \gg 0$ or $f_{\mathrm{w}} > 1$

Next, the focus is posed on plasmas where it was not possible to adjust f_{M} such that both the numerically integrated braking curve and the predicted drop in τ_{M} agreed with the experiment. This observation is reported in 88 out of the 103 cases. Furthermore, in $\sim 35\%$ of the 103 tested cases, the discrepancy between the experimental and predicted locking duration for both 'co' and 'de' scenarios was overestimated by a factor of $1.3-2$. The missing braking torque was compensated by setting either $f_{\mathrm{w}} > 1$ or $f_{\mathrm{M}} \gg 1$ (or a combination of both, see below). An example of one of those cases is examined in the following.

In Fig. 5.8 an initially rotating mode occurring during the AUG discharge #28227 is shown. The discharge details are inspected to examine the potential source of the above mentioned discrepancy. The disruption took place due to a locked mode that appeared as a consequence of high density and an impurity

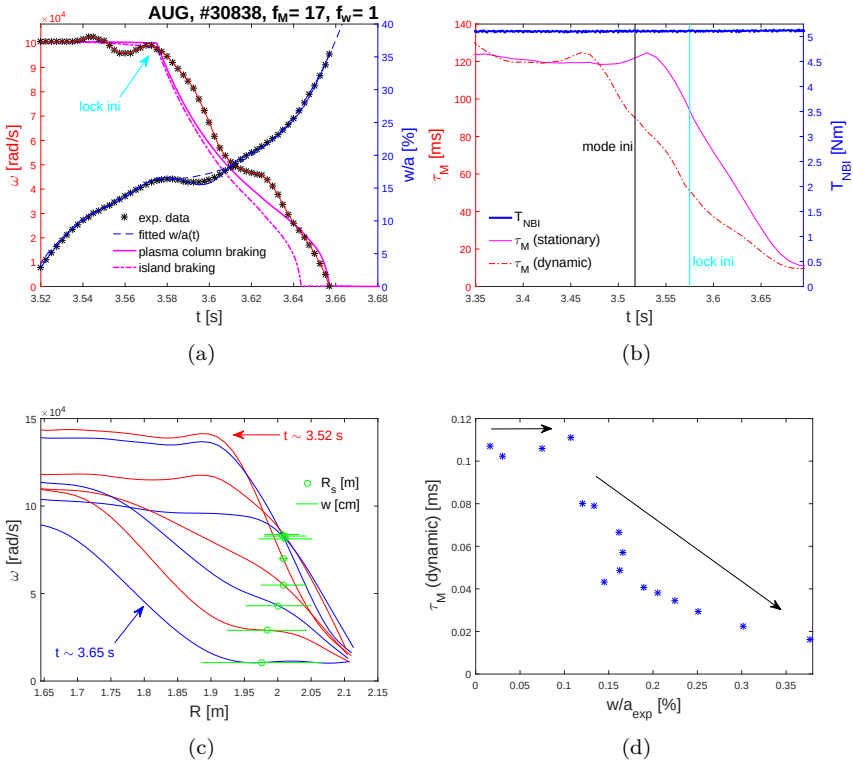

Figure 5.6: *NBI-heated discharge #30838 with a 2/1 mode. (a) Comparison of experimental and reconstructed braking curves, both braking curves were obtained by setting* $f_{\mathrm{M}} = 17$. *In case of the 'de' scenario this leads to underestimation of the experimental braking duration. Setting* $f_{\mathrm{M}} = 9$ *results in matching of the 'de' scenario braking curve to the experimental data points, but the 'co' scenario overestimates the locking phase duration. Note that only the 'fitted w/a(t)' and the associated data points (visualized by black stars and bold blue line) were plotted w.r.t the right vertical axis. (b) Temporal evolution of* T_{NBI} *and* τ_{M}. *(c) Temporal evolution of rotation profiles. (d) Evolution of the dynamic* τ_{M} *during the mode growth.*

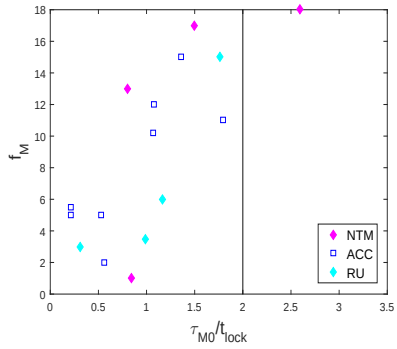

Figure 5.7: *Parameter f_{M} vs. the discharge-specific ratio $\tau_{\mathrm{M0}}/t_{lock}$. As a rule of thumb, the mode locking model can reproduce the experimental braking curves when $\tau_{\mathrm{M0}}/t_{lock} \lesssim 2$. Only the disruption classes NTM, ACC, and RU are present in the plot.*

influx, according to a scenario similar to the H-mode density limit presented in Ref. [123]. More specifically, the discharge entered a transient period at around 6 s. At this time, the Greenwald fraction reached $n_{\mathrm{e}}/n_{\mathrm{GW}} \approx 0.96$ and l_{i} started to gradually increase, while the thermal stored energy W_{th} started to decrease. Slightly later, an NBI source tripped briefly (see the dip in the corresponding time trace in Fig. 5.8b at $t \approx 6.05$ s), which could have led to a redistribution of the torque input density. Due to divertor detachment, a region of cold plasma, presumably a MARFE, developed early in the transient phase. This cold plasma region started to shift poloidally at around 6.105 s. At the same time, the equilibrium reconstruction suggests that the plasma separatrix moved slightly towards the torus inner wall, which may have led to the material erosion (the measured tungsten concentration in the plasma has risen). A cold dense region is recognized to shortly stabilize close to the midplane at the inner part of the torus. In addition, the plasma appears to have briefly entered and left the H-mode during the transient period, the second time at $t \approx 6.112$ s. A 'cold edge', featuring highly peaked current density profiles, developed progressively, driving a 3/1 mode unstable at $t \approx 6.145$ s, which started to decelerate immediately. The mode was located at a normalized radius $r_{\mathrm{s}}/a \approx 0.91$ and it grew within 7 ms from $w/a \approx 3\%$ to $w/a \approx 14\%$. Rotation profiles (not shown) reveal a large and fast variation of the central plasma rotation. Changes were also observable in T_{e} and T_{i}, with the latter gradually decreasing and the former increasing. The initially rotating mode was followed by a rise of the locked mode signal (Fig. 5.8d). It is thus probable that the toroidal rotation of the plasma column changed rapidly, at least in the vicinity of the rational surface. Note that in this particular case, the line-integrated plasma density was retrieved from the DCN interferometer data. These suffered from a fringe jump at $t \approx 6.108$ s, presumably due to displacement of the cold region. This was the last temporal point at which the density was calculated, therefore the plasma density was kept constant at this value in the numerical integration of the braking curve. However, Fig. 5.8a clearly shows that, for $f_{\mathrm{M}} = 0$ and $f_{\mathrm{w}} = 1$, the integrated curves in both the 'co' and 'de' scenarios do not correspond to the

experimental curve. In particular, the integrated mode frequency is overestimated with respect to the experiment after the braking initiation ($\omega_{\rm exp} \ll \omega_{\rm int}$).

In Fig. 5.8c, $f_{\rm M} \gg 0$, or $f_{\rm w} \gg 1$, or a combination of both was adopted in the attempt of the braking curve reconstruction. Only the 'co' scenario is shown here, first for $f_{\rm w} = 1$ and $f_{\rm M} \gg 1$. The value $f_{\rm M} = 110$ yielded the best approximation to the data points, but failed to reproduce the frequency decay to a locked state that was observed experimentally, instead showing asymptotic behaviour. These settings of $f_{\rm M}$ and $f_{\rm w}$ predict a decay of $\tau_{\rm M}$ from 17 ms ($\approx \tau_{\rm M0}$) to ≈ 1 ms, i.e. decreasing $\tau_{\rm M0}$ by about a factor of 20. However, experimental data suggest that the momentum confinement time at the end of the transient phase was about 11 ms. It should be noted that the calculation of $\tau_{\rm M}$ relies on the knowledge of the rotation profiles, whereas in case of this discharge the $\omega(r)$ profiles could suffer from considerable uncertainties during the transient phase. In a next attempt, the values $f_{\rm w} = 3.0$ and $f_{\rm M} = 0$ were chosen. In this case, the reconstructed braking curve decays to locking at the experimentally observed time, but the details of the experimental braking curves are not captured, with $\omega_{\rm exp} \ll \omega_{\rm int}$. Finally, for $f_{\rm w} = 2.5$ and $f_{\rm M} = 35$ a satisfactory braking curve was obtained. However, with these settings the predicted final momentum confinement time is $\tau_{\rm M} \approx 2$ ms, i.e. about a factor 9 smaller than $\tau_{\rm M0}$, significantly underestimating the experimental value. It is therefore concluded that with this combination of $f_{\rm w} > 1$ and $f_{\rm M} \gg 1$, the momentum losses of the plasma column are not dominated by the braking mode within the scope of the model. This is discussed in more detail in Sec. 5.5.

Relation of $t_{\rm lock}$ and $f_{\rm w}$ with plasma parameters and disruption classes

For all 103 initially rotating modes, braking curves were reconstructed such as to match the experimentally observed duration $t_{\rm lock}$ of the locking phase with that obtained from the integrated braking curve. In case this match could not be achieved using $f_{\rm M} > 0$ and $f_{\rm w} = 1$, with the additional requirement of consistency with the experimental confinement time at the locking, also $f_{\rm w} > 1$ was applied. Analysis of the 103 discharges yielded average values $\bar{f}_{\rm w,co} = 1.5$ (median 1.2) and $\bar{f}_{\rm w,de} = 1.2$ (median 1.0). In the following, the focus is set on the 'co' scenario, involving plasma column braking.

To further examine the potential dependence of the experimental locking duration on the plasma parameters, the Pearson correlation across the *full set* of 103 discharges was calculated between $t_{\rm lock}$ and various parameters x at braking initiation. The correlation between $t_{\rm lock}$ and the total change Δx of x over the entire period of braking was determined as well. In the following, it is referred to the absolute value of the correlation.

A strong correlation was found between $t_{\rm lock}$ and the change in the pressure-dependent parameters ($\Delta\beta_{\rm p}$, $\Delta W_{\rm th}$). In most cases $\beta_{\rm p}$ decreased during the braking phase ($\Delta\beta_{\rm p} < 0$), which might be mainly associated with a decrease in the plasma kinetic pressure. This could be due to a drop in the plasma temperature, potentially caused by the mode and localized plasma cooling. In turn, this may influence the mode velocity through the electron diamagnetic drift, given by Eq. (2.30) (its variant for electrons). On the other hand, in case of the NBI heated discharges, the mode rotation can be dominated by the ion bulk rotation, suppressing thus the relative importance of $v_{\rm e,dia}$. It is reported that $t_{\rm lock}$ correlated

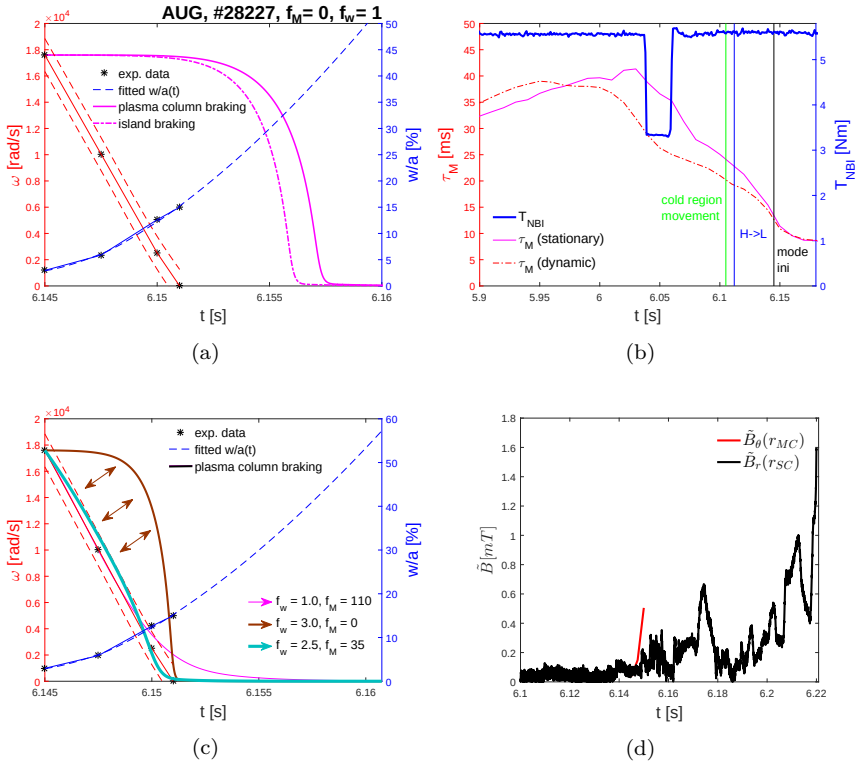

Figure 5.8: *NBI-heated discharge* #28227 *with a 3/1 mode. (a) Comparison of experimental and reconstructed braking curves. (b) Temporal evolution of* T_{NBI} *and* τ_{M}*. (c) Attempts to reconstruct the experimental braking curve by setting* $f_{\mathrm{M}} \gg 1$ *and/or* $f_{\mathrm{w}} > 1$*. Only a combined adjustment of both factors allows to reproduce the experimental braking curve. (d) The locked mode field amplitude* $\tilde{B}_r(r_{\mathrm{SC}})$ *(black bold line, measured at the saddle coil location* r_{SC}*) rises above the noise level at* $t \approx 6.149$ *s. The rotating mode amplitude* $\tilde{B}_\theta(r_{\mathrm{MC}})$ *starts to rise shortly before (red bold line, measured at the Mirnov coil location* r_{MC}*).*

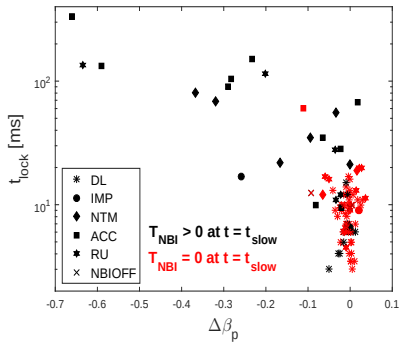

Figure 5.9: *Experimental locking duration* t_{lock} *plotted against the variation in* β_{p} *occurring during the mode braking. Color coding separates* $T_{\mathrm{NBI}} > 0$ *and* $T_{\mathrm{NBI}} = 0$ *(both calculated at* $t = t_{\mathrm{slow}}$*) cases.*

positively with T_{NBI} and also with ω_0. This observation is in accordance with the fact that the external torque input acts as a source of plasma rotation, which can be reflected in higher mode initial rotational frequency and can lead to extended braking phase duration. Fig. 5.9 displays t_{lock} in the context of $\Delta\beta_{\mathrm{p}}$ and resolves the cases with NBI torque input and without it at $t = t_{\mathrm{slow}}$. The plot area can be virtually divided along $\Delta\beta_{\mathrm{p}} = -0.05$. The strong correlation between t_{lock} and $\Delta\beta_{\mathrm{p}}$ is preserved for cases with $\Delta\beta_{\mathrm{p}} < -0.05$. Those cases are typically of long braking phase durations and with $T_{\mathrm{NBI}} > 0$ at $t = t_{\mathrm{slow}}$. The mode rotation can be thus dominated by the external torque input there, giving the electron diamagnetic drift mode velocity component a minor relative importance. The reason for the strong correlation between t_{lock} and $\Delta\beta_{\mathrm{p}}$ can thus not be traced back to an effect of $v_{\mathrm{e,dia}}$ alone.

It is noted that only a weak correlation was observed between t_{lock} and the change of pressure-dependent parameters *preceding* the locking phase (the temporal interval of interest was set 200 ms prior to the mode braking until the locking initiation). This suggests that the rate of mode momentum loss is mainly related to the variation of the plasma parameters *during* the mode locking. A moderate correlation between t_{lock} and Δl_{i}, Δq_{95} and $\Delta l_{\mathrm{i}}/q_{95}$ was observed. The first two parameters determine the q-profile, thus indirectly affecting the position of the resonant surface r_{s}. As mentioned before, the ratio l_{i}/q_{95} is related with the free energy available for growth of the mode. In turn, this may influence the mode growth rate, which is strongly correlated with t_{lock}.

As in the case of t_{lock}, $\Delta\beta_{\mathrm{p}}$ and ΔW_{th} appear to be linked to f_{w}, but the correlation was relatively weak. A weak positive correlation between $r_{\mathrm{s}}/r_{\mathrm{w}}$ and f_{w} was observed. This is somewhat counter-intuitive, since the braking force increases when the mode is located closer to the wall. On the other hand, the mode growth might also be counter-acted by currents induced in the wall. A moderately negative correlation between f_{w} and ω_0 was observed, suggesting a decreasing need for correcting (increasing) the mode wall torque for modes with higher initial rotational frequency.

A plot of f_{w} is shown in Fig. 5.11. It shows that the correction factor f_{w} has

a tendency to decrease with the product of t_{lock} with $(w/a)_{\mathrm{crit,exp}}$. The latter is defined as the experimental island width calculated at $\omega = \omega_{\mathrm{crit}}$ (see Sec. 5.4.3). This means that the correction of the wall torque becomes less important for large islands with an extended braking phase. Furthermore, Fig. 5.11 resolves the disruption classes, suggesting that $f_{\mathrm{w}} > 1$ is systematically necessary for the DL class disruptions. In this particular class, l_{i} varied significantly during the time between braking initiation and disruption onset, as can be seen from the comparison of $l_{\mathrm{i}}(q_{95})$ operational diagrams calculated at $t = t_{\mathrm{slow}}$ (Fig. 5.10a) and $t = t_{\mathrm{disr}}$ (Fig. 5.10b). In the DL (and NBIOFF) cases, the range of l_{i} shifts between t_{slow} and t_{disr} by $\sim 15\%$. Entries below a virtual separation line at $l_{\mathrm{i}} = 1.3$ undergo, on average, minor shifts within the parametric space. It is noted that the separation is already noticeable in a similar diagram constructed from data at about 0.5 s before the onset of mode deceleration, at a slightly lower value of $l_{\mathrm{i}} \approx 1.1$. Density limit plasmas are likely to develop a cold edge, the resulting changes in the current profile may explain at least partially the need to correct the torque. In addition, interplay between local cooling by the mode and the presence of a cold edge might further enhance changes in the plasma momentum content. This point will be further discussed in Sec. 5.5.

Unfortunately, the relation between t_{lock}, f_{w} and the plasma density could not be examined for the full set of discharges, particularly for the DL cases.

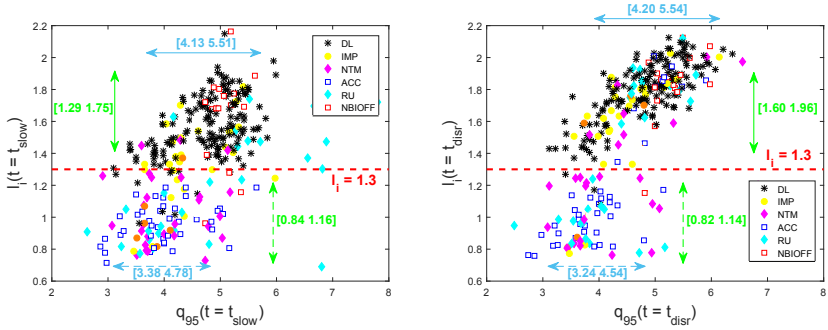

(a) (b)

Figure 5.10: $l_{\mathrm{i}}(q_{95})$ *diagrams for ROT and IRLM entries obtained (a) at the mode deceleration initiation (t_{slow}) and (b) at the disruption onset (t_{disr}). Note the distinct shift of the range of* l_{i} *for the groups of disruptions occurring at high plasma density.*

5.4.3 Experimental evaluation of the locking bifurcation condition

In the following, it is attempted to experimentally validate the dynamic condition for locking bifurcation given by Eq. (2.109) (only the 'co' braking scenario is considered). Out of the 103 cases suitable for application of the mode locking model (and therefore for the bifurcation condition validation), the necessary condition given by Eq. (2.107) for the locking bifurcation to take place was fulfilled in 61

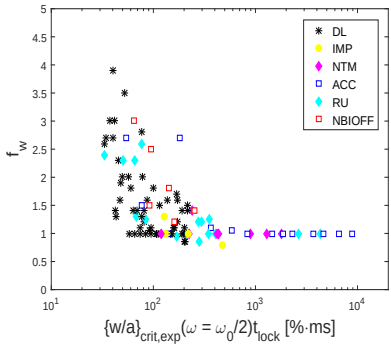

Figure 5.11: *Parameter f_{w} vs. $(w/a)_{\mathrm{crit,exp}} t_{lock}$, indicating disruption classes. The wall torque exerted on large modes locking over long temporal intervals requires a minimum artificial increment.*

cases. Furthermore, the conditions $\eta \geq 1$ (mode growing linearly or faster in time, recall Eq. (2.77)) and $\alpha \leq 9$ (i.e. the maximum value of this parameter across the parametric scan discussed in Sec. 2.5.3) were satisfied for 23 out of those 61 cases. Therefore, in only 23 cases it was possible to proceed to comparison of experimental and predicted critical island widths for locking. In Sec. 5.4.2, the experimental braking curves were reproduced for f_{M} between 1 and 18, whereas for the rest of the discharges, the value of this parameter was undetermined. Furthermore, this parameter is not included in the definition of the dynamic locking bifurcation condition. Therefore, in evaluating the critical island width for locking, $f_{\mathrm{M}} = 0$. For the purpose of further discussion, it is noted that Eq. (2.99) allows evaluating the critical mode frequency ω_{crit} at which a locking bifurcation takes place. In the following, using $f_{\mathrm{M}} = 0$, $\omega_{\mathrm{crit}} = \omega_0/2$ is obtained.

For each of the 23 cases, $(w/a)_{\mathrm{crit,s}}$ and $(w/a)_{\mathrm{crit,d,fit}}$ were *calculated* using Eq. (2.97) and Eq. (2.109), respectively. Means and medians of the calculated terms are displayed in Tab. 5.4. According to the expectations, the average/median dynamic critical island widths exceed the stationary equivalents.

Furthermore, $(w/a)_{\mathrm{crit,d}}$ is obtained from the fitted $w/a(t)$ curve at a time point at which the integrated braking curve decays in frequency to ω_{crit} (see an example in Fig. 5.12). In principle, $(w/a)_{\mathrm{crit,d,fit}}$ and $(w/a)_{\mathrm{crit,d}}$ should match. However, given the approximations made along derivation of Eq. (2.109) and together with that $A(t)$ was considered a function of time, whereas A is taken a constant in the definition of $(w/a)_{\mathrm{crit,d,fit}}$ (A was calculated from plasma parameters obtained at the time of initialization of the numerical integration for the purpose of the $(w/a)_{\mathrm{crit,d,fit}}$ calculation), $(w/a)_{\mathrm{crit,d,fit}}$ and $(w/a)_{\mathrm{crit,d}}$ can differ. In the example shown in Fig. 5.12, $(w/a)_{\mathrm{crit,d,fit}} \approx (w/a)_{\mathrm{crit,d}}$. Tab. 5.4 allows comparison of means/medians of the two critical island widths for the 23 discharges. The average effect of the two above factors results in $(w/a)_{\mathrm{crit,d,fit}} \approx 1.2\,(w/a)_{\mathrm{crit,d}}$.

It is noted that among the 23 here discussed discharges, multiple cases required f_{w} to match the experimental and predicted locking duration (for example, $f_{\mathrm{w}} = 1.4$ in case of the locking mode displayed in Fig. 5.12). Multiplication of the island width by $f_{\mathrm{w}} > 1$ typically resulted in the modification of the mode growth

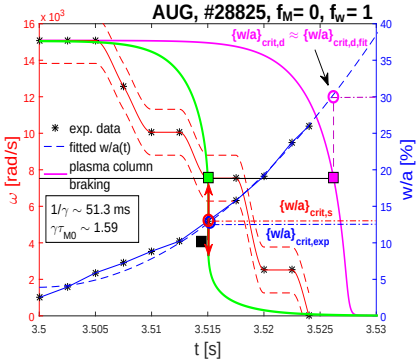

Figure 5.12: *Experimental evaluation of the condition for mode locking (i.e. the point of locking bifurcation) for discharge #28825 (2/1 mode), with* $f_{\mathrm{M}} = 0$, $f_{\mathrm{w}} = 1$. *The green line shows the static braking curve and the double red arrow delimits the forbidden frequency range, while the magenta line corresponds to dynamic braking (recall Fig. 2.16a). The experimental* $\omega(t)$ *data points were not smoothed, the discrete data points thus reflect the temporal and frequency resolution of the spectrogram (see Sec. 5.3).*

	$(w/a)_{\mathrm{crit,s}}$	$(w/a)_{\mathrm{crit,d,fit}}$	$(w/a)_{\mathrm{crit,d}}$	$(w/a)_{\mathrm{crit,exp}}$
Mean	15.5	35.8	31.1	13.7
Median	14.0	36.7	29.8	12.5
Std	6.1	9.3	9.3	6.5

Table 5.4: *Means and medians of* $(w/a)_{\mathrm{crit}}$ *of interest for* $f_{\mathrm{M}} = 0$, *expressed as percentages. Standard deviations were added in the last row ('Std').*

parameters and therefore the change in $(w/a)_{\mathrm{crit,d,fit}}$ and $(w/a)_{\mathrm{crit,d}}$. The observed variation was, however, minor.

Last column of the table contains the experimental island width at ω_{crit}, $(w/a)_{\mathrm{crit,exp}}$. It can be seen that the median experimental island width, calculated for the 23 cases of interest, exceeds both $(w/a)_{\mathrm{crit,d,fit}}$ and $(w/a)_{\mathrm{crit,d}}$ by the respective factors ~ 3 and ~ 2. It is thus reported that the physics elements contained in the dynamic condition for locking bifurcation are insufficient to reproduce the experiment.

Finally, the experimental island width at ω_{crit} was retrieved for all 103 discharges, regardless of whether the condition for locking bifurcation given by Eq. (2.107) was satisfied. With this manipulation, Tab. 5.5 presents summary statistics concerning $(w/a)_{\mathrm{crit,exp}}$ and $f_{\mathrm{w}}(w/a)_{\mathrm{crit,exp}}$. It can be seen that the mean 'corrected' $f_{\mathrm{w}}(w/a)_{\mathrm{crit,exp}}$ is larger than its experimental uncorrected equivalent by a factor of ≈ 1.3 in the 'co' scenario and 1.1 in the 'de' scenario.

Scenario		$(w/a)_{\mathrm{crit,exp}}$	$f_{\mathrm{w}}(w/a)_{\mathrm{crit,exp}}$
'co'	Mean	14.9 ± 6.9	19.6 ± 7.1
	Median	13.7	18.4
'de'	Mean	14.9 ± 6.9	16.3 ± 6.9
	Median	13.7	14.4

Table 5.5: *Means and medians, expressed as a percentage, of* $(w/a)_{\mathrm{crit,exp}}$ *and* $f_{\mathrm{w}}(w/a)_{\mathrm{crit,exp}}$ *for 103 discharges.*

5.5 Discussion

The model for mode locking that was used in this study can describe two extreme scenarios of the mode braking: either the mode locking is decoupled from the plasma bulk motion ('de'), or the plasma column decelerates with the mode ('co'). The evolution of the experimental rotation profiles shown in Sec. 5.4.2 suggests, however, that the actual situation might be a compromise between the two scenarios. The extent to which either scenario is a good approximation is likely related to the instantaneous mode width and the rate of the mode growth relative to the rate of momentum redistribution. In practical applications, one could estimate the critical mode width for locking and the locking duration using the two scenarios, resulting in an interval of critical locking parameters with boundaries defined by the two braking scenarios.

Degradation of the confinement properties during the discharge can occur due to multiple reasons, which can be difficult to disentangle. In some cases, setting $f_{\mathrm{M}} < 18$ and $f_{\mathrm{w}} = 1$ allowed reconstruction of the experimental braking curves, with the mode braking usually accompanying the onset of the momentum confinement deterioration (Sec. 5.4.2). In those cases, momentum confinement times at locking, predicted by Eq. (2.72), agreed with the experimental data points, decreasing the initial momentum confinement time by a factor $\lesssim 6$. For a number of examined locking modes, the predicted value of the momentum confinement time for $f_{\mathrm{M}} \gg 1$ was of the order of milliseconds or less. For a given constant torque density input, such low values would imply a plasma column at almost complete rest at locking. However, experimental rotation profiles often reveal a delayed deceleration of the central part of the plasma, with respect to the mode (see Ref. [124] for a similar observation in the JET tokamak).

In a substantial fraction of the cases studied here, the calculated wall torque was not large enough to reproduce the experimentally observed locking (Sec. 5.4.2). A similar observation was reported in DIII-D tokamak, hypothesized in Ref. [122] to originate from the existence of a second in-vessel conducting structure that could contribute to mode locking. The characteristic resistive time of this second structure would be an order of magnitude smaller than that of the vacuum vessel. As a result, a component of the wall torque would be introduced, reaching a maximum at comparatively higher mode frequencies, compensating for the missing braking torque. However, this model involving two resistive shells does not appear to be a suitable candidate to explain the missing torque in the here reported observations, since the need to compensate for the missing torque only presented itself under specific discharge conditions, not universally (see below).

Within the scope of the model used in this thesis, the stationary condition for the locking bifurcation is only suited for determining the critical mode width for locking when the mode grows on a sufficiently long time scale compared to that of the momentum redistribution. Therefore, in most practical applications the dynamic condition for the bifurcation should be used instead. Here, the dynamic bifurcation condition was restricted to certain mode growth scenarios and did not include the momentum confinement time degradation (Sec. 2.5.3). Validation of this theoretical condition was thus affected by those restrictions. In Sec. 5.4.3 it turned out that the predicted and experimental critical island widths differed substantially, possibly due to the above limitations. The dynamic condition for the locking bifurcation is a step forward in estimating the critical island widths in practical cases, but highlights the necessity to include more physical mechanisms in its definition.

The condition for the locking bifurcation, given by Eq. (2.107), was satisfied for about 60% of the 2/1 braking modes and 20% of the 3/1 modes. The rest of modes thus lacks a theoretical definition of the critical island width for mode braking. It is of interest, however, to examine at which island widths the modes typically lock in the full set of 103 discharges. Normalized island widths at half of the frequency decay were thus calculated in all cases. It turned out that at this point, the islands typically extend over about 15% of the plasma radius. However, to match the experimental and numerically calculated locking durations, the modes would have to extend, on average, over about 20% of the radius for the scenario with full plasma column braking (Sec. 5.4.3). The critical island width in a scenario of decoupled island braking would be more compatible with the experiment.

The mode locking model used here takes into account only two forces on the mode and assumes a rigid body motion, either fully coupled to or decoupled from the plasma bulk. A more detailed description of the mode locking should incorporate additional forces, such as interactions with external fields, and consider the momentum redistribution by solving the momentum transfer across the plasma [125]. On the other hand, the feasibility of such a scheme might be questioned in the context of a large database, or as a real time application during the discharge. In contrast, an advantage of the simple model used here is that it might allow to estimate locking durations and critical mode widths in real time.

One possible source of deceleration that was neglected in this work is the poloidal component of the wall force term, as the motion in this direction was assumed to be damped. However, according to Ref. [28], the associated force term component is, when evaluated with the discharge-specific parameters, one or two orders of magnitude larger than the toroidal component. Thus, identifying the circumstances under which the poloidal component of the force becomes important, could be a next step in the analysis of the mode braking.

Multiple root causes can destabilize resistive instabilities and a clustering according to disruption class was recognizable in the operational diagram containing l_i and q_{95}, about half a second before the locking onset [73] (Sec. 5.4.2). Following the study presented here, it appears that the model can predict locking durations for disruptions falling into certain disruption classes. The model systematically fails to predict locking of initially rotating modes that are driven unstable at high plasma density and/or that are compromised by a high impurity content. In discharge #28227, where the model failed to reproduce the experimental braking curve (Sec. 5.4.2), the mode was seeded after a cold region, originally located

at the vessel inner bottom (see Fig. 5.13a), was detected at the inner midplane (Fig. 5.13b). Following a slight separatrix movement, a local density increase was observed. Unfortunately, the DCN interferometers suffered from fringe jumps during the cold region development. However, the CO_2 interferometer edge channel (not routinely examined at AUG due to the high noise level and sensitivity to the external heating power and environmental conditions) shows the effect of the cold region on density (Fig. 5.13c). Specifically, a transient density increase can be observed, up to about 2.5×10^{20} m^{-3}, presumably owing to the corresponding line-of-sight intersecting the cold and dense region. At an increased density the plasma rotational frequency would have to decrease for the toroidal angular momentum to remain constant.

The mode equation of motion, accounting for the effect of a mass increase due to local particle source, e.g. caused by a MARFE, adopts the following form [26]:

$$\frac{\mathrm{d}\omega}{\mathrm{d}t} = -\frac{\omega}{n_\mathrm{e}}\frac{\mathrm{d}n_\mathrm{e}}{\mathrm{d}t} + \frac{n_{\mathrm{e}0}\omega_0}{n_\mathrm{e}\tau_{\mathrm{M}0}} - \frac{\omega(1+f_\mathrm{M}f_\mathrm{w}\frac{w}{a})}{\tau_{\mathrm{M}0}} - A\left[f_\mathrm{w}\frac{w}{a}(t)\right]^4 \frac{\omega\tau_\mathrm{w}}{(\omega\tau_\mathrm{w})^2+m^2}. \quad (5.5)$$

Here, $n_{\mathrm{e}0}$ is the electron density at the resonant surface at the onset of braking. In case of fast ($\ll \tau_{\mathrm{M}0}$) and large variations of the density, the first term on the right-hand side can dominate the mode slowing down, while for $\mathrm{d}n_\mathrm{e}/\mathrm{d}t \approx 0$ (i.e. $n_\mathrm{e} \approx n_{\mathrm{e}0}$) the equation approaches its original form of Eq. (2.79). A test was conducted to integrate Eq. (5.5) in the decoupled braking scenario, at the same time mimicking the presence of a significant density increase during mode braking. A simplified model with constant $\mathrm{d}n_\mathrm{e}/\mathrm{d}t$ was applied for the rate of density increase, starting from $n_{\mathrm{e}0} = 10^{20}$ m^{-3} at the onset of the mode deceleration and ending at a maximum density $n_{\mathrm{e,max}} = 2.5 \times 10^{20}$ m^{-3} roughly at the end of the braking phase, in accordance with the CO_2 interferometer data. The density variation was also taken into account for calculating the parameter A_de from Eq. (2.76). Note that in Fig. 5.13c the density probably fluctuates due to the cold dense region moving in and out of the viewing chord, even though it is assumed to represent a density increase during the entire braking phase. The resulting braking curve is plotted in Fig. 5.13d (cyan dotted curve) and compared with the result from the mode equation Eq. (2.79) without the density increase (dashed-dot magenta curve). The settings $f_\mathrm{M} = 5$ and $f_\mathrm{w} = 1$ were used, the former value chosen in order to match the experimentally observed decrease of the momentum confinement (Fig. 5.8b). It can be seen that the output of Eq. (5.5) agrees well with the experimental braking curve at the initial phase of braking, reducing the need to artificially increase the decelerating wall torque.

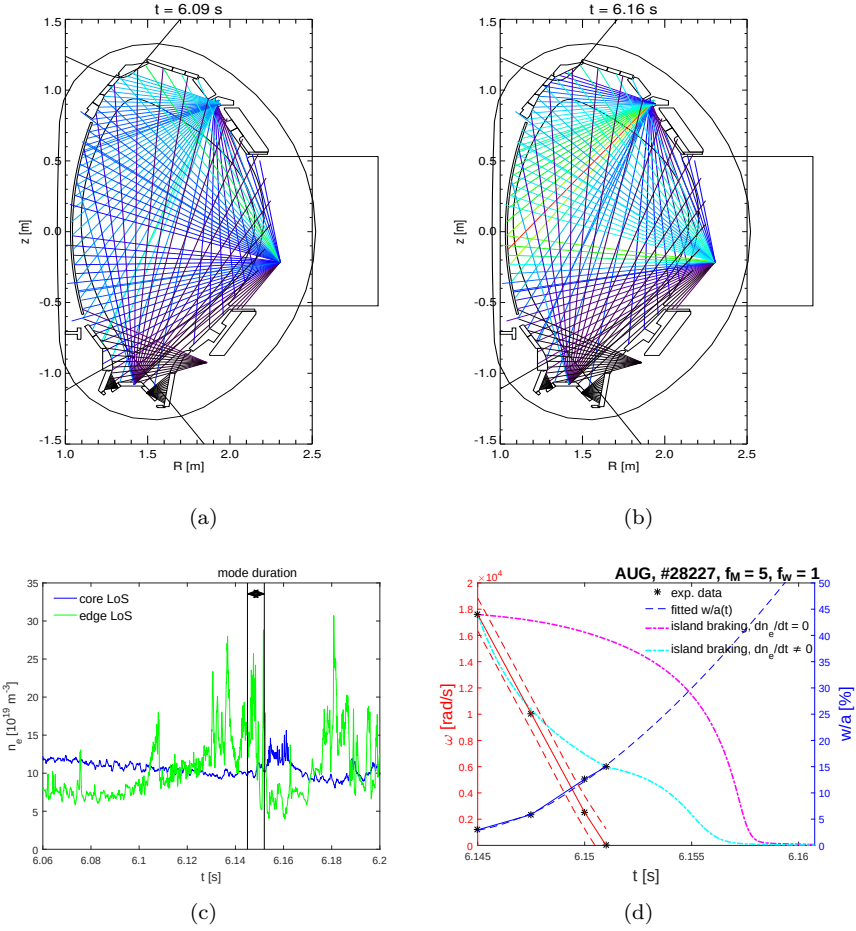

Figure 5.13: *Illustration of an attempt to reconstruct the braking curve in NBI-heated discharge #28227. (a) and (b) display AXUV diode bolometry signals, colour-coded according to relative emissivity (dark blue = low emissivity, light green = medium, red = high). In (a), at $t = 6.09$ s, a cold region has developed and is visible in the channels viewing the vessel HFS bottom. (b) At $t = 6.16$ s the cold region is recognizable near the inner midplane. (c) Line-integrated electron density measurements from the CO_2 interferometer. The core LOS is nearly unaffected by the cold and dense region, while in the edge channel its influence can be clearly noticed between about 6.1 and 6.2 s. In particular, during the presence of the mode, the density reaches $\approx 2.5 \times 10^{20}$ m^{-3}. (d) Comparison of braking curves obtained by integrating the mode equation either with a modelled local particle source (Eq. (5.5), cyan dotted) or without (magenta dash-dotted).*

6. Temporal and growth characteristics of disruption precursors

6.1 Motivation

Given the fact that most of disruptions were identified to be caused by a locked mode in the past [112], number of devices implement in the discharge emergency shut-down schemes a real-time monitoring of the locked mode amplitude (by means of magnetic sensors) [126–128]. The thresholds at which the warning signals are initiated have been set upon experience with the device operation. This machine protection scheme is a simple version of a disruption forecasting algorithm, introduced in Sec. 1.4, that aims to decide at which levels of plasma parameters the disruption is inevitable and once the critical levels are reached, acts to protect the device components. It is recalled that the disruption mitigation action can consist of a fast current ramp-down initiation, (de-) activation of external heating modules and ultimately of quick filling of the vacuum chamber by gas or pellets. The time sampling of the plasma control system and the gas (pellet) filling modules add to a reaction time necessary for the ultimate disruption mitigation.

In the past, a cross-device analysis of the mode disruptive amplitude yielded the scaling formula for the threshold radial magnetic instability field, expressed by Eq. (2.110). Recall that the formula allows estimating the disruptive amplitude for discharge-specific plasma parameters and it might thus represent a key input for the disruption forecasting algorithms. Equally important as the critical amplitude levels are the time scales at which the instability develops and reaches the critical amplitude. An a-priori estimation of the locked mode duration would help to decide in the PCS design whether a real-time monitoring of the amplitude *alone* provides the required minimum reaction time for the disruption mitigation. Eventually, in the real-time application, a disruption avoidance action might be first initiated by the PCS if the predicted durations would be favourably long.

Ideally, the time scales of the mode durations would be derived by calculating the mode growth rates [129], but in practice this appears feasible in a limited number of specific cases only. The measured locked mode amplitude often exhibits complex behaviour and events such as minor disruptions, mode re-rotation under constant external torque input etc. Those factors are currently not fully understood and complicate thus the mode development modelling. Furthermore, Sec. 4.3 reported on that a *locked mode* represents a widely used technical term, even though the mode can still rotate at the moment of its detection by the saddle coils. This motivated the definition of the saddle coil signal and locked phase durations in Sec. 4.3.

In this chapter, the large database of disruptive discharges, introduced in Chap. 4, will be used for a cross-device analysis of the saddle coil signal and locked

phase durations, evaluation of the predictive capability of the scaling Eq. (2.110) and regression analysis of the measured locked phase duration. Those tasks will be on multiple occasions discussed in the context of the disruption classes. Given the broad range of plasma parameters, discharge scenarios and disruption root causes, an empirical approach will be adopted in this chapter, including number of phenomenological observations.

This chapter is organized in the following way. Sec. 6.2 focuses first on analysis of factors that can influence the experimental mode durations. Both technical and physics aspects of the problem will be addressed. Secondly, the mode growth features are examined by construction of the time-to-disruption curves. Sec. 6.3 reports on regression analysis of the experimental locked phase durations. Scaling formulae, allowing to make extrapolations to ITER, will be presented. In Sec. 6.4, the predictive capability of the scaling formula for the disruptive mode amplitude will be examined in the context of the mode dynamics, sensor relative positions within the tokamak and the disruption class. A limited predictive capability of the scaling equation in case of rotating modes or sensors located at the inner torus side will be reported. For the latter case, a correction of the scaling will be presented. A discussion of the results is given in Sec. 6.5.

6.2 Experimental saddle coil signal and locked phase durations

In the following, the measured saddle coil signal (Δt_{SC}) and locked phase (Δt_{LP}) durations are examined. Sec. 6.2.1 will concern the parameter medians. The reported values will be discussed in the context of initiation of the emergency ramp-down, onset of minor disruptions and the relative occurrence of disruption classes. Sec. 6.2.2 will focus on the experimental mode (signal) growth description. In particular, time-to-disruption curves will be constructed and number of cases that develop certain levels of the disruptive mode amplitude at a particular time point prior to the disruption onset will be reported. The shape of the curves will be inspected and the typical mode growth scenario in AUG will be discussed.

The mode growth characteristic time scale, τ_{G}, is assumed to be limited by the resistive diffusion time scale τ_{R}, Eq. (2.13), and the Alfvén time τ_{A}, Eq. (2.11), i.e. $\tau_{\mathrm{R}} > \tau_{\mathrm{G}} > \tau_{\mathrm{A}}$. When applicable, the information is thus presented in the context of a, i.e. the plasma characteristic length scale included in the above time scale definitions ($L \to a$).

6.2.1 Median saddle coil signal Δt_{SC} and locked phase Δt_{LP} durations

Ideally, the dependence of the mode growth rate on plasma parameters would be determined from first principles, resulting in an analytical expression for the mode duration. Number of not fully understood phenomena, mentioned above, complicate this task. Here, it is decided that the saddle coil signal duration Δt_{SC} serves as a measure of mode duration for all database entries. This decision follows from that $\Delta t_{\mathrm{SC}} > 0$ everywhere (Sec. 4.3). This duration is determined by a multitude of factors related to the plasma conditions, as well as characteristics

of the device and the saddle coils. The upper panel of Fig. 6.1a displays medians (the second quartiles, Q2) and first and third quartiles (Q1 and Q3, marking the lowest and highest 25% of data, respectively) of the two parameters as a function of a (ROT entries were excluded from the calculation of Δt_{LP} as $\Delta t_{\mathrm{LP}} = 0$ there). COMPASS data retrieved from the low-field-side coils are shown. It appears that the respective median durations increase with a. This trend is favourable for ITER in terms of the time available for the PCS to take a disruption mitigation or avoidance action. The quartiles suggest that the distributions are rather broad and skewed towards longer durations (the respective medians, Q1 and Q3 numerical values are presented in Sec. 6.2.1, Tab. 6.2, second row). The distributions are shown in Fig. 6.1b. While the trend with a is evident, it should be noted that the simultaneous variation of other parameters in addition to the plasma size (e.g. relative occurrence of disruption classes), contributes to the uncertainty in the observed dependence. This fact motivated the construction of a scaling law for Δt_{LP} (Sec. 6.3). There, the regression analysis aims at disentangling the different effects.

The lower panel shows the ratio of the locked phase and saddle coil signal duration, $\Delta t_{\mathrm{LP}}/\Delta t_{\mathrm{SC}}$. It can be seen that in COMPASS Δt_{LP} constitutes typically about a quarter of the detected Δt_{SC}, while in DIII-D and JET the Δt_{SC} time scale is almost fully determined by the locked phase. The ratio is given by a combination of two aspects. Firstly, the physics driving the mode locking and a device-specific vulnerability to seeding of born-locked modes (recall Sec. 4.5). Devices with high occurrence of those modes will incline to equality of the two medians. Secondly, the properties of measuring instruments and the surrounding conducting structures affect the ratio. Here, important might be the sensitivity of saddle coils to the mode rotation phase (see Sec. 4.3), their relative location with respect to the vessel (in or out-vessel components) that influences the detection of the mode radial field component and the device specific wall characteristic time τ_{w} that determines the radial field attenuation.

In the following subsections, several aspects that could contribute to the calculated saddle coil signal and locked phase durations are discussed.

Effect of the emergency current ramp-down on Δt_{SC} (AUG, JET)

In a number of AUG and JET database entries, an 'emergency' current ramp-down (E-RD) was initiated by the plasma control system once a predefined signal threshold (such as that of the radial mode field amplitude $\tilde{B}_{\mathrm{r}}$ [126, 128]) was reached. The emergency discharge ramp-down is often considered as one of the first actions within the discharge emergency shut-down, aiming at the disruption mitigation. Other actions consist for example of switching on/off various external heating modules. The signal threshold for the massive gas (pellet) injection (if in use) typically exceeds that of the emergency ramp-down and it is considered as the last action within the disruption mitigation. Since the gas injection usually results in an extended vacuum chamber pumping to recover the working vacuum (and increases the vessel impurity content), the fast ramp-down initiation will be part of disruption mitigation actions preceding the massive gas (pellet) injection in ITER [130]. In this context, it is worth examining the influence of the fast ramp-down initiation on the experimental saddle coil signal time scales in AUG and JET.

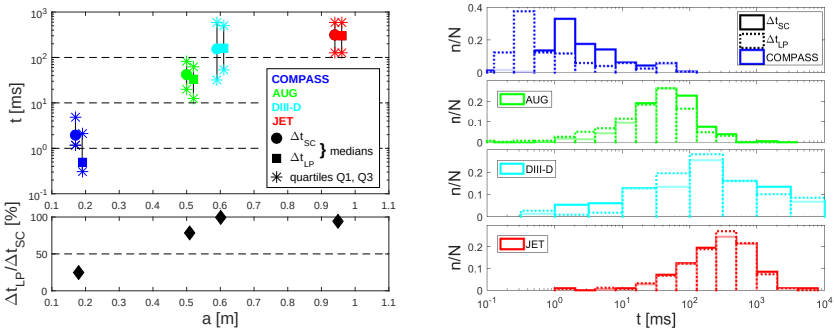

(a) (b)

Figure 6.1: *(a) Upper panel: Quartiles Q1, Q3 and Q2 (median) of the saddle coil signal and locked phase durations (Δt_{SC} and Δt_{LP}) displayed as a function of the plasma minor radius a. Lower panel: Ratios of $\Delta t_{\mathrm{LP}}/\Delta t_{\mathrm{SC}}$ in percentages. (b) Distributions of the two durations in the distinct devices.*

Device	AUG		JET	
	E-RD on	E-RD off	E-RD on	E-RD off
relative occurrence (%)	30	70	77	23
Δt_{SC} (ms)	72	35	385	101

Table 6.1: *Comparison of the median(Δt_{SC}) in AUG and JET for cases with an emergency current ramp-down prior the major disruption onset initiated ('E-RD on') and not ('E-RD off'). In both devices the median(Δt_{SC}) is lower in the 'E-RD off' scenario.*

In most of the here examined cases, the emergency ramp-down was triggered by reaching a threshold radial mode field amplitude. It was initiated in 30% and 77% of the AUG and JET database entries, respectively. The plasma response to the emergency current ramp-down can be of high complexity and it can result in a fast variation of plasma parameters (such as of the q_{95}). In Tab. 6.1, medians of the saddle coil signal duration Δt_{SC} for the 'E-RD on' and 'off' cases in the devices are displayed. It can be seen that, in both machines, the median(Δt_{SC}) is higher in the 'E-RD on' case. In the following, the effect of the emergency ramp-down initiation on the l_{i}/q_{95} ratio associated with the free energy supporting the mode growth (Sec. 2.3.2) is briefly examined.

In Fig. 6.2, an AUG discharge with an emergency ramp-down initiated at $t_{\mathrm{E-RD,on}}+\Delta t_{\mathrm{r}}$, where Δt_{r} is the plasma reaction time (of the order of miliseconds), is shown. It can be seen that after this temporal point the l_{i}/q_{95} ratio does not increase any more. The mode amplitude fluctuates until the final growth period terminated by disruption at $t = t_{\mathrm{disr}}$, when the locked mode amplitude is ~ 2 mT. Stabilization of the source of driving energy for the mode, represented by the l_{i}/q_{95} ratio, might contribute to the extension of the saddle coil signal duration. The stabilization is assumed to be associated with the increase in q_{95} that follows the ramp-down initiation. Multiple discharges, exhibiting the parameter ratio

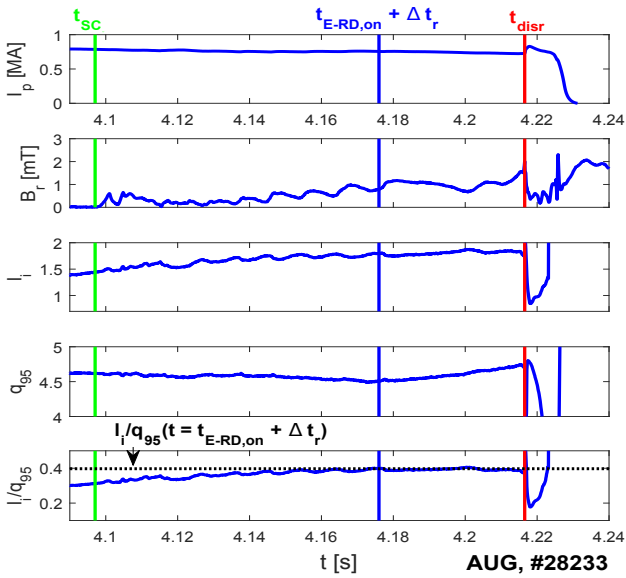

Figure 6.2: *Example of an AUG discharge with an emergency ramp-down initiated at* $t = t_{\mathrm{ER-D,on}}$*, leading to stabilization of the* l_i/q_{95} *ratio.*

stabilization similar to that of the example shown in the figure, were manually identified both in AUG and JET. Examination of this candidate explanation of the time scale extension on a larger statistical set will be subject of further studies.

It is noted that, in DIII-D, the real-time emergency ramp-down schemes are implemented in the plasma control system too [127]. Since it was initiated in $< 5\%$ of the database entries, its influence on the saddle coil signal durations was not examined due to lack of statistically relevant number of cases suitable for the analysis.

Relationship between Δt_{SC} and minor disruptions and delimitation of Δt_{SC} by the minor disruption onset time

One of the events that can result in a complex mode growth scenario is the occurrence of minor disruptions. The relative occurrence of those events in the particular devices has been shown in Tab. 3.1. For those cases, the minor disruption onset time did not equal the major disruption onset time, i.e. $t_{\mathrm{min.disr}} \neq t_{\mathrm{disr}}$. Here, the number of discharge specific minor disruptions in the context of the measured saddle coil signal duration Δt_{SC} in the devices of interest is briefly discussed. Relationship between the two parameters is visualized in Fig. 6.3a. Figs. 6.3b-6.3d will serve as a supportive material for consideration of physics aspects that might contribute to the data distribution presented in Fig. 6.3a. Secondly, a discussion will concern the effect of reducing the saddle coil signal duration to a time interval separating the saddle coil signal and the first minor disruption onsets which might be potentially desirable in large, high performance plasmas.

Fig. 6.3a can be divided in two parts delimited by rectangles '1' and '2'. Entries in the latter case display a proportionality relationship between the two parameters, i.e. for longer Δt_{SC}, a larger number of minor disruptions can take place before the major disruption onset. In the former case, no minor disruptions were observed prior to t_{disr}. Further analysis showed that the majority of discharges within the group '2' belong to DL, NBIOFF, ACC and IMP classes (their lower occurrence in DIII-D and COMPASS might lead to rather low presence of minor disruptions), while the group '1' is mainly populated by BLIM, LOQ and LON class entries. A relationship between the minor disruption onset and high plasma impurity content has been reported in the past, as well as the rare presence of those events within the LOQ classes [131]. The occurrence of minor disruptions has also been compared with the mode dynamics (i.e. affiliation to the ROT/IRLM/BLM groups), but no relationship was observed, i.e. the occurrence of minor disruptive events appears decoupled from the instantaneous mode dynamics.

A relationship between the occurrence of minor disruptions and selected plasma parameters was examined. Fig. 6.3b displays the number of minor disruptions as a function of q_{95} calculated at the saddle coil signal onset time t_{SC}. It can be seen that discharges experiencing minor disruptions are encountered for a broad range of q_{95} values. A virtual boundary (depicted by the colour-coded dashed lines) can be recognized in the plot, delimiting roughly an upper limit of minor disruptions sustained by the plasma for a given q_{95}. It can be seen that in JET case, the line is steeper, suggesting that for given q_{95} the plasma can sustain higher number of minor disruptions there. Furthermore, a weak correlation (i.e. the absolute value of the Pearson correlation coefficient is between 0.2 and 0.4) between the number of minor disruptions and $q_{95}(t = t_{\mathrm{SC}})$ was identified in the AUG and DIII-D cases, but not in JET. On the other hand, number of minor disruptions and $l_i/q_{95}(t = t_{\mathrm{SC}})$ correlate negatively and moderately (the range of the correlation coefficient is between 0.4 and 0.6) in JET, while in the two other devices, no correlation was identified.

Fig. 6.3d is a reduction of Fig. 6.3b (upper panel) and Fig. 6.3c (lower panel) for JET (disruption classes are indicated). In the upper panel, the number of ACC cases with high occurrence of minor disruptions ($\gtrsim 5$) can be recognized close to the dashed border line. It appears thus that the plasma might sustain a higher number of minor disruptive events in case of the ACC disruption class prior to major disruption. ACC class entries in JET do not experience substantial drops in temperature (unlike DL AUG entries, recall Fig. 4.1, the fifth panel, in which both and core ECE channels display reduction in temperature to $\sim 50-75\%$ of the pre-minor disruption value). In fact, the temperature is often observed to recover the pre-minor disruptive level [49], as was pointed out in Sec. 2.4. This statement is reflected in the median plasma AUG and JET temperatures shown in Tab. 3.1. Note that the median drop in T_{e} during the time interval separating the saddle coil signal detection and the disruption onset is by a factor ~ 3 in AUG, while in JET the drop is by a factor ~ 2. Furthermore, in Sec. 6.2.1 it will be shown that the median saddle coil signal duration of the ACC JET group entries is the second longest (after the LON class). The temperature recovery, often observed in this JET disruption class, might thus be one of the physics factors that determine the measured saddle coil signal duration. In particular, it might lead to its extension with respect to other class entries were the temperature drops during the minor disruption can be more significant.

In the lower panel, a delimiting line can be drawn along $l_i/q_{95} = 0.31$, dividing the plot in the region mainly populated with the ACC class entries and the rest. The moderate correlation, reported in the context of Fig. 6.3c, is preserved for the cases with $l_i/q_{95} < 0.31$. The mechanism driving the minor disruption onset might differ for the discharges delimited by the border line. Detailed examination of the relationship between l_i, q_{95} and the minor disruption occurrence is out of the scope of this thesis. Effect of enhanced radiation due to impurities on destabilization of minor disruptions for a given plasma current has been studied for example in Ref. [43].

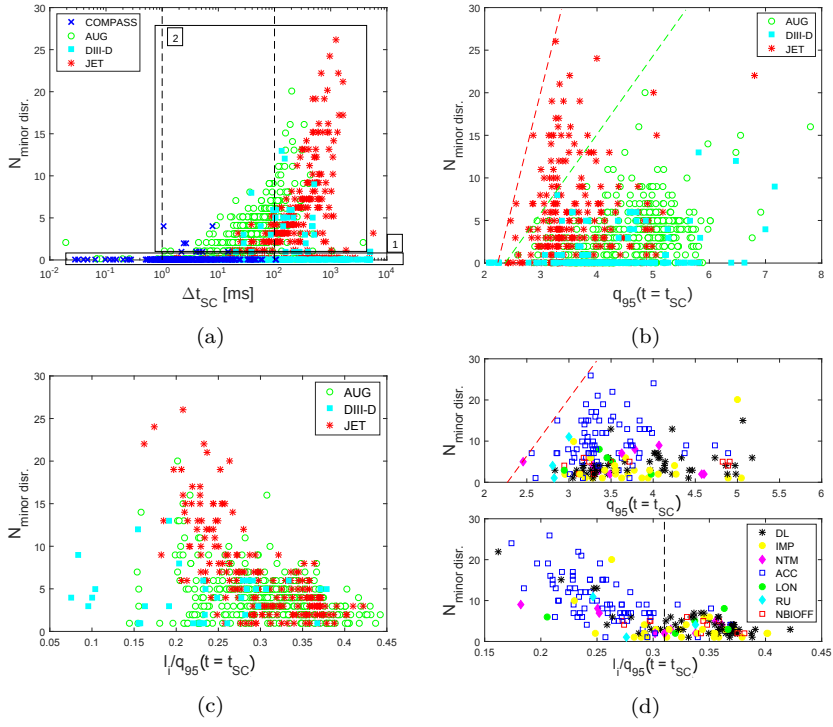

Figure 6.3: *(a) The number of minor disruptions preceding the major disruption onset* t_{disr}*,* $N_{\mathrm{minor\ disr.}}$*, shown in the context of the corresponding saddle coil signal duration* Δt_{SC}*. (b) The number of minor disruptions preceding* t_{disr} *shown in the context of* q_{95} *and (c)* l_i/q_{95} *calculated at* t_{SC}*. Data points with* $N_{\mathrm{minor\ disr.}} = 0$ *were discarded from figure (c). Minor disruptions are rare in COMPASS, data related to this device are thus not shown. (d) Extract of (b) and (c) with only JET data points. Disruption classes are indicated.*

In large, hot plasmas, the thermal energy loss during minor disruptions might represent a risk to the plasma facing components in terms of their melting. Hence, for high temperature plasmas, it might be of interest to focus the disruption prediction schemes towards the onset of the first minor disruptive event (i.e. the point of the first thermal quench, when the plasma temperature can still be close to the

maximum discharge values). The potential reaction time of the saddle coil signal based disruption prediction scheme on the upcoming minor disruption was examined. To do that, the saddle coil signal duration was reduced (when applicable) to a time interval separating the saddle coil signal onset and the first minor disruption occurrence, i.e. $\Delta t_{\mathrm{SC,red}} = t_{\mathrm{min.disr}} - t_{\mathrm{SC}}$ ('red' stands for 'reduced'). Tab. 6.2 provides a comparison of the median(Δt_{SC}) (i.e. the saddle coil signal duration as defined in Sec. 4.3) and the median($\Delta t_{\mathrm{SC,red}}$). It can be seen that, particularly in devices with a high fraction of database entries having $t_{\mathrm{min.disr}} \neq 0$, the decrease in the calculated median is by a factor $\sim 2 - 17$, shortening thus significantly a reaction time on the upcoming disruptive event.

Device		COMPASS	AUG
$\Delta t_{\mathrm{SC}} = t_{\mathrm{disr}} - t_{\mathrm{SC}}$	Δt_{SC} (ms)	1.2,**2.0**,4.9	20,**42**,82
$\Delta t_{\mathrm{SC,red}} = t_{\mathrm{min.disr}} - t_{\mathrm{SC}}$		1.1,**1.9**,4.6	2.1,**6.3**,14
Device		DIII-D	JET
$\Delta t_{\mathrm{SC}} = t_{\mathrm{disr}} - t_{\mathrm{SC}}$	Δt_{SC} (ms)	31,**152**,588	128,**308**,588
$\Delta t_{\mathrm{SC,red}} = t_{\mathrm{min.disr}} - t_{\mathrm{SC}}$		7.0,**77**,480	6.0,**18**,191

Table 6.2: *The second and third rows compare the Q1,**median(Δt_{SC})**,Q3 for the cases of the saddle coil signal duration delimited by t_{disr} and $t_{\mathrm{min.disr}}$, respectively. The quartiles suggest that the distributions are rather broad and skewed towards longer durations.*

Δt_{SC} associated with the disruption classes

Finally, the calculated saddle coil signal durations Δt_{SC} in the context of the disruption classes is presented. Tab. 6.3 displays the median(Δt_{SC}) (and quartiles Q1, Q3) calculated for distinct disruption classes in the four devices. Modes of long duration are systematically falling in the LON class. Of particularly extended durations in DIII-D are the NTM and RU class entries, the latter case is observed in COMPASS too. In JET, a long Δt_{SC} appears bound with the ACC, RU and the NTM classes. On the other hand, modes within the IMP, BLIM and LOQ groups have the shortest durations. Entries within the last two groups approach the ideal instability disruptive limits and can thus develop on the associated short time scale. The greatly varying time scales depending on disruption class, combined with the different relative occurrence of disruption classes over the devices (Tab. 4.3) contributes to the width of the time scale distributions shown in Fig. 6.1a.

6.2.2 Experimental saddle coil signal growth description in terms of time-to-disruption parameter

As was demonstrated earlier, the measured radial component of the mode field often exhibits fluctuations and periods of a non-linear growth. Retrieving experimentally the information concerning the mode growth rate (not the *signal* growth rate) is typically possible only for a narrow subgroup of modes, often falling in

Device		DL	IMP	NTM
COMPASS	Δt_{SC} (ms)	-,**0.94**,-	0.7,**1.0**,1.6	1.3,**1.9**,4.3
AUG		31,**48**,82	5.8,**15**,20	9.8,**27**,116
DIII-D		7.5,**53**,141	-,**8.2**,-	227,**822**,1.7e3
JET		128,**175**,290	49,**101**,415	136,**231**,801
Device		ACC	LON	RU
COMPASS	Δt_{SC} (ms)	2.2,**2.6**,5.5	-,**4.4**,-	7.2,**20**,37
AUG		9.1,**36**,77	106,**151**,255	14,**62**,134
DIII-D		-,**-**,-	87,**198**,363	162,**401**,4.4e3
JET		316,**477**,738	461,**679**,971	-,**254**,-
Device		NBIOPFF	BLIM	LOQ
COMPASS	Δt_{SC} (ms)	-,**3.8**,-	0.8,**1.2**,2.9	0.1,**0.8**,1.6
AUG		42,**62**,87	-,**1.7**,-	-,**-**,-
DIII-D		58,**121**,168	2.6,**12**,55	-,**32**,-
JET		87,**97**,191	-,**-**,-	-,**99**,-

Table 6.3: *Q1,**median**(Δt_{SC}),Q3 calculated for distinct disruption classes in the devices of interest (Q1 and Q3 not shown if number of class entries < 10).*

the LON disruption class [112]. In those cases, a monotonic mode growth was observed. Nevertheless, usually, the mode amplitude time evolution is complex. In the context of disruption forecasting, it is important to retrieve information concerning the temporal evolution of the mode to examine how soon a particular level of the disruptive mode amplitude can be detected prior to the disruption onset. This motivates the construction of the time-to-disruption curves, defined below.

A time-to-disruption interval (TtD) for a specific level X ($\mathrm{TtD_X}$) of experimental disruptive mode amplitude $B_{\mathrm{r,disr}}$ is defined as a time interval that separates the major disruption from the time at which the particular disruptive level ($X\%$ $B_{\mathrm{r,disr}}$) is first reached. It is important to note that $B_{\mathrm{r,disr}}$ was calculated in the post-discharge processing phase (its predictions will be discussed in Sec. 6.4). In the example shown in Fig. 6.4a, $\mathrm{TtD_{50}}$ is highlighted. The time interval translates into the available warning time for the PCS to react on the upcoming disruption (~ 25 ms in the displayed case). It is recalled that in case of modes rotating prior to locking, the measured amplitude growth rate might not necessarily reflect the actual mode growth, but the signal growth rate. The latter may depend on the properties of the conducting structures surrounding the saddle coils, such as the wall resistive time τ_{w}. In the particular case of Fig. 6.4a, the mode finally locks at $t = 1.535$ s and the measured steep amplitude growth, observed during a time interval $\sim$ (1.535 1.540) s, is probably related to the reduction of wall shielding as the mode locks. It is noted that the mode rotation phase can constitute a non-negligible portion of the saddle coil signal duration Δt_{SC} in COMPASS and AUG (recall Fig. 6.1a). In the following, it is considered as inseparable from Δt_{SC}.

For all database entries, the durations $\mathrm{TtD_{10}}$, $\mathrm{TtD_{50}}$ and $\mathrm{TtD_{90}}$ were calculated. In Fig. 6.4b, the resulting time-to-disruption curves for the four devices are shown. The curves are displayed against a fraction of disruptions FD, i.e. the

number of disruptions (in %) for which a particular $\mathrm{TtD_X}$ reaches at least the duration delimited by intersection of an arbitrary normal with the horizontal axis (it is noted that the horizontal axis is expressed as a the time interval preceding the major disruption onset). Like that, one estimates the FD that would trigger an alarm on upcoming disruption, if the warning level on the mode amplitude was set at X% of the $B_{\mathrm{r,disr}}$. For instance, in AUG when one sets the detection threshold at 10% of $B_{\mathrm{r,disr}}$, 90% of the disruptions would have been detected at about 3.5 ms before t_{disr}. Many among those would be detected earlier, but only 50% of all AUG shots would have been detected at a TtD $\sim$ 7.5 ms. Setting the threshold higher, to 50% of $B_{\mathrm{r,disr}}$, would deteriorate the detection results. In particular, to reach a success rate of 90% of the cases in AUG, one would have only 1 ms until the disruption, while a success rate of 50% would be feasible at about 6 ms prior to t_{disr}. It is noted that only the cases where the measured mode field exceeded a threshold value $B_{\mathrm{r,thresh}} = B_{\mathrm{r,noise}} + 0.1$ mT (where $B_{\mathrm{r,noise}}$ is the average noise field level prior to the onset of the saddle coil signal t_{SC}) were included in the figure. This filtered out $[2, 4, <1, <1]$% of the database entries in the respective devices.

From the practical point of view, the $B_{\mathrm{r,disr}}$ would have to be a priori known. Its estimate can be obtained by using the scaling for the disruptive mode amplitude, Eq. (2.110) (the estimates will be obtained in Sec. 6.4).

The black curves in Fig. 6.4b represent the saddle coil signal durations Δt_{SC}. In all machines, the full Δt_{SC} distributions span over several orders of magnitude. The modes with the longest and shortest durations would fall in the respective disruption classes shown in Tab. 6.3. In COMPASS, a hard limit on Δt_{SC} is set by the pulse length, not exceeding 0.5 s, according to Tab 3.1.

In Fig. 6.4c, a vertical cross-section of Fig. 6.4b is shown for a selected time-to-disruption $\mathrm{TtD} = t_{\mathrm{PCS}} = 10$ ms, where t_{PCS} is a typical time scale of the exception handling plasma control system reaction in large devices [132,133]. It can be seen that in JET, nearly 100% of the modes develop on a time scale exceeding t_{PCS} prior to the major disruption onset t_{disr} and $\sim$ 80% of modes reach 10% $B_{\mathrm{r,disr}}$ during a time interval $> t_{\mathrm{PCS}}$. With decreasing a, the respective fractions of disruptions decrease, however. In ITER ($a = 2$ m), on the other hand, it appears that a vast majority of modes should reach 90% $B_{\mathrm{r,disr}}$ before t_{PCS}.

Fig. 6.4d displays three horizontal cross-section of Fig. 6.4b. Time-to-disruptions for a fraction of disruptions equal to [10,50,90]% are shown. The vertical spread (logarithmic) of the points from each particular device provides an idea of the typical mode growth nature. Data points located at FD = 10% (having a long TtD) have a narrow spread, suggesting a quasi-stable mode amplitude development. On the other hand, data dispersion at FD = 90% is broad, suggesting a steep mode initial growth followed by a quasi-stable locked mode amplitude period, finalized by a steep mode growth prior to the major disruption onset. A particularly broad distribution of Δt_{SC} and TtD in the case of DIII-D is well visualized in terms of a comparison of the FD = 10% and FD = 90% panels. While in the former case the TtD exceeds the JET data points, in the latter case the 10% $B_{\mathrm{r,disr}}$ (and $t_{\mathrm{disr}} - t_{\mathrm{SC}}$) data point is below the AUG level.

Finally, it is noted that the mode growth nature can be to a certain extent related to the disruption class, see the TtD curves for DL and ACC group entries in Fig. 6.4e. For example, data points at fraction of disruptions FD = 50% reveal that in the DL class 10% $B_{\mathrm{r,disr}}$ is reached shortly before the major disruption

onset and this time point is separated from lower mode amplitude levels by a relatively long time interval. The final fast mode growth takes place just before the disruption onset. In case of the ACC class, however, the difference between TtD of distinct mode amplitude levels is smaller, suggesting that the mode amplitude could be preferentially quasi-stable, in other words, the distinct levels of the disruptive mode amplitude were detected earlier than in the very final steep phase of the mode growth (see examples of DL and ACC group entries inserted in the figure). It is hypothesised that this growth nature might be related to the significant positive increment of the l_i/q_{95} in the DL disruption class, reported in Sec. 5.4.2. Increase of this parameter (median$[l_\mathrm{i}/q_{95}(t_\mathrm{disr}) - l_\mathrm{i}/q_{95}(t_\mathrm{SC})] = 0.11$) might provide drive for the mode growth, resulting in a progressive increase of the mode amplitude. In the case of the ACC class entries, the l_i/q_{95} increment is typically small (median$[l_\mathrm{i}/q_{95}(t_\mathrm{disr}) - l_\mathrm{i}/q_{95}(t_\mathrm{SC})] = 0.01$).

6.3 Regression analysis of the locked phase duration

In this section, Δt_LP is examined for the modes with IRLM and BLM dynamics. This duration is expected to be determined mainly by the physics of mode growth, while Δt_SC can be affected by the details of the machine and diagnostics. Dependencies of Δt_LP can be established through a scaling relation. This relation might serve as an input to the design of the plasma control system aiming at the disruption forecasting.

The regression analysis was carried out using a power law model for Δt_LP only. A linear model was tested too, but the power law model fitted the data better. Plasma parameters used for the regression were all calculated at $t = t_\mathrm{LP}$. A set of predictor variables, obtained from a step-wise linear regression of log-transformed data, was selected. A scaling formula of the following form was identified to have the highest capability of predicting the duration [134]:

$$\Delta t_\mathrm{LP}\ [\mathrm{ms}] = c_0 \cdot a^{c_a} \cdot \beta_\mathrm{N}^{c_{\beta_\mathrm{N}}} \cdot q_{95}^{c_{q95}} \cdot f_\mathrm{rad}^{c_{f_\mathrm{rad}}}, \tag{6.1}$$

Δt_LP is in seconds, a in meters and $f_\mathrm{rad} = P_\mathrm{rad}/P_\mathrm{IN}$ being the ratio of the total radiated power over the total power input. Two options were tested: either the factor c_0 was allowed to be disruption class dependent, or it was taken as common to all classes. The first option corresponds to a class-dependent offset of the scaling. It thus takes into account at least part of the variability of Δt_LP between distinct classes, reported in Sec. 6.2.1. In both cases, the other parameters (c_a, c_{β_N}, $c_{q_{95}}$ and c_{f_rad}) were common to all classes.

Tab. 6.4 and Tab. 6.5 present the results of weighted least squares regression. The first table displays the fit parameter and measures of goodness-of-fit for a common class offset, the second table shows the results for a class-dependent offset. The model was tested on two database subsets: BLM cases only (259 database points in total, 7 COMPASS, 88 AUG, 57 DIII-D and 107 JET cases); all cases with non-zero locked phase duration (761 database points in total, 104 COMPASS, 308 AUG, 107 DIII-D and 242 JET cases). Both tables contain the fit results for the two database subsets. To balance the contributions from distinct machines, weight factors were used for each sample i, given by $w_{ij}^{-1} = 2 + \sqrt{N_j}/4$, where N_j is the number of points contributed by device j [135].

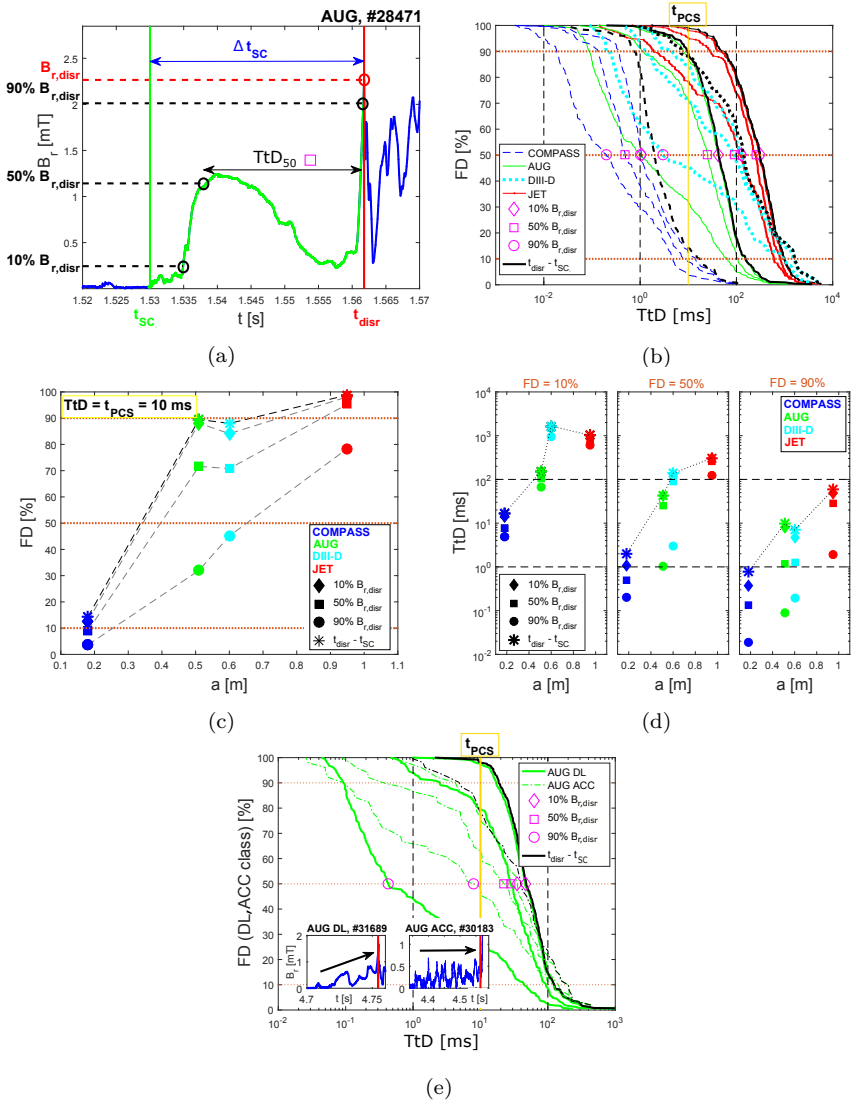

Figure 6.4: *(a) Example of an initially rotating locked mode disrupting plasma at* $t = t_{\mathrm{disr}}$ *(AUG).* TtD_{50} *and* $t_{\mathrm{disr}} - t_{\mathrm{SC}}$ *(i.e.* Δt_{SC}*) are highlighted by the black and blue arrows, respectively. The 10%, 50% and 90%* $B_{\mathrm{r,disr}}$ *threshold levels are indicated as well. (b) TtD curves for [10,50,90]%* $B_{\mathrm{r,disr}}$ *in the respective devices. (c) Vertical cross-section of (b) displaying the FD values at TtD =* $t_{\mathrm{PCS}} = 10$ *ms. (d) Horizontal cross-section of (b) displaying TtD for FD = [10,50,90]%. In figures (b-d)* Δt_{SC} *durations are displayed in black. (e) TtD curves for [10,50,90]% of the experimental* $B_{\mathrm{r,disr}}$ *shown for DL and ACC AUG group entries (typical mode amplitude time traces are inserted).*

A clear trend is observed for Δt_{LP} in terms of minor radius and safety factor in both offset variants. In addition, a weak dependence of the duration on β_{N} and f_{rad} is reported. A prediction $\widehat{\Delta t}_{\mathrm{LP}}$ was made for an ITER scenario with $\beta_{\mathrm{N}} = 1.8$, $q_{95} = 3$ and $f_{\mathrm{rad}} = 0.5$ [12,17,136]. The predicted values, $\widehat{\Delta t}_{\mathrm{LP,ITER}}$, are shown in the tables. In the case of a class-dependent offset, the DL class was used for making a prediction, because of its relatively high occurrence in the database. Predictions for other classes can be obtained by adjusting the multiplication factor.

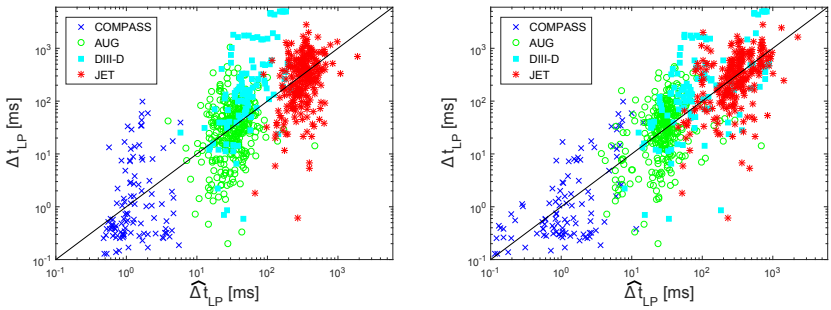

Figure 6.5: *Predicted locked phase durations* $\widehat{\Delta t}_{\mathrm{LP}}$ *plotted against experimental values* Δt_{LP}*. The predictions were obtained from power law scaling with (a) common and (b) class-specific offsets.*

It should be noted that the error bars, presented in the form of standard deviations, on the fitted parameters are relatively large. Moreover, the rather low coefficient of determination R^2 indicates that the model is able to explain only part of the data variability. This can be also seen in the plots of the duration predictions, $\widehat{\Delta t}_{\mathrm{LP}}$, shown in Fig. 6.5 for all points with non-zero locked phase duration against their experimental value Δt_{LP}. Sources of uncertainty can be related to the occurrence of minor disruptions, a rapid sequence of initially rotating and fast locking modes (observed often in AUG density limit disruptions), intentional variation of the plasma parameters, changes in the mode structure etc. All those events can take place after the locked phase onset. The results also reveal that the model with the class-dependent offset provides a better fit than the one with the common offset, especially for the COMPASS data.

Individual results shown in the tables indicate that Δt_{LP} can vary significantly among the various disruption classes. A similar conclusion was already drawn from Tab. 6.3 for Δt_{SC}. The longest locked phase durations are again found in the LON and RU classes, while the shortest locking phases tend to occur in the IMP, BLIM and LOQ classes.

The increasing trend of Δt_{LP} with plasma minor radius, which was also observed for Δt_{SC}, is incorporated in the model. In addition, the duration scales positively with q_{95}. This can be understood, because for larger edge safety factor the rational surface, where the mode occurs, is located closer to the plasma core region. Ref. [45] reported on the role of the distance between the mode and the plasma edge in the disruption onset and showed that with smaller distance the

Common offset								
Dataset (N)	c_0	c_a	c_{β_N}	$c_{q_{95}}$	$c_{f_{rad}}$	$\widehat{\Delta t}_{LP,ITER}$ (ms)	RMSE (ms)	R^2
BLM (259)	37 12	3.25 0.14	-0.40 0.08	1.21 0.25	-0.27 0.04	1270 320	1.4	0.55
$\Delta t_{LP} > 0$ (761)	8.0 3.5	2.72 0.28	-0.90 0.13	2.00 0.41	-0.31 0.07	345 130	1.5	0.61

Table 6.4: *Results of the power-law regression analysis, yielding the scaling Eq.* (6.1)*. The analysis was performed on the born-locked modes (BLM) only and all cases with non-zero duration of the locked mode phase. The fit parameters are presented in the rows, the first row contains the fitted parameter and the second its error bar (one standard deviation). RMSE, the-root-mean-squared error, and* R^2*, the coefficient of determination, are measures of the goodness-of-fit.*

likelihood of disruption increases. This observation is in correspondence with the results reported here. The duration also decreases with the radiated fraction f_{rad}. It appears, thus, that larger relative radiative losses (leading to plasma cooling and an increase in the resistivity) lead to shorter locked phase duration.

The two tables indicate that the dependence on a become somewhat weaker when the fit is restricted to BLM cases only. This may be related to the concomitant increased negative dependence on β_N, as a and β_N are quite strongly anti-correlated across the database (correlation coefficient -0.51). It is noted that the offsets are lower than in the combined case with IRLM and BLM points, contributing to a significantly lower duration prediction for ITER.

6.4 Validation of scaling formula for the disruptive mode amplitude

In this section, validation of the predictive capability of the scaling formula for the disruptive mode amplitude, Eq. (2.110), will be performed by applying it on a large set of disruptive discharges. This manipulation is important for the potential scaling application in next-step devices where the disruption forecasting will become critical. The predicted and experimental disruptive mode amplitudes will be compared and sources of eventual discrepancies will be examined. Then, the scaling formula will be used to construct scaled time-to-disruption curves. Number of cases that develop certain levels of the scaled disruptive mode amplitude at a particular time point prior to the disruption onset will be reported.

Most of the input for the scaling Eq. (2.110) results from the equilibrium reconstruction. Reliability of the equilibrium calculation can decrease prior to a disruption, particularly in the highly dynamic discharge phases comprising changes in the plasma shape, i.e. during the plasma current ramp-up or ramp-down. In a number of DIII-D cases, the equilibrium parameters suffered from large and fast fluctuations prior to the disruption onset time t_{disr}. Eq. (2.110) was thus not applied on those cases. Furthermore, in some DIII-D discharges, equilibrium data were not calculated until t_{disr} and those discharges were also not considered.

Class offset Dataset (N)	$c_{0,\mathrm{ACC}}$	$c_{0,\mathrm{BLIM}}$	$c_{0,\mathrm{DL}}$	$c_{0,\mathrm{BLIM}}$	$c_{0,\mathrm{LON}}$	$c_{0,\mathrm{LOQ}}$
BLM (259)	31 14	32 18	28 14	6.7 3.1	47 22	17.1 8.7
	$c_{0,\mathrm{NBIOFF}}$	$c_{0,\mathrm{NTM}}$	$c_{0,\mathrm{RU}}$	c_a	c_{β_N}	$c_{\mathrm{q}_{95}}$
	36 18	45 23	158 85	2.97 0.25	-0.63 0.12	1.31 0.45
	$c_{\mathrm{f}_{\mathrm{rad}}}$	$\widehat{\Delta t}_{\mathrm{LP,ITER}}$ (ms)	RMSE (ms)	R^2		
	-0.23 0.07	749 270	1.2	0.67		
$\Delta t_{\mathrm{LP}} > 0$ (761)	$c_{0,\mathrm{ACC}}$	$c_{0,\mathrm{BLIM}}$	$c_{0,\mathrm{DL}}$	$c_{0,\mathrm{BLIM}}$	$c_{0,\mathrm{LON}}$	$c_{0,\mathrm{LOQ}}$
	74 24	29 13	47 16	18.0 5.8	134 44	38 14
	$c_{0,\mathrm{NBIOFF}}$	$c_{0,\mathrm{NTM}}$	$c_{0,\mathrm{RU}}$	c_a	c_{β_N}	$c_{\mathrm{q}_{95}}$
	75 26	83 27	380 130	3.53 0.13	-0.19 0.08	1.12 0.26s
	$c_{\mathrm{f}_{\mathrm{rad}}}$	$\widehat{\Delta t}_{\mathrm{LP,ITER}}$ (ms)	RMSE (ms)	R^2		
	-0.18 0.04	1880 470	1.3	0.70		

Table 6.5: *The table content is organized similarly to that of Tab. 6.4, but the model implements a class-dependent offset.*

In total, 17% of the DIII-D database entries were discarded from the following analysis, leaving up 1086 points for the scaling validation.

Firstly, the predictive capability of Eq. (2.110) is examined by calculating the ratio $B_{\mathrm{r,disr}}/\hat{B}_{\mathrm{r,disr}}$, for all database entries ($\hat{B}_{\mathrm{r,disr}}$ is obtained with the usage of Eq. (2.110)). The respective medians corresponding to the devices of interest are listed in the third column of Tab. 6.6. The ratio distributions for the sum of IRLM and BLM group entries are displayed in Fig. 6.6b in bold lines and the medians are included in the table, third column. Modes locked at the disruption onset appear to match better the predicted values than the ROT group entries. In Sec. 4.3, it was discussed that due to the mode rotation, the calculated amplitude can be attenuated. This is probably reflected in the displayed mode field median ratio, as it can be seen that $\hat{B}_{\mathrm{r,disr}}$ systematically overestimates $B_{\mathrm{r,disr}}$. The fifth column in the table displays medians ± MAD of the ratio for the full database; in the last column, the ROT group entries are excluded in the respective devices. The $B_{\mathrm{r,disr}}/\hat{B}_{\mathrm{r,disr}}$ plot for the database (with ROT entries excluded) is shown in Fig. 6.6a. It can be seen that the JET case median approaches the equality of predicted versus experimental quantities the most. Furthermore, in the JET case, the $B_{\mathrm{r,disr}}/\hat{B}_{\mathrm{r,disr}}$ ratio distribution is rather narrow. It is noted that the majority of disruptive discharges used in Ref. [14] to obtain Eq. (2.110) were the same JET discharges used in this work. This fact can contribute to the relatively good matching of the predicted and experimental values.

The lowest median ratios are observed in the COMPASS HFS and AUG. In both cases, the sensors are located at the torus high-field-side. Eq. (2.110) does not take into account the effect of toroidicity (and the plasma shape) that would result in the substitution of the exponent in the radial mode field scaling $(r_{\mathrm{c}}/r_{\mathrm{q}})^{-|m|-1}$, see Sec. 2.5.2, reflected in the value of the ρ_{c} exponent in Eq. (2.110), by its 'effective' equivalent, m_{eff}. According to Sec. 2.5.2 $m_{\mathrm{eff}} > m$ and $m_{\mathrm{eff}} < m$ in the respective high and low-field-side cases. Given the fact that the majority of the discharges examined in Ref. [14] were calculated using data from the low-field-side sensors, applicability of the formula in the high-field side can suffer from uncertainties. In accordance with Sec. 2.5.2, a trial modification of Eq. (2.110) is performed by substituting the exponent in ρ_{c} to reflect the $m_{\mathrm{eff}} = 3.8$ for the $m = 2$ high-field-side case. The scaling equation thus becomes

$$B_{\mathrm{r,disr}}(r_c) = 8.5 \cdot I_{\mathrm{p}}^{1.07} \cdot a^{-1.1} \cdot q_{95}^{-1.2} \cdot l_{\mathrm{i}}^{1.2} \cdot \rho_{\mathrm{c}}^{-4.8}. \tag{6.2}$$

For the full AUG database, median ± MAD of the $B_{\mathrm{r,disr}}/\hat{B}_{\mathrm{r,disr}}$ ratio becomes 0.95 ± 0.42 (1.05 ± 0.38 with ROT excluded). In COMPASS HFS, one obtains 0.40 ± 0.60 (1.05 ± 0.60 with ROT excluded). With scaling Eq. (6.2), the predictions are clearly improved. In the following, for the AUG and COMPASS HFS cases, Eq. (6.2) is used instead of Eq. (2.110). It is noted that distributions of the $B_{\mathrm{r,disr}}/\hat{B}_{\mathrm{r,disr}}$ ratio calculated with Eq. (2.110) (JET, DIII-D and COMPASS LFS) and Eq. (6.2) (AUG) are displayed in Fig. 6.6b (dotted lines) and the respective medians ± MAD for the IRLM and BLM groups are 1.00 ± 0.44 and 0.95 ± 0.32 (COMPASS HFS data are excluded from the distributions).

The median ratio for distinct disruption classes were seen to lie within interval 0.70 and 0.90 (with the exception of the BLIM group where the ratio was ~ 0.15). It appears thus that the disruption class plays a minor role in the predictive capability of Eq. (2.110) (or Eq. (6.2)).

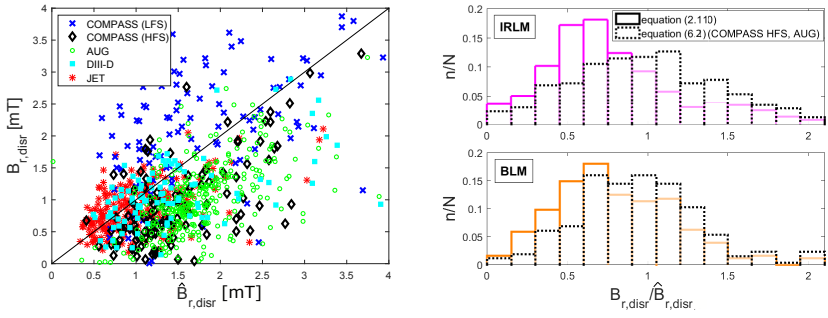

(a) (b)

Figure 6.6: *(a) Predicted disruptive mode amplitude* $\hat{B}_{\mathrm{r,disr}}$ *(calculated with Eq.* (2.110)*) plotted against its experimental equivalent,* $B_{\mathrm{r,disr}}$ *(ROT entries excluded). (b) Distributions of the* $B_{\mathrm{r,disr}}/\hat{B}_{\mathrm{r,disr}}$ *ratios retrieved for discharge groups formed according to the mode dynamics. Distributions in bold were obtained by using the scaling Eq.* (2.110) *for the full database. Distributions depicted by the dotted lines were obtained by using Eq.* (6.2) *for the COMPASS HFS and AUG cases.*

Scaling		(2.110)	(6.2)
$\frac{B_{\mathrm{r,disr}}}{B_{\mathrm{r,disr,s}}}$	ROT	0.32 ± 0.35	0.44 ± 0.42
	IRLM	0.70 ± 0.90	1.00 ± 0.44
	BLM	0.75 ± 0.31	0.95 ± 0.32
		Full databases	
	COMPASS HFS	0.24 ± 0.56	0.40 ± 0.60
	COMPASS LFS	0.74 ± 0.67	
	AUG	0.50 ± 0.53	0.95 ± 0.42
	DIII-D	0.75 ± 0.32	
	JET	0.84 ± 0.33	
		ROT excluded	
	COMPASS HFS	0.54 ± 0.29	1.05 ±0.60
	COMPASS LFS	1.15 ± 0.60	
	AUG	0.57 ± 0.20	1.05 ±0.38
	DIII-D	0.83 ± 0.29	
	JET	0.86 ± 0.32	

Table 6.6: *Medians ± MAD of the* $B_{\mathrm{r,disr}}/\hat{B}_{\mathrm{r,disr}}$ *ratio, the table sections differ by the mode dynamics and device. For the former, the LFS data in COMPASS are used. The latter is shown first for the full databases and then without the ROT cases.* $\hat{B}_{\mathrm{r,disr}}$ *was calculated using scaling Eq.* (2.110)*, data shown in the fourth column display* $\hat{B}_{\mathrm{r,disr}}$ *calculated with Eq.* (6.2) *in the COMPASS HFS and AUG cases.*

Device		DL	IMP	NTM	ACC	LON
COMPASS	FD (%)	0	0	2	0	0
AUG		78	25	63	45	100
DIII-D		36	0	52	-	25
JET		95	81	91	90	78
Device		RU	NBIOFF	BLIM	LOQ	
COMPASS	FD (%)	60	0	0	0	
AUG		78	83	0	-	
DIII-D		55	37	13	0	
JET		100	89	-	47	

Table 6.7: *Fraction of disruptions FD reaching 50% of the scaled disruptive amplitude $\hat{B}_{\mathrm{r,disr}}$ (calculated with Eq.* (2.110) *in COMPASS LFS, DIII-D and JET and Eq.* (6.2) *in AUG, COMPASS HFS data are roughly identical to the LFS case) in distinct disruption classes at the scaled time-to-disruption TtD interval equalling the typical plasma control system reaction time (TtD = t_{PCS} = 10 ms).*

Secondly, the focus is set on calculation of the time interval that separates the disruption onset from the time at which the measured mode amplitude reaches $\hat{B}_{\mathrm{r,disr}}$. Similarly to Sec. 6.2.2, for this purposes a time-to-disruption for a specific level X of the *scaled* disruptive mode amplitude ($\mathrm{TtD_X}$) is defined as a time interval that separates the major disruption from the point at which the particular scaled disruptive level ($X\%$ $\hat{B}_{\mathrm{r,disr}}$) first intersects $\tilde{B}_{\mathrm{r}} = f(t)$. An example is shown in Fig. 6.7a, the $\mathrm{TtD_{50}}$ is highlighted by the double arrow and the (10,50,90)% $\hat{B}_{\mathrm{r,disr}}$ time traces are displayed as well. Fig. 6.7b displays the resulting scaled time-to-disruption curves TtD for the devices of interest. It is worth emphasizing that not always $X\%$ $\hat{B}_{\mathrm{r,disr}}$ intersects $\tilde{B}_{\mathrm{r}} = f(t)$ prior to t_{disr}. Those cases are then missing in Fig. 6.7b. Fig. 6.7c shows the maximum fraction of disruption reached for the respective (10,50,90)% $\hat{B}_{\mathrm{r,disr}}$ levels in the four devices. It can be seen that detection of $X\%$ $\hat{B}_{\mathrm{r,disr}}$ prior to t_{disr} is for the three disruptive amplitude levels maximized in JET and AUG. In DIII-D, in only about $\sim 40\%$ of the examined cases the 90% of the scaled disruptive amplitude intersects the $\hat{B}_{\mathrm{r}}$ experimental time traces prior to the major disruption onset.

Fig. 6.7d displays a vertical cross-section plot similar to that presented in Fig. 6.4c, i.e. the fraction of disruptions reaching a particular predicted disruptive mode amplitude at the scaled time-to-disruption time TtD = t_{PCS} = 10 ms (recall that t_{PCS} is a typical plasma control system reaction time scale). One observes about $\sim$ 95% and $\sim$ 30% of the disruption fraction reaching 10% $\hat{B}_{\mathrm{r,disr}}$ and 90% $\hat{B}_{\mathrm{r,disr}}$, respectively, at this time point in JET. The respective fractions of disruptions for the distinct predicted mode levels decrease with the device minor radius, with the AUG data points exceeding those of DIII-D.

The fraction of disruptions reaching 50% $\hat{B}_{\mathrm{r,disr}}$ at the scaled time-to-disruption TtD= t_{PCS} in devices of interest for distinct disruption classes are shown in Tab. 6.7. The fraction of disruptions in the respective devices is in accordance with the observation reported in Fig. 6.7d, i.e. the overall fraction of disruptions is maximised in JET and the AUG data exceed those of DIII-D. We note that the lowest fraction of disruptions appears related to the LOQ, BLIM and IMP cases.

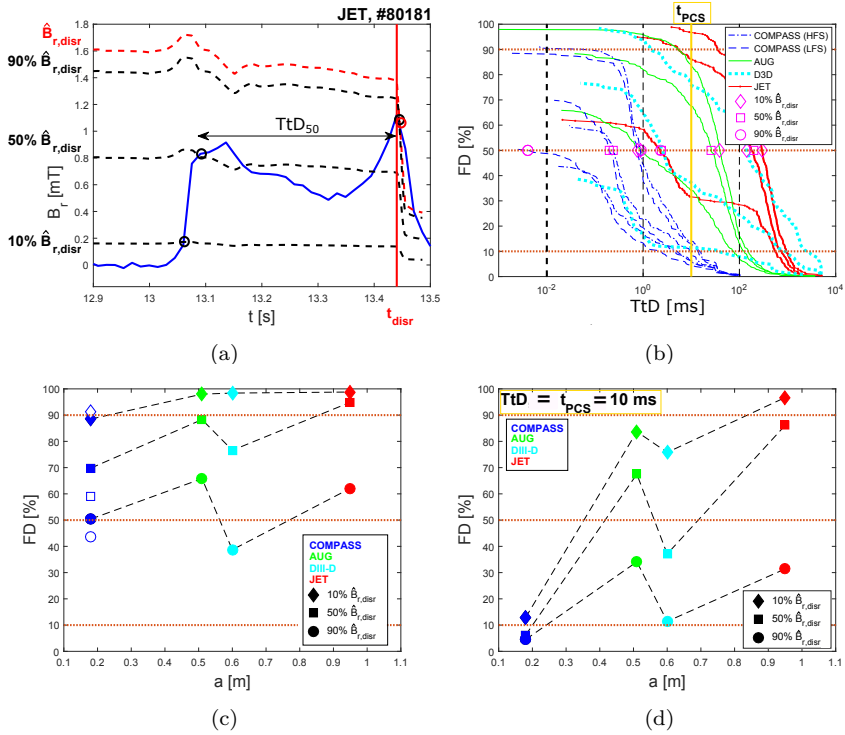

Figure 6.7: *(a) Example of a locked mode disrupting plasma at* $t = t_{\mathrm{disr}}$ *(JET). (10,50,90)%* $\hat{B}_{\mathrm{r,disr}}$ *time traces and* TtD_{50} *are highlighted. In this example,* $t(B_{\mathrm{r}} = \hat{B}_{\mathrm{r,disr}}) > t(B_r = B_{\mathrm{r,disr}})$*, encircled in red is the point at which* $\hat{B}_{\mathrm{r,disr}}$ *intersects the experimental* B_{r} *time trace. (b) TtD curves for (10,50,90)% of the scaled* $\hat{B}_{\mathrm{r,disr}}$ *in the respective devices. (c) Maximum fraction of disruption FD of the distinct* $\hat{B}_{\mathrm{r,disr}}$ *levels detected prior to* t_{disr}*. (d) Vertical cross-section of (b) displaying FD reached at TtD =* $t_{\mathrm{PCS}} = 10$ *ms. For COMPASS, only LFS data points are shown (HFS data points are roughly equal).*

6.5 Discussion

Sec. 4.3 showed that the mode locked and (fast) rotation phases are typically monitored by independent detectors. Calculation of the locking mode amplitude thus often suffers from discontinuities and/or uncertainties at the borders of the measuring instrument ranges. A reliable continuous measurement of the mode amplitude would represent an improved input to the plasma control system. Ref. [137] reports on a method suitable for such continuous measurement, accounting for the removal of the wall mirror current contribution to the measured amplitude. The method is expected to be applicable in ITER.

It is reported here that the highest and lowest fractions of the born-locked modes were observed in the largest and smallest examined devices, respectively, i.e. in JET and COMPASS. Extrapolating this observation to larger devices is not straightforward. Intrinsic and extrinsic sources of the plasma rotation (reflected in the mode rotation rate), intensity of the error fields (and their correction), discharge scenario and other aspects might determine whether for a given plasma the particular mode will rotate prior to locking. Earlier references have, nevertheless, reported on the vulnerability of large plasmas to the error field born-locked modes (see Sec. 4.5).

Time-to-disruption curves would represent a starting point for the analysis of the optimized settings of the disruption predictor in terms of premature and false alarms [138]. A large set of non-disruptive discharges, having a locked mode, will have to be assembled in the future to perform this analysis.

In Sec. 6.3, a regression analysis of the locked phase durations was carried out and a scaling formula was presented (Eq. 6.1). This scaling can serve as a rough estimate of the locked phase duration, possibly in real-time, given that the input in terms of the equilibrium quantities and instantaneous radiative losses is supplied. It should be noted that the formula does not yield any information about the mode growth nature. Furthermore, the scaling is not fully expressed upon normalized quantities. Future improvement of the scaling in this perspective might improve its applicability and increase its predictive capacity.

The scaling presented in Ref. [14] for the disruptive mode amplitude has been applied to the experimental data set in Sec. 6.4. This manipulation allowed the scaling validation on a large set of discharges pertaining to multiple device experimental campaigns. The largest deviation of the predicted vs. experimental data points was observed in case of sensors located at the torus high-field side and modes (slowly) rotating at the disruption onset. Concerning the former, the scaling equation has been adjusted for the effect of toroidicity for the high-field-side case, adopting the effective poloidal mode number from Chap. 2. The predictive capability of the scaling relation was improved in COMPASS high-field-side and AUG cases. With this adjustment, the scaling has shown its merit in the prediction of the locked mode disruptive amplitude. Concerning the rotating modes, it is hypothesised that because of the currents driven in the wall, the calculated radial component of the slowly rotating mode amplitude is attenuated, causing the scaled disruptive amplitude to overestimate systematically the measured radial field mode component. Apart from those two points, the scaling formula relies on the input from the equilibrium reconstruction. Low temporal resolution and poor reconstruction quality (often encountered in the ramp-down, circular plasmas, shortly prior to the disruption) can compromise the scaling applicability.

7. Summary and outlook

High performance tokamak operation faces many challenges. Among them, disruptions are particularly threatening to the device components. To secure the designed ITER operation, it is likely that the plasma control system will, in the scope of the disruption prevention, employ schemes that will rely on data-driven algorithms benefiting from the input from physics models and scalings.

To provide additional insight in the physics underlying the development of a disruption, a large (> 1100 entries) database of disruptive discharges has been created. Data were collected in four devices with varying plasma size and common criteria on the entries were applied during the database assembly. Therefore, the database represents a suitable base for the exploratory analysis of the MHD disruption precursors. Multiple observations were discussed in the context of the mode dynamics and the disruption class, thus, a particular care was taken to identify those characteristics properly. A disruption classification was performed by manual inspection of objective discharge-related information and an emphasis was set on unifying the classification cross-device. Nevertheless, it is noted that the class label remains to a certain level subjective, especially in case of complex discharges showing signs of multiple mode destabilizing mechanisms.

In the scope of this thesis, the database was used to study multiple aspects of the disruption prediction and/or avoidance. The majority of the results obtained in this work was presented in Chap. 5 and Chap. 6.

In Chap. 5, the validation of a previously derived mode locking model was presented. Key information concerning the duration of braking phase and critical mode width for locking might be supplied to the disruption avoidance and prediction schemes by the characterization of the braking with the model. A reduced database of ASDEX Upgrade discharges exhibiting a locking mode was used for the model validation. The model incorporated braking force due to electromagnetic interaction between the mode and the conducting vessel wall, as well as the restoring viscous force and its degradation due to growth of the mode.

The mode braking model showed its merit in describing deceleration of large modes locking over temporal intervals comparable to the momentum confinement time, in case the mode deceleration phase was initiated in a quasi-stationary rotating plasma column. Under such conditions, the model could predict the duration of the braking phase. On the other hand, the theoretical critical mode width for locking, set at the dynamic point of the locking bifurcation, could not be reliably compared with the experiment due to limitations in the locking bifurcation definition.

For a substantial fraction of discharges, often those occurring in high-density plasmas, the calculated wall torque was not sufficient to reproduce the locking dynamics and the braking of the initially rotating modes could not be explained on the basis of the physical mechanisms contained in the model. To increase the predictive capability of the model for plasmas experiencing a transient increase of the plasma density in the vicinity of the mode location, it was proposed to add a local particle source in the mode equation of motion.

In Chap. 6, the database was used to study time scales at which the saddle

coil signal and the locked phase durations (i.e. another key parameter of interest in the context of disruption prevention) develop, to establish a scaling formula for the locked phase duration and to validate a previously derived scaling for the disruptive mode amplitude.

In all devices, it was reported that multiple boundaries of the safe operation space were probed. Owing probably to this fact, the saddle coil signal durations were shown to span over multiple orders of magnitude in all devices. ITER will explore boundaries of the non-disruptive operation space and it is thus likely that the durations will span several orders of magnitudes there too.

Multiple factors that could influence the measured durations, such as the plasma dimensions, the response of the plasma control system to exceptional situations, specific location of the discharge within the device parametric space (often reflected in the disruption class affiliation) and occurrence of minor disruptions, were discussed. The effect of some of these factors on the mode characteristics could be quantified using the empirical scaling, albeit with a large uncertainty on the predictions.

Application of the scaling formula for the locked phase duration (Eq. 6.1) to the ITER Baseline scenario suggests that this time interval will be on the order of hundreds of miliseconds or seconds in ITER. Such time scales are favourable for a timely disruption mitigation in the device, as the ITER PCS minimum reaction time for this action is designed to 30 ms [113]. This positive statement is supported by the observation that the median signal saddle coil and locked phase durations were shown to increase with the plasma size.

The scaling formula for the locked phase duration does not predict the mode growth nature in ITER. However, one can extrapolate the fraction of disruptions reaching a certain level of the mode amplitude linearly with the plasma minor radius. Like that, it is possible to obtain an estimate of the percentage of cases that will develop this level at a given time point prior to disruption. It is necessary to stress that this single parameter extrapolation is undoubtedly oversimplifying the problem. Nevertheless, the extrapolation performed for 90% of both the scaled and experimental disruptive mode amplitude levels suggests that in a majority of the modes, this mode amplitude level would be reached at least 10 ms prior to the disruption onset in ITER. Once again, this speaks in favour of a timely disruption mitigation mentioned above in case of this device.

This thesis employed two approaches in the study of the MHD disruption precursors. A model for mode braking was validated using a reduced database of disruptive discharges in ASDEX Upgrade. Yet, the reduced database was composed of discharges covering a broad range of plasma parameters. The model limitations were identified, owing to the broad plasma condition range. Next, an empirical approach was adopted in the study of the locked phase durations in the four devices. A number of concurrent aspects were identified as possibly influencing the duration. Given the complexity of the phenomenon, a report of phenomenological observations represents a natural first approach to the problem.

The mode amplitude monitored by magnetic sensors, in particular its critical disruptive level and its development in time, constituted the main parameter that was studied in the scope of this work. Focus on this parameter-diagnostic combination was driven by the fact that the critical mode amplitude has been identified as a primary disruption trigger in the past and by the relative sim-

plicity and broad usage of the diagnostic instrument. This thesis followed the parameter critical properties from the initially rotating phase, through the locking, until the disruption onset. It has been pointed out that in large devices this sequence of events might reduce to born-locked modes disrupting the plasma. The combined information about the initially rotating mode development, coming from the model for mode braking (adjusted for the here discussed limitations), the here reported scaling for the locked phase durations and the earlier scaling for the disruptive amplitude, validated here, might represent an important input to the disruption forecasting schemes that profit from physics models and data-driven algorithms, such as the DECAF code described in Ref. [139].

Due to the severe limitation in number of acceptable unmitigated disruptions in the ITER high performance scenario [20], it is unlikely that the PCS decision-taking logic, in the view of the disruption prevention, would rely only on one (yet important, such as the mode amplitude) diagnostic signal. Work presented here suggests that apart from the mode amplitude, of interest might be to follow the evolution of l_i/q_{95} ratio, the radiated fraction, plasma beta, density etc. The here compiled database might serve for construction of time-to-disruption curves related to the development of those parameters and examination of their relevance in the disruption forecasting.

Symbols and acronyms

A	Mass number
a	Minor plasma radius
$\tilde{B}$	Perturbation helical magnetic field
B	Nucleus binding energy
B_ϕ	Equilibrium poloidal magnetic field
B_θ	Equilibrium toroidal magnetic field
$\tilde{B}_\mathrm{r}$	Perturbation radial magnetic field component
$\tilde{B}_\theta$	Perturbation poloidal magnetic field component
b	Wall thickness
c	Speed of light
g	Gravitational constant
$\mathbf{j}$	Current density
$\tilde{J}_s$	Surface current
k_B	Boltzmann constant
L	Characteristic length scale
l_i	Plasma internal inductance
m	Poloidal mode number
$m_\mathrm{e/i}$	Mass (electron/ion)
n	Toroidal mode number
$n_\mathrm{e/i}$	Density
p	Pressure
P_tot	Total auxiliary power input
P_rad	Total radiated power
q	Safety factor
q_0	Safety factor at the magnetic axis
q_{95}	Safety factor at the flux surface enclosing 95% of the toroidal flux
q_a	Safety factor at $r = a$ (cylindrical plasma)
r	Minor radial coordinate
r_L $(r_\mathrm{L,e/i})$	Larmor radius
r_w	Wall minor radius
R	Major radial coordinate
R_0	Major plasma radius
R_geo	Geometric major radius
R_m	Magnetic Reyonolds number
R_mag	Magnetic major radius
R_p	Radiation parameter
S	Surface
$\underline{\boldsymbol{S}}$	Viscous stress tensor
T $(T_\mathrm{e/i})$	Temperature (electron/ion)
T_NBI	Torque supplied by the neutral injection
t_ROT	Rotating mode duration
t_disr	Disruption time
v_A	Alfvén velocity

v_i	Ion velocity
v_ϕ	Plasma bulk velocity
V_loop	Loop voltage
W	Potential energy
W_th	Plasma thermal energy
w	Magnetic island width
β	Ratio of kinetic and magnetic pressure
γ_0	Heat capacity ratio
γ	Growth rate
Δ'	Stability index
Δm	Mass defect
δ	Resistive layer width
δ_b	Bottom plasma triangularity
η	Resistivity
θ	Poloidal angle
θ^*	Straight field line angle
κ	Plasma elongation
$\underline{\boldsymbol{\kappa}}$	Thermal conductivity tensor
λ_D	Debye length
λ_mfp	Mean free path
μ_0	Vacuum permeability
ρ	Mass density
σ	Conductivity
τ_D	Magnetic diffusion time scale
τ_E	Energy confinement time
τ_M	Momentum confinement time
τ_R	Resistive diffusion time scale
τ_w	Resistive wall time
ϕ	Toroidal angle
Φ_B	Magnetic flux
$\boldsymbol{\Psi}$	Equilibrium flux function
$\tilde{\psi}$	Perturbation flux function
ω	Angular frequency

ASDEX	Axially Symmetric Divertor EXperiment
BLM	Born-Locked Mode
COMPASS	COMPact ASSembly
CXRS	Charge Exchange Recombination Spectroscopy
ECE	Electron Cyclotron Emission
ECRH	Electron Cyclotron Resonance Heating
FT	Flat-Top
ICRH	Ion Cyclotron Resonance Heating
IRLM	Initially Rotating Locked Mode
JET	Joint European Torus
MARFE	Multi-faceted Axisymmetric Radiation From the Edge
MHD	Magnetohydrodynamics
NBI	Neutral Beam Injection
NTM	Neoclassical Tearing Mode
PCS	Plasma Control System
ROT	ROTating mode
RD	Ramp-Down
RU	Ramp-Up
TS	Thomson Scattering
VDE	Vertical Displacement Event

Bibliography

[1] J.G.J. Olivier and J.A.H.W. Peters (Netherlands Environmental Assessment Agency). *Trends in Global CO2 and Total Greenhouse Gas Emissions*. `http://www.pbl.nl/sites/default/files/cms/publicaties/pbl-2018-trends-in-global-co2-and-total-greenhouse-gas-emissons-2018-report_3125.pdf`, 2018. [cit. September 2019].

[2] International Energy Agency. *Global Energy & CO2 Status Report*. `http://webstore.iea.org/download/direct/2461?fileName=Global_Energy_and_CO2_Status_Report_2018.pdf`, 2019. [cit. September 2019].

[3] S.E. Liverhant. *Elementary Introduction to Nuclear Reactor Physics*. John Wiley & Sons, 1960, ISBN: 978-0471541547.

[4] H.S. Bosch and G.M. Hale. *Improved Formulas for Fusion Cross-sections and Thermal Reactivities*. Nuclear Fusion, 32(4):611, 1992.

[5] J.D. Lawson. *Some Criteria for a Power Producing Thermonuclear Reactor*. Proceedings of the Physical Society, 70(1):6, 1957.

[6] H. Zohm. *Magnetohydrodynamic Stability of Tokamaks*. Wiley-VCH, 2015, ISBN: 978-3527412327.

[7] Consiglio Nazionale delle Ricerce. *Tokamak and Stellarator*. `https://www.ifp.cnr.it/la-fusione-nucleare/tokamak-and-stellarator?&set_language=en`, September 2016. [cit.October 2019].

[8] Heating ITER Physics Expert Group on Energetic Particles and Current Drive. *Plasma auxiliary heating and current drive*. Nuclear Fusion, 39(12):2495, 1999.

[9] F. Wagner *et al. Development of an Edge Transport Barrier at the H-Mode Transition of ASDEX*. Physical Review Letters, 53(15):1453, 1984.

[10] K.H. Burrell *et al. Physics of the L-mode to H-mode Transition in Tokamaks*. Plasma Physics and Controlled Fusion, 34(13):1859, 1992.

[11] H. Zohm. *On the Minimum Size of DEMO*. Fusion Science and Technology, 58(2):613, 2010.

[12] ITER Organization. `https://www.iter.org/construction/construction`. [cit.October 2019].

[13] ITER Organization. `https://www.iter.org/gallery/com_image_download#411`. [cit.October 2019].

[14] P.C. de Vries *et al. Scaling of the MHD Perturbation Amplitude Required to Trigger a Disruption and Predictions for ITER*. Nuclear Fusion, 56(2):026007, 2016.

[15] R.S. Granetz *et al. Disruptions and Halo Currents in Alcator C-Mod*. Nuclear Fusion, 36(5):39, 1996.

[16] J. Wesson. *Tokamaks*. Oxford University Press, 2011, ISBN: 978-0198562931.

[17] J.M. Linke *et al. Performance of PFC Materials in Tokamaks and Stellarators*. Fusion Science and Technology, 42(1):142, 2004.

[18] B.N. Breizman *et al. Physics of Runaway Electrons in Tokamaks.* Nuclear Fusion, 36(/8):59, 2019.

[19] C. Reux *et al. Runaway Electron Beam Generation and Mitigation During Disruptions at JET-ILW.* Nuclear Fusion, 55(9):093013, 2015.

[20] M. Lehnen *et al. Disruptions in ITER and strategies for their control and mitigation.* Journal of Nuclear Materials, 53(15):39, 2015.

[21] G. Pautasso *et al. On-line Prediction and Mitigation of Disruptions in ASDEX Upgrade.* Nuclear Fusion, 42(1):100, 2002.

[22] R. Moreno *et al. Disruption Prediction on JET during the ILW Experimental Campaigns.* Fusion Science and Technology, 69(2):485, 2016.

[23] G.A. Ratta *et al. Viability Assessment of a Cross-Tokamak AUG-JET Disruption Predictor.* Fusion Science and Technology, 74(1-2):13, 2018.

[24] M. Odstrĉil *et al. Comparison of Advanced Machine Learning Tools for Disruption Prediction and Disruption Studies.* Plasma Science, IEEE Transactions on, 41:1751, 2013.

[25] R. Fitzpatrick. *Helical Temperature Perturbations Associated with Tearing Modes in Tokamak Plasmas.* Physics of Plasmas, 2(3):825, 1995.

[26] Private communication with H. Zohm.

[27] V. Igochine *et al. Active Control of Magnetohydrodynamic Instabilities in Hot Plasmas.* Springer, 2015, ISBN: 978-3662442227.

[28] M.F.F. Nave and J.A. Wesson. *Mode Locking in Tokamaks.* Nuclear Fusion, 30(12):2575, 1990.

[29] R.H. La Haye *et al. Cross–machine Benchmarking for ITER of Neoclassical Tearing Mode Stabilization by Electron Cyclotron Current Drive.* Nuclear Fusion, 46(4):451, 2006.

[30] H. Alfvén. *Existence of Electromagnetic-Hydrodynamic Waves.* Nature, 150:405, 1942.

[31] P.A. Davidson. *An Introduction to Magnetohydrodynamics.* Cambridge University Press, 2001, ISBN: 978-0521794879.

[32] S. Galtier. *Introduction to Modern Magnetohydrodynamics.* Cambridge University Press, 2016, ISBN: 978-1316665961.

[33] J.P. Freidberg. *Ideal MHD.* Cambridge University Press, 2014, ISBN: 978-0511795046.

[34] D. Biskamp. *Nonlinear Magnetohydrodynamics.* Cambridge University Press, 1997, ISBN: 978-0511599965.

[35] E. Priest. *Magnetic Reconnection.* Cambridge University Press, 2000, ISBN: 978-0511525087.

[36] V.D. Shafranov. *Plasma Equilibrium in a Magnetic Field.* Reviews of Plasma Physics, 2:103, 1966.

[37] F. Troyon *et al. MHD Limits to Plasma Confinement.* Plasma Physics and Controlled Fusion, 26(1A):209, 1984.

[38] M. Kruskal and J.L. Tuck. *The Instability of a Pinched Fluid with a Longitudinal Magnetic Field.* Proceedings of the Royal Society A, 245:222, 1958.

[39] V.D. Shafranov. *The Stability of a Cylindrical Gaseous Conductor in a Magnetic Field*. Reviews of Plasma Physics, 1(5):709, 1956.

[40] A. Dinklage. *Plasma Physics: Confinement, Transport and Collective Effects*. Springer, 2005, ISBN: 978-3540252746.

[41] R.H. Rutherford. *Nonlinear Growth of the Tearing Modes*. Physics of Fluids, 16(11):1903, 1973.

[42] R.S. Cohen *et al. The Electrical Conductivity of an Ionized Gas*. Physical Review, 80(2):230, 1950.

[43] M.F. Turner and J.A. Wesson. *Transport, Instability and Disruptions in Tokamaks*. Nuclear Fusion, 22(8):1069, 1982.

[44] C.Z. Cheng *et al. MHD Stable Regime of the Tokamak*. Plasma Physics and Controlled Fusion, 29(3):351, 1987.

[45] R. Sweeney *et al. Statistical Analysis of Locked and Quasi-stationary Modes with Rotating Precursors at DIII-D*. Nuclear Fusion, 57(1):016019, 2017.

[46] R.J. Bickerton *et al. Diffusion Driven Plasma Currents and Bootstrap Tokamak*. Nature, 229:110, 1971.

[47] Z. Chang *et al. Observation of Nonlinear Neoclassical Pressure-Gradient–Driven Tearing Modes in TFTR*. Physical Review Letters, 74(23):4663, 1995.

[48] R.J. Buttery *et al. Neoclassical Tearing Modes*. Plasma Physics and Controlled Fusion, 42:B61, 2000.

[49] A. Pau *et al. A Tool to Support the Construction of Reliable Disruption Databases*. Fusion Engineering and Design, 125:139, 2017.

[50] E.A. Lazarus *et al. Control of the Vertical Stability in Tokamaks*. Nuclear Fusion, 30(1):111, 1990.

[51] S.J. Fielding *et al. High Density Discharges with Gettered Torus Walls in DITE*. Nuclear Fusion, 17(6):1382, 1977.

[52] M. Murakami *et al. Some Observations on Maximum Densities in Tokamak Experiments*. Nuclear Fusion, 16(2):347, 1976.

[53] M. Greenwald *et al. A New Look at Density Limits in Tokamaks*. Nuclear Fusion, 28(12):2199, 1988.

[54] M. Bernert *et al. The H-mode Density Limit in the full Tungsten ASDEX Upgrade Tokamak*. Plasma Physics and Controlled Fusion, 57(1):014038, 2014.

[55] S.S. Abdullaev *et al. Mappings of Stochastic Field Lines in Poloidal Divertor Tokamaks*. Nuclear Fusion, 46(4):S113, 2006.

[56] P.C. de Vries *et al. The Influence of an ITER-like Wall on Disruptions at JET*. Physics of Plasmas, 21(5):056101, 2014.

[57] V. Philipps *et al. Comparison of Tokamak Behaviour with Tungsten and Low-Z Plasma Facing Materials*. Plasma Physics and Controlled Fusion, 42(12B):293, 2000.

[58] H.R. Kozlowski. *Operational Limits in Tokamaks*. `http://www.iek-yig.de/531stWEH/talks/I5_2_Koslowski.pdf`, May 2013. [cit.November 2019].

[59] K.-D. Zastrow *et al. Transfer Rates of Toroidal Angular Momentum During Neutral Beam Injection.* Nuclear Fusion, 38(2):257, 1998.

[60] J.E. Rice. *Intrinsic and Driven Rotation in Tokamak Plasmas.* `http://library.psfc.mit.edu/catalog/reports/2010/16ja/16ja002/16ja002_full.pdf`, September 2016.

[61] R. McDermott *et al. Core Intrinsic Rotation Behaviour in ASDEX Upgrade Ohmic L-mode Plasmas.* Nuclear Fusion, 54(4):043009, 2014.

[62] T.H. Stix. *Decay of Poloidal Rotation in a Tokamak Plasma.* Physics of Fluids, 16(8):1260, 1973.

[63] Massachusetts Institute of Technology. *Fluid Description of Plasma.* `https://ocw.mit.edu/courses/nuclear-engineering/22-611j-introduction-to-plasma-physics-i-fall-2003/lecture-notes/chap4.pdf`, October 2003. [cit.November 2019].

[64] J.S. deGrassie *et al. Dimensionless Size Scaling of Intrinsic Rotation in DIII-D.* Physics of Plasmas, 23(8):082501, 2016.

[65] C. Sozzi *et al. Identifi*
cation of Disruption Paths for Prevention and Avoidance. `http://hdl.handle.net/21.11116/0000-0002-6F70-4`, October 2018. [cit.November 2019].

[66] M. Okabayashi *et al. Avoidance of Neoclassical Tearing Mode Locking and Disruption by Feedback-Induced Accelerating Electro-Magnetic Torque.* `http://ocs.ciemat.es/EPS2013PAP/pdf/P2.152.pdf`, July 2013. [cit.November 2019].

[67] J. Ham *et al. Resistive Wall Mode Stabilization by Differential Rotation in an Analytic Tokamak.* Plasma Physics and Controlled Fusion, 53(8):085003, 2011.

[68] A.W. Morris *et al. Feedback Stabilization of Disruption Precursors in a Tokamak.* Physical Review Letters, 64(11):1254, 1990.

[69] C. Chrystal *et al. Predicting Rotation for ITER via Studies of Intrinsic Torque and Momentum Transport in DIII-D.* Physics of Plasmas, 24(5):085003, 2017.

[70] M.J. Singh *et al. Heating Neutral Beams for ITER: Negative Ion Sources to Tune Fusion Plasmas.* New Journal of Physics, 19:055004, 2017.

[71] Z. Chang and J.D. Callen. *Global Energy Confinement Degradation due to Macroscopic Phenomena in Tokamaks.* Nuclear Fusion, 30(2):219, 1990.

[72] A. Kallenbach *et al. Characterization of the Angular Momentum Transport in ASDEX.* Plasma Physics and Controlled Fusion, 33(6):595, 1991.

[73] J. Snipes *et al. Large Amplitude Quasi-stationary MHD Modes in JET.* Nuclear Fusion, 28(6):1085, 1988.

[74] V. Igochine *et al. MHD Limits and Plasma Response in High-beta Hybrid Operations in ASDEX Upgrade.* Nuclear Fusion, 57(11):116027, 2017.

[75] R.H. La Haye *et al. Critical Error Fields for Locked Mode Instability in Tokamaks.* Physics of Fluids B: Plasma Physics, 4(7):2098, 1992.

[76] J.T. Scoville *et al. Multi-mode Error Field Correction on the DIII-D Tokamak.* Physics of Fluids B: Plasma Physics, 43(4):250, 2003.

[77] J.T. Scoville *et al. The Error Field Correction Coils on the JET Machine.* Fusion Engineering and Design, 58(11):250, 2001.

[78] D.A. Gates and T.C. Hender. *Resistive Wall Induced Forbidden Bands of Mode Rotation Frequency on the COMPASS-D Tokamak.* Nuclear Fusion, 36(6):273, 1996.

[79] P.C. de Vries *et al. MHD-mode Stabilization by Plasma Rotation in TEXTOR.* Plasma Physics and Controlled Fusion, 38(4):467, 1996.

[80] B.E. Chapman *et al. Observation of Tearing Mode Deceleration and Locking due to Eddy Currents Induced in a Conducting Shell.* Physics of Plasmas, 11(5):2156, 2004.

[81] R.J. Buttery *et al. Error Field Mode Studies on JET, COMPASS-D and DIII-D, and Implications for ITER.* Nuclear Fusion, 39(11Y):1827, 1999.

[82] I.H. Hutchinson. *Principles of Plasma Diagnostics.* Cambridge University Press, 2009, ISBN: 978-0511613630.

[83] S. Zurek. *Encyclopedia Magnetica, Mirnov Coils.* `http://www.encyclopedia-magnetica.com/doku.php/file/mirnov_coils_magnetica.png`, July 2013. [cit.December 2019].

[84] C.A.J. Hugenholtz. *Microwave Interferometer and Reflectometer Techniques for Thermonuclear Plasmas.* `https://pure.tue.nl/ws/files/3681746/328524.pdf`, January 1990. [cit.December 2019].

[85] D. Veron *et al. Multichannel HCN Interferometer for Electron Density Profile Measurements of Tokamak Plasmas.* Journal of the Optical Society of America, 67(7):964, 1977.

[86] Li-Wen-Lai and X. You-Gang. *A DCN Laser Interferometer for Electron Density Measurements of Plasmas.* International Journal of Infrared and Millimeter Waves, 5(6):767, 1984.

[87] C.E. Gil *et al. Analysis and Improvements of Fringe Jump Corrections by Electronics on the JET Tokamak Far Infrared Interferometer.* The Review of Scientific Instruments, 81(10):10D536, 2010.

[88] J-W. Juhn *et al. Fringe-jump Corrected Far Infrared Tangential Interferometer/Polarimeter for a Real-time Density Feedback Control System of NSTX Plasmas.* The Review of Scientific Instruments, 81(10):10D540, 2010.

[89] D.E. Billings. *A Guide to the Solar Corona.* Academic Press, 1966, ISBN: 978-1483274188.

[90] N.J. Peacock *et al. Measurement of the Electron Temperature by Thomson Scattering in Tokamak T3.* Nature, 224:488, 1969.

[91] N.J. Peacock *et al. A Pulse-burst Laser System for Thomson Scattering on NSTX-U.* Journal of Instrumentation, 12:C10002, 2017.

[92] W. Moller. *Fundamentals of Plasma Physics.* `https://www.hzdr.de/db/Cms?pOid=23689`, June 2006. [cit.December 2019].

[93] A.E. Costley *et al. Electron Cyclotron Emission from a Tokamak Plasma: Experiment and Theory.* Physical Review Letters, 33(13):758, 1974.

[94] M. Bornatici *et al. Electron Cyclotron Emission and Absorption in Fusion Plasmas.* Nuclear Fusion, 23(9):1153, 1983.

[95] R.J. Fonck *et al.* *Determination of Plasma-ion Velocity Distribution via Charge-exchange Recombination Spectroscopy.* Physical Review A, 29(6):3288, 1983.

[96] P.J. McCarthy *et al.* *The CLISTE interpretive equilibrium code.* `https://pure.mpg.de/pubman/faces/ViewItemFullPage.jsp?itemId=item_2130737_1&view=EXPORT`, June 1999. [cit. December 2019].

[97] L.L. Lao *et al.* *Reconstruction of Current Profile Parameters and Plasma Shapes in Tokamaks.* Nuclear Fusion, 25(11):1611, 1985.

[98] F.M. Levinton *et al.* *Magnetic Field Pitch-angle Measurements in the PBX-M Tokamak Using the Motional Stark Effect.* Physical Review Letters, 63(19):2060, 1989.

[99] K. Tahiliani and R. Jha. *Bolometers for Fusion Plasma Diagnostics.* 2012, ISBN: 978-9535102359.

[100] IPP Prague. *COMPASS tokamak.* `http://www.ipp.cas.cz/vedecka_struktura_ufp/tokamak/tokamak_compass/`, June 2018. [cit. January 2019].

[101] R. Pánek *et al.* *Reinstallation of the COMPASS-D Tokamak in IPP ASCR.* Czechoslovak Journal of Physics, 56(2):125, 2006.

[102] R. Pánek *et al.* *Status of the COMPASS Tokamak and Characterization of the First H-mode.* Plasma Physics and Controlled Fusion, 58(1):014015, 2015.

[103] F. Wagner *et al.* *Development of an Edge Transport Barrier at the H-Mode Transition of ASDEX.* Physical Review Letters, 53(15):1453, 1984.

[104] R. Neu *et al.* *Development of an Edge Transport Barrier at the H-Mode Transition of ASDEX.* Journal of Nuclear Materials, 438(S):34, 2013.

[105] J.L. Luxon. *A Design Retrospective of the DIII-D Tokamak.* Nuclear Fusion, 42(5):614, 2002.

[106] M.L. Walker *et al.* *Next-generation Plasma Control in the DIII-D Tokamak.* Fusion Engineering and Design, 66:749, 2003.

[107] M. Keilhacker *et al.* *High Fusion Performance from Deuterium-tritium Plasmas in JET.* Fusion Engineering and Design, 39(2):209, 1999.

[108] A.C. Rolfe. *Operational Aspects of the JET Remote Handling System.* Fusion Engineering and Design, 10:501, 1989.

[109] V. Philipps *et al.* *Overview of the JET ITER-like Wall Project.* Fusion Engineering and Design, 85(7-9):1581, 2010.

[110] E. Joffrin *et al.* *Overview of the JET Preparation for Deuterium–tritium Operation with the ITER Like-wall.* Nuclear Fusion, 59(11):112021, 2019.

[111] V. Riccardo *et al.* *Analysis of JET Halo Currents.* Plasma Physics and Controlled Fusion, 46(6):925, 2004.

[112] P.C. de Vries *et al.* *Survey of Disruption Causes at JET.* Nuclear Fusion, 51(5):053018, 2011.

[113] G. Pautasso *et al.* *Proceedings of the 40th EPS Conference on Plasma Physics, Berlin, Germany, Disruption Causes in ASDEX Upgrade.* `http://ocs.ciemat.es/EPS2014PAP/pdf/P2.015.pdf`, July 2014. [cit.December 2019].

[114] J.T. Scoville *et al. Locked Modes in DIII-D and a Method for Prevention of the Low Density Mode.* Nuclear Fusion, 31(5):875, 1991.

[115] M. Komm *et al. Divertor Impurity Seeding Experiments at the COMPASS Tokamak.* Nuclear Fusion, 59(10):106035, 2019.

[116] J.A. Holmes *et al. Stabilization of Tearing Modes to Suppress Major Disruptions in Tokamaks.* Nuclear Fusion, 19(10):1333, 1979.

[117] B. Esposito *et al. Disruption Avoidance by Means of Electron Cyclotron Waves.* Nuclear Fusion, 53(12):124035, 2011.

[118] G. Granucci *et al. Proceedings of the 40th EPS Conference on Plasma Physics, Berlin, Germany, Stable Operation at Disruptive Limits by Means of EC at ASDEX Upgrade.* `https://pdfs.semanticscholar.org/b5b5/23e9a22766596340360446196O6bd42302a5.pdf`, July 2015. [cit.December 2019].

[119] O. Klüber *et al. MHD Mode Structure and Propagation in the ASDEX Tokamak.* Nuclear Fusion, 31(5):907, 1991.

[120] Princeton Plasma Physics Laboratory. *TRANSP references.* `https://omfit.io/modules/mod_TRANSP.html`, November 2019. [cit.December 2019].

[121] L. Laurent *et al. Improvement of the Tokamak Concept.* INIS Volume, 28:28016718, 1994.

[122] N.C. Logan *et al. Measurement of the Electromagnetic Torque in Rotating DIII-D Plasmas.* Plasma Physics and Controlled Fusion, 52(4):045013, 2010.

[123] M. Bernert *et al. The H-mode Density Limit in the Full Tungsten ASDEX Upgrade Tokamak.* Plasma Physics and Controlled Fusion, 57(1):014038, 2014.

[124] J. Snipes *et al. Plasma Stored Energy and Momentum Losses During Large MHD Activity in JET.* Nuclear Fusion, 30(2):205, 1990.

[125] H. Zohm *et al. Plasma Angular Momentum Loss by MHD Mode Locking.* Europhysics Letters, 11(8):745, 1990.

[126] M. Maraschek *et al. Proceedings of the 40th EPS Conference on Plasma Physics, Berlin, Germany, Measurement and Impact of the n=1 Intrinsic Error Field at ASDEX Upgrade.* `http://ocs.ciemat.es/EPS2013PAP/pdf/P4.127.pdf`, July 2014. [cit.December 2019].

[127] N.W. Eidietis *et al. Implementing a Finite-state Off-normal and Fault Response System for Disruption Avoidance in Tokamaks.* Nuclear Fusion, 58(5):056023, 2018.

[128] C. Reux *et al. Use of the Disruption Mitigation Valve in Closed Loop for Routine Protection at JET.* Fusion Engineering and Design, 88(6):1101, 2013.

[129] H. van den Brand *et al. Integrated Modelling of Island Growth, Stabilization and Mode Locking: Consequences for NTM Control on ITER.* Plasma Physics and Controlled Fusion, 54(9):094003, 2012.

[130] J.L. Barr *et al. Proceedings of the 27th IAEA Fusion Energy Conference, Ahmedabad, India, Fast ITER-relevant Low-disruptivity Rampdowns*

in DIII-D and EAST. `https://conferences.iaea.org/indico/event/151/papers/6280/files/4298-IAEA_FEC_2018_BARR_vSubmit.pdf`, October 2018. [cit.December 2019].

[131] J.A. Wesson *et al. Disruptions in JET*. Nuclear Fusion, 29(4):641, 1989.

[132] K. Kurihara *et al. Plasma Control Systems Relevant to ITER and Fusion Power Plants*. Fusion Engineering and Design, 83(7):959, 2008.

[133] G. Pautasso *et al. The ITER Disruption Mitigation Trigger: Developing its Preliminary Design*. Nuclear Fusion, 58(3):036011, 2018.

[134] Private communication with G. Verdoolaege.

[135] O.J.W.F. Kardaun. *Interval estimate of the global energy confinement time during ELMy H-mode in ITER-FEAT, based on the international multi-tokamak ITERH.DB3 dataset*. IPP-IR-2002/5 1.1, Max Planck Institute for Plasma Physics, Garching, Germany, 2002.

[136] A. Murari, E. Peluso, P. Gaudio, and M. Gelfusa. *Robust scaling laws for energy confinement time, including radiated fraction, in Tokamaks*. Nuclear Fusion, 57(12):26017, 2017.

[137] R. Sweeney and E.J. Strait. *Decomposing Magnetic Field Measurements into Internally and Externally Sourced Components in Toroidal Plasma Devices*. Physics of Plasmas, 26(1):012509, 2019.

[138] S. Dormido-Canto *et al. Development of an Efficient Real-time Disruption Predictor from Scratch on JET and Implications for ITER*. Nuclear Fusion, 53(11):113001, 2013.

[139] S.A. Sabbagh *et al. Proceedings of the 27th IAEA Fusion Energy Conference, Ahmedabad, India, Disruption Event Characterization and Forecasting in Tokamaks*, October 2018. [cit.August 2020].

Acknowledgements

Without a second of doubts I can state that I received a great supervision of my work during my doctoral studies. I would like to express a sincere gratitude to all my supervisors and advisors.

Dr. Gabriella Pautasso and Prof. Hartmut Zohm dedicated a substantial amount of time to discussions about the progress of my work. They offered help, when needed, shared ideas and improved my manuscripts and presentations with patience and a kind attitude. Their support has led to the completion of this dissertation.

Prof. Geert Verdoolaege always provided a constructive input to my work and an important feedback and input to the manuscripts. All this, together with the practical support from the university side arranged by him, significantly contributed to the dissertation finalization.

Drs. Peter de Vries, Joseph Snipes and Michael Lehnen led my work during my internship at ITER. Our discussion sessions, combined with the exciting working environment, turned my internship into a pleasant experience with highly added value in terms of the gathered knowledge. I am thankful for that.

Data presented in this thesis were acquired in multiple institutes. The data gathering and processing would not be possible without a help from the side of the tokamak team members. I would like to express gratitude to all colleagues who contributed to this task. In particular, I would like to acknowledge helpful input from Drs. Marc Maraschek, Anja Gude, Giovanni Tardini, Rachael McDermott, Ondřej Kudláček, Filip Janky, Valentin Igochine, Hendrik Meyer and other ASDEX Upgrade and MST1 team members. Drs. Michael Komm, Josef Havlíček and fellow students Tomáš Markovič, Ondřej Kovanda, Martin Imríšek and other colleagues from the COMPASS team at IPP Prague, Drs. Ryan Sweeney, Edward Strait and others from the DIII-D working group, as well as Matteo Baruzzo from the JET team contributed to the work presented here.

I would like to thank Profs. Jean-Marie Noterdaeme and Kristel Crombé for organizing the FUSION-DC program, my thanks extends to all the other people involved in the program realization.

The fellow students, post-doc researches, simply all colleagues that I met during my doctoral studies created an ambient and productive working environment. I appreciate that.

Lastly, I would like to address one big thanks to my family. Support of all kinds from the side of my family was essential to the completion of this document. A special note applies to my parents and my sisters: you have always showed interest in my work and shared both good and challenging times with me. Thank you for that.